

Artificial Intelligence in *Medical Imaging*

Artif Intell Med Imaging 2020 June 28; 1(1): 1-69



A**|****M****|**

Artificial Intelligence in Medical Imaging

Contents

Bimonthly Volume 1 Number 1 June 28, 2020

EDITORIAL

- 1 Rising role of artificial intelligence in image reconstruction for biomedical imaging
Chen XL, Yan TY, Wang N, von Deneen KM

REVIEW

- 6 Breast dynamic contrast-enhanced-magnetic resonance imaging and radiomics: State of art
Orlando A, Dimarco M, Cannella R, Bartolotta TV

MINIREVIEWS

- 19 Artificial intelligence in pancreatic disease
Chen BB
- 31 Machine learning for diagnosis of coronary artery disease in computed tomography angiography: A survey
Zhao FJ, Fan SQ, Ren JF, von Deneen KM, He XW, Chen XL
- 40 Acute pancreatitis: A pictorial review of early pancreatic fluid collections
Xiao B

ORIGINAL ARTICLE

Basic Study

- 50 Acoustic concept based on an autonomous capsule and a wideband concentric ring resonator for pathophysiological prevention
Medjdoub A, Lefebvre F, Saad N, Soudani S, Nassar G

CASE REPORT

- 65 Cerebral amyloid angiopathy vs Alzheimer's dementia: Diagnostic conundrum
Arberry J, Singh S, Mizoguchi RA

ABOUT COVER

Editor-in-Chief of *Artificial Intelligence in Medical Imaging*, Professor Xue-Li Chen is an expert in the field of biomedical photonics imaging as well as its application in early detection and accurate diagnosis of gastric cancer. Professor Chen has co-lead the development of Cerenkov luminescence endoscope and further explored the application in early detection of clinical gastrointestinal tumors. Professor Chen has also developed the stimulated Raman projection tomography technology which can perform the volumetric imaging of single cells in a label-free manner. Professor Chen has served as the member of SPIE, OSA, IEEE, and as a committee member of the Branch of Contrast Technology in China Medicinal Biotech Association, the Nuclear Medicine Committee of Shaanxi Cancer Association, and the Shaanxi Society of Biomedical Engineering.

AIMS AND SCOPE

The primary aim of *Artificial Intelligence in Medical Imaging (AIMI, Artif Intell Med Imaging)* is to provide scholars and readers from various fields of artificial intelligence in medical imaging with a platform to publish high-quality basic and clinical research articles and communicate their research findings online.

AIMI mainly publishes articles reporting research results obtained in the field of artificial intelligence in medical imaging and covering a wide range of topics, including artificial intelligence in radiology, pathology image analysis, endoscopy, molecular imaging, and ultrasonography.

INDEXING/ABSTRACTING

There is currently no indexing.

RESPONSIBLE EDITORS FOR THIS ISSUE

Electronic Editor: *Yan-Xia Xing*, Production Department Director: *Yun-Xiaojuan Wu*, Editorial Office Director: *Jin-Lei Wang*.

NAME OF JOURNAL

Artificial Intelligence in Medical Imaging

ISSN

ISSN 2644-3260 (online)

LAUNCH DATE

June 28, 2020

FREQUENCY

Bimonthly

EDITORS-IN-CHIEF

Xue-Li Chen, Ahmed Abd El-Razek, Jun Shen

EDITORIAL BOARD MEMBERS

<https://www.wjgnet.com/2644-3260/editorialboard.htm>

PUBLICATION DATE

June 28, 2020

COPYRIGHT

© 2020 Baishideng Publishing Group Inc

INSTRUCTIONS TO AUTHORS

<https://www.wjgnet.com/bpg/gerinfo/204>

GUIDELINES FOR ETHICS DOCUMENTS

<https://www.wjgnet.com/bpg/GerInfo/287>

GUIDELINES FOR NON-NATIVE SPEAKERS OF ENGLISH

<https://www.wjgnet.com/bpg/gerinfo/240>

PUBLICATION ETHICS

<https://www.wjgnet.com/bpg/GerInfo/288>

PUBLICATION MISCONDUCT

<https://www.wjgnet.com/bpg/gerinfo/208>

ARTICLE PROCESSING CHARGE

<https://www.wjgnet.com/bpg/gerinfo/242>

STEPS FOR SUBMITTING MANUSCRIPTS

<https://www.wjgnet.com/bpg/GerInfo/239>

ONLINE SUBMISSION

<https://www.f6publishing.com>



Rising role of artificial intelligence in image reconstruction for biomedical imaging

Xue-Li Chen, Tian-Yu Yan, Nan Wang, Karen M von Deneen

ORCID number: Xue-Li Chen [0000-0002-3898-9892](https://orcid.org/0000-0002-3898-9892); Tian-Yu Yan [0000-0002-2245-1537](https://orcid.org/0000-0002-2245-1537); Nan Wang [0000-0002-6780-3401](https://orcid.org/0000-0002-6780-3401); Karen M von Deneen [0000-0002-5310-1003](https://orcid.org/0000-0002-5310-1003).

Author contributions: Chen XL designed the overall outline of the manuscript; Yan TY and Wang N performed the literature review and summary; Chen XL contributed to the writing and editing of the manuscript; von Deneen KM polished the language of the paper.

Supported by The National Key R&D Program of China, No. 2018YFC0910600; the National Natural Science Foundation of China No. 81627807 and 11727813; Shaanxi Science Funds for Distinguished Young Scholars, No. 2020JC-27; the Fok Ying Tung Education Foundation, No. 161104; and Program for the Young Top-notch Talent of Shaanxi Province.

Conflict-of-interest statement: The authors declare that they have no conflicts of interest.

Open-Access: This article is an open-access article that was selected by an in-house editor and fully peer-reviewed by external reviewers. It is distributed in accordance with the Creative Commons Attribution NonCommercial (CC BY-NC 4.0)

Xue-Li Chen, Tian-Yu Yan, Nan Wang, Karen M von Deneen, Engineering Research Center of Molecular and Neuro Imaging of Ministry of Education, School of Life Science and Technology, Xidian University, Xi'an 710126, Shaanxi Province, China

Corresponding author: Xue-Li Chen, PhD, Professor, Engineering Research Center of Molecular and Neuro Imaging of Ministry of Education, School of Life Science and Technology, Xidian University, No. 266, Xinglong Section of Xifeng Road, Xi'an 710126, Shaanxi Province, China. xlchen@xidian.edu.cn

Abstract

In this editorial, we review recent progress on the applications of artificial intelligence (AI) in image reconstruction for biomedical imaging. Because it abandons prior information of traditional artificial design and adopts a completely data-driven mode to obtain deeper prior information *via* learning, AI technology plays an increasingly important role in biomedical image reconstruction. The combination of AI technology and the biomedical image reconstruction method has become a hotspot in the field. Favoring AI, the performance of biomedical image reconstruction has been improved in terms of accuracy, resolution, imaging speed, *etc.* We specifically focus on how to use AI technology to improve the performance of biomedical image reconstruction, and propose possible future directions in this field.

Key words: Biomedical imaging; Image reconstruction; Artificial intelligence; Machine learning; Deep learning; Tomography

©The Author(s) 2020. Published by Baishideng Publishing Group Inc. All rights reserved.

Core tip: Three-dimensional biomedical imaging plays an important role in biology and medicine. We review recent progress on the applications of artificial intelligence (AI) in image reconstruction for biomedical imaging. We specifically focus on how to use AI technology to improve the performance of biomedical image reconstruction and propose possible future directions in this field. We believe that, with further development, AI technology will play an increasingly important role in biomedical image reconstruction.

Citation: Chen XL, Yan TY, Wang N, von Deneen KM. Rising role of artificial intelligence in

license, which permits others to distribute, remix, adapt, build upon this work non-commercially, and license their derivative works on different terms, provided the original work is properly cited and the use is non-commercial. See: <http://creativecommons.org/licenses/by-nc/4.0/>

Manuscript source: Invited manuscript

Received: May 7, 2020

Peer-review started: May 7, 2020

First decision: May 15, 2020

Revised: June 9, 2020

Accepted: June 17, 2020

Article in press: June 17, 2020

Published online: June 28, 2020

P-Reviewer: Tomizawa N

S-Editor: Wang JL

L-Editor: Filipodia

E-Editor: Ma YJ



image reconstruction for biomedical imaging. *Artif Intell Med Imaging* 2020; 1(1): 1-5

URL: <https://www.wjgnet.com/2644-3260/full/v1/i1/1.htm>

DOI: <https://dx.doi.org/10.35711/aimi.v1.i1.1>

BACKGROUND

Biomedical imaging plays an important role in biology and medicine. In particular, three-dimensional (3D) imaging mode based on an image reconstruction technique, such as computed tomography (CT), magnetic resonance imaging (MRI), positron emission tomography (PET), photoacoustic tomography (PAT), and 3D optical imaging, allow biologists and physicians to visualize the structural, cellular, and functional information stereoscopically. Image reconstruction in 3D biomedical imaging is a type of inverse problem, which is used to reconstruct the distribution of this information in the living body by using the physical signals acquired from outside of the body. Research on the image reconstruction algorithm has always been an important issue to promote the development and innovation of biomedical imaging equipment. However, due to several reasons, such as the limitation of imaging time and dose (contrast medium or radiation dose), insufficiency of the measurements, inherent noise and other interference doping in the original signals, the traditional image reconstruction techniques cannot achieve good performance. For example, there are trade-offs in optimal imaging accuracy, spatial resolution and imaging speed, which have been challenges in the field of biomedical image reconstruction. The rapid development of artificial intelligence (AI) technology brings new opportunities for biomedical image reconstruction. AI abandons prior information of traditional artificial design, and adopts a completely data-driven mode to obtain deeper prior information *via* learning. Currently, the combination of AI and the biomedical image reconstruction method has become a hotspot in the field.

ADVANCES

Recently, AI plays an increasingly important role in image reconstruction of 3D biomedical imaging, including both clinical and preclinical biomedical imaging technologies such as CT, MRI, PET, PAT, and 3D optical imaging. In CT reconstruction, AI technology mainly focuses on solving two problems: CT reconstruction with low radiation dose and CT reconstruction with a small amount of view measurements^[1-6]. For example, Chen *et al*^[1] integrated the autoencoder, deconvolution network, and shortcut connections into the residual encoder-decoder convolutional natural network for low-dose CT imaging, which demonstrated great potential for high-speed imaging with good noise reduction, structural preservation, and lesion detection. For CT reconstruction with a small amount of view measurements, it mainly involves a small amount of view reconstruction based on limited angles^[2-4] and sparse view reconstruction based on full angles^[5-7]. With the help of the deep learning framework, researchers can obtain a much clearer edge and fine structural information through a small amount of measured data, to achieve the best imaging quality with faster imaging speed^[5-7]. The use of AI technology in MRI image reconstruction has attracted an increasing amount of attention, and much progress has been made in recent years. In these works, by means of machine learning or deep learning framework, MRI image reconstruction can be much improved by reducing noise or artifacts^[8], enhancing spatial resolution or details^[9-12], accelerating imaging speed^[13-16], and improving image accuracy and quality^[17-21]. AI-based image reconstruction techniques have also been applied to clinical studies, for example the TrueFidelity^[22], a deep learning-based image processing platform developed by General Electric Healthcare and the Advanced intelligent clear-IQ Engine^[23], developed by Canon Medical Systems Corporation.

In functional or molecular imaging, AI technology is mainly used to improve the quality of reconstructed images^[24-38]. For example, by using AI technology, high-quality PET images can be reconstructed from low-dose and ultra-low-dose radionuclides^[24,25]. The whole neural network can solve the storage space challenge in PET and realize the direct reconstruction of large-scale data^[26]. With the help of machine learning and deep learning frameworks, the problems existing in PAT image reconstruction caused by limited views or sparse view measurements, including resolution and image quality

degradation, can be solved^[29-33]. In diffuse light-based 3D optical imaging, it is necessary to establish a mathematical model to describe diffused light propagation in the living body, and then to calculate the target distribution by solving the model in reverse^[39,40]. However, this mathematical model is usually a simplified linear model that has serious ill-posedness, which results in poor quality of reconstructed images. With the help of the deep learning framework by directly learning the complicated relationship between surface measurements and target distribution inside the body, the quality of the reconstructed image can be greatly improved and the reconstruction time can be reduced^[34-38].

OUTLOOK

We present recent progresses on AI-based image reconstruction for 3D biomedical imaging. The rising role of AI in image reconstruction includes improving the quality, accuracy, and resolution of the reconstructed image as well as the imaging speed. Furthermore, with the rapid development of AI technology, such a rising role will become increasingly significant. However, there remain several central challenges facing the field. The first one is the generality of machine learning or the deep learning framework. In existing studies, the frameworks are all aimed at specific problems, such as image objects with specific features. Thus, generalization performance and the migration ability of the framework are poor. If a network framework can be developed, which can provide good image reconstruction performance for the imaging objects with various structures and properties, even for all of the biomedical imaging technologies, it will be great progress on AI-based image reconstruction for biomedical imaging. Second, current research needs to use AI technology to reconstruct the measured data into images, and then analyze these images to obtain relevant physiological or pathological information. With the help of AI, it will be significant to obtain physiological and pathological information directly from the measured data, which is also the future direction of the application of AI technology in the field of biomedical imaging. Lastly, the development of machine learning or the deep learning algorithm itself is also an important direction in the field. These efforts are expected to promote the wide applications of AI-based biomedical imaging in biology and medicine.

REFERENCES

- 1 **Chen H**, Zhang Y, Kalra MK, Lin F, Chen Y, Liao P, Zhou J, Wang G. Low-Dose CT With a Residual Encoder-Decoder Convolutional Neural Network. *IEEE Trans Med Imaging* 2017; **36**: 2524-2535 [PMID: 28622671 DOI: 10.1109/TMI.2017.2715284]
- 2 **Jiang Z**, Chen Y, Zhang Y, Ge Y, Yin FF, Ren L. Augmentation of CBCT Reconstructed From Under-Sampled Projections Using Deep Learning. *IEEE Trans Med Imaging* 2019; **38**: 2705-2715 [PMID: 31021791 DOI: 10.1109/TMI.2019.2912791]
- 3 **Bubba TA**, Kutyniok G, Lasses M, Marz M, Samek W, Siltanen S, Srinivasan V. Learning the invisible: a hybrid deep learning-shearlet framework for limited angle computed tomography. *Inverse Probl* 2019; **35**: 064002 [DOI: 10.1088/1361-6420/ab10ca]
- 4 **Fu J**, Dong J, Zhao F. A Deep Learning Reconstruction Framework for Differential Phase-Contrast Computed Tomography With Incomplete Data. *IEEE Trans Image Process* 2020; **29**: 2190-2202 [PMID: 31647435 DOI: 10.1109/TIP.2019.2947790]
- 5 **Kyong Hwan Jin**, McCann MT, Froustey E, Unser M. Deep Convolutional Neural Network for Inverse Problems in Imaging. *IEEE Trans Image Process* 2017; **26**: 4509-4522 [PMID: 28641250 DOI: 10.1109/TIP.2017.2713099]
- 6 **Han Y**, Ye JC. Framing U-Net via Deep Convolutional Framelets: Application to Sparse-View CT. *IEEE Trans Med Imaging* 2018; **37**: 1418-1429 [PMID: 29870370 DOI: 10.1109/TMI.2018.2823768]
- 7 **Nakai H**, Nishio M, Yamashita R, Ono A, Nakao KK, Fujimoto K, Togashi K. Quantitative and Qualitative Evaluation of Convolutional Neural Networks with a Deeper U-Net for Sparse-View Computed Tomography Reconstruction. *Acad Radiol* 2020; **27**: 563-574 [PMID: 31281082 DOI: 10.1016/j.acra.2019.05.016]
- 8 **Zhu B**, Liu JZ, Cauley SF, Rosen BR, Rosen MS. Image reconstruction by domain-transform manifold learning. *Nature* 2018; **555**: 487-492 [PMID: 29565357 DOI: 10.1038/nature25988]
- 9 **Chaudhari AS**, Fang Z, Kogan F, Wood J, Stevens KJ, Gibbons EK, Lee JH, Gold GE, Hargreaves BA. Super-resolution musculoskeletal MRI using deep learning. *Magn Reson Med* 2018; **80**: 2139-2154 [PMID: 29582464 DOI: 10.1002/mrm.27178]
- 10 **Sun L**, Fan Z, Fu X, Huang Y, Ding X, Paisley J. A Deep Information Sharing Network for Multi-Contrast Compressed Sensing MRI Reconstruction. *IEEE Trans Image Process* 2019; **28**: 6141-6153 [PMID: 31295112 DOI: 10.1109/TIP.2019.2925288]
- 11 **Shi J**, Li Z, Ying S, Wang C, Liu Q, Zhang Q, Yan P. MR Image Super-Resolution via Wide Residual

- Networks With Fixed Skip Connection. *IEEE J Biomed Health Inform* 2019; **23**: 1129-1140 [PMID: 29993565 DOI: [10.1109/JBHI.2018.2843819](https://doi.org/10.1109/JBHI.2018.2843819)]
- 12 **Zhang J**, Gu Y, Tang H, Wang X, Kong Y, Chen Y, Shu H, Coatrieux J. Compressed sensing MR image reconstruction via a deep frequency-division network. *Neurocomputing* 2020; **384**: 346-355 [DOI: [10.1016/j.neucom.2019.12.011](https://doi.org/10.1016/j.neucom.2019.12.011)]
 - 13 **Yang G**, Yu S, Dong H, Slabaugh G, Dragotti PL, Ye X, Liu F, Arridge S, Keegan J, Guo Y, Firmin D, Keegan J, Slabaugh G, Arridge S, Ye X, Guo Y, Yu S, Liu F, Firmin D, Dragotti PL, Yang G, Dong H. DAGAN: Deep De-Aliasing Generative Adversarial Networks for Fast Compressed Sensing MRI Reconstruction. *IEEE Trans Med Imaging* 2018; **37**: 1310-1321 [PMID: 29870361 DOI: [10.1109/TMI.2017.2785879](https://doi.org/10.1109/TMI.2017.2785879)]
 - 14 **Lee D**, Yoo J, Tak S, Ye JC. Deep Residual Learning for Accelerated MRI Using Magnitude and Phase Networks. *IEEE Trans Biomed Eng* 2018; **65**: 1985-1995 [PMID: 29993390 DOI: [10.1109/TBME.2018.2821699](https://doi.org/10.1109/TBME.2018.2821699)]
 - 15 **Xiang L**, Chen Y, Chang W, Zhan Y, Lin W, Wang Q, Shen D. Deep Learning Based Multi-Modal Fusion for Fast MR Reconstruction. *IEEE Trans Biomed Eng* 2019; **66**: 2105-2114 [PMID: 30507491 DOI: [10.1109/TBME.2018.2883958](https://doi.org/10.1109/TBME.2018.2883958)]
 - 16 **Zhang J**, Wu J, Chen S, Zhang Z, Cai S, Cai C, Chen Z. Robust Single-Shot T₂ Mapping via Multiple Overlapping-Echo Acquisition and Deep Neural Network. *IEEE Trans Med Imaging* 2019; **38**: 1801-1811 [PMID: 30714913 DOI: [10.1109/TMI.2019.2896085](https://doi.org/10.1109/TMI.2019.2896085)]
 - 17 **Schlemper J**, Caballero J, Hajnal JV, Price AN, Rueckert D. A Deep Cascade of Convolutional Neural Networks for Dynamic MR Image Reconstruction. *IEEE Trans Med Imaging* 2018; **37**: 491-503 [PMID: 29035212 DOI: [10.1109/TMI.2017.2760978](https://doi.org/10.1109/TMI.2017.2760978)]
 - 18 **Quan TM**, Nguyen-Duc T, Jeong WK. Compressed Sensing MRI Reconstruction Using a Generative Adversarial Network With a Cyclic Loss. *IEEE Trans Med Imaging* 2018; **37**: 1488-1497 [PMID: 29870376 DOI: [10.1109/TMI.2018.2820120](https://doi.org/10.1109/TMI.2018.2820120)]
 - 19 **Mardani M**, Gong E, Cheng JY, Vasanawala SS, Zaharchuk G, Xing L, Pauly JM. Deep Generative Adversarial Neural Networks for Compressive Sensing MRI. *IEEE Trans Med Imaging* 2019; **38**: 167-179 [PMID: 30040634 DOI: [10.1109/TMI.2018.2858752](https://doi.org/10.1109/TMI.2018.2858752)]
 - 20 **Qin C**, Schlemper J, Caballero J, Price AN, Hajnal JV, Rueckert D. Convolutional Recurrent Neural Networks for Dynamic MR Image Reconstruction. *IEEE Trans Med Imaging* 2019; **38**: 280-290 [PMID: 30080145 DOI: [10.1109/TMI.2018.2863670](https://doi.org/10.1109/TMI.2018.2863670)]
 - 21 **Kofler A**, Dewey M, Schaeffter T, Wald C, Kolbitsch C. Spatio-Temporal Deep Learning-Based Undersampling Artefact Reduction for 2D Radial Cine MRI With Limited Training Data. *IEEE Trans Med Imaging* 2020; **39**: 703-717 [PMID: 31403407 DOI: [10.1109/TMI.2019.2930318](https://doi.org/10.1109/TMI.2019.2930318)]
 - 22 **Hsieh J**, Liu E, Nett B, Tang J, Thibault JB, Sahney S. A new era of image reconstruction: TrueFidelityTM - Technical white paper on deep learning imaging reconstruction. New York: General Electric Company, 2019: 1-14
 - 23 **Boedeker K**. AiCE deep learning reconstruction: bringing the power of ultra-high resolution CT to routine imaging. Tochigi: Canon Medical Systems Corporation, 2019
 - 24 **Kim K**, Wu D, Gong K, Dutta J, Kim JH, Son YD, Kim HK, El Fakhri G, Li Q. Penalized PET Reconstruction Using Deep Learning Prior and Local Linear Fitting. *IEEE Trans Med Imaging* 2018; **37**: 1478-1487 [PMID: 29870375 DOI: [10.1109/TMI.2018.2832613](https://doi.org/10.1109/TMI.2018.2832613)]
 - 25 **Ouyang J**, Chen KT, Gong E, Pauly J, Zaharchuk G. Ultra-low-dose PET reconstruction using generative adversarial network with feature matching and task-specific perceptual loss. *Med Phys* 2019; **46**: 3555-3564 [PMID: 31131901 DOI: [10.1002/mp.13626](https://doi.org/10.1002/mp.13626)]
 - 26 **Xu J**, Liu H. Three-dimensional convolutional neural networks for simultaneous dual-tracer PET imaging. *Phys Med Biol* 2019; **64**: 185016 [PMID: 31292287 DOI: [10.1088/1361-6560/ab3103](https://doi.org/10.1088/1361-6560/ab3103)]
 - 27 **Gong K**, Catana C, Qi J, Li Q. PET Image Reconstruction Using Deep Image Prior. *IEEE Trans Med Imaging* 2019; **38**: 1655-1665 [PMID: 30575530 DOI: [10.1109/TMI.2018.2888491](https://doi.org/10.1109/TMI.2018.2888491)]
 - 28 **Whiteley W**, Luk WK, Gregor J. DirectPET: full-size neural network PET reconstruction from sinogram data. *J Med Imaging (Bellingham)* 2020; **7**: 032503 [PMID: 32206686 DOI: [10.1117/1.JMI.7.3.032503](https://doi.org/10.1117/1.JMI.7.3.032503)]
 - 29 **Antholzer S**, Haltmeier M, Schwab J. Deep learning for photoacoustic tomography from sparse data. *Inverse Probl Sci Eng* 2019; **27**: 987-1005 [PMID: 31057659 DOI: [10.1080/17415977.2018.1518444](https://doi.org/10.1080/17415977.2018.1518444)]
 - 30 **Waibel D**, Grohl J, Isensee F, Kirchner T, Maier-Hein K, Maier-Hein L. Reconstruction of initial pressure from limited view photoacoustic images using deep learning. *Oraevsky A, Wang L, editors. Photons Plus Ultrasound: Imaging and Sensing. SPIE* 2018; 104942S [DOI: [10.1117/12.2288353](https://doi.org/10.1117/12.2288353)]
 - 31 **Hauptmann A**, Lucka F, Betcke M, Huynh N, Adler J, Cox B, Beard P, Ourselin S, Arridge S. Model-Based Learning for Accelerated, Limited-View 3-D Photoacoustic Tomography. *IEEE Trans Med Imaging* 2018; **37**: 1382-1393 [PMID: 29870367 DOI: [10.1109/TMI.2018.2820382](https://doi.org/10.1109/TMI.2018.2820382)]
 - 32 **Deng H**, Wang X, Cai C, Luo J, Ma C. Machine-learning enhanced photoacoustic computed tomography in a limited view configuration. In: Yuan XC, Carney PS, Shi K, Somekh MG, editors. *Advanced Optical Imaging Technologies II. SPIE* 2019; 111860J [DOI: [10.1117/12.2539148](https://doi.org/10.1117/12.2539148)]
 - 33 **Vu T**, Li M, Humayun H, Zhou Y, Yao J. A generative adversarial network for artifact removal in photoacoustic computed tomography with a linear-array transducer. *Exp Biol Med (Maywood)* 2020; **245**: 597-605 [PMID: 32208974 DOI: [10.1177/1535370220914285](https://doi.org/10.1177/1535370220914285)]
 - 34 **Gao Y**, Wang K, An Y, Jiang SX, Meng H, Tian J. Non model-based bioluminescence tomography using a machine-learning reconstruction strategy. *Optica* 2018; **5**: 1451-1454 [DOI: [10.1364/OPTICA.5.001451](https://doi.org/10.1364/OPTICA.5.001451)]
 - 35 **Guo L**, Liu F, Cai C, Liu J, Zhang G. 3D deep encoder-decoder network for fluorescence molecular tomography. *Opt Lett* 2019; **44**: 1892-1895 [PMID: 30985768 DOI: [10.1364/OL.44.001892](https://doi.org/10.1364/OL.44.001892)]
 - 36 **Zhang Z**, Cai M, Gao Y, Shi X, Zhang X, Hu Z, Tian J. A novel Cerenkov luminescence tomography approach using multilayer fully connected neural network. *Phys Med Biol* 2019; **64**: 245010 [PMID: 31770734 DOI: [10.1088/1361-6560/ab5bb4](https://doi.org/10.1088/1361-6560/ab5bb4)]
 - 37 **Li DS**, Chen CX, Li JF, Yan Q. Reconstruction of fluorescence molecular tomography based on graph convolution networks. *J Opt* 2020; **22**: 045602 [DOI: [10.1088/2040-8986/ab76a5](https://doi.org/10.1088/2040-8986/ab76a5)]

- 38 **Yoo J**, Sabir S, Heo D, Kim KH, Wahab A, Choi Y, Lee SI, Chae EY, Kim HH, Bae YM, Choi YW, Cho S, Ye JC. Deep Learning Diffuse Optical Tomography. *IEEE Trans Med Imaging* 2020; **39**: 877-887 [PMID: 31442973 DOI: 10.1109/TMI.2019.2936522]
- 39 **Cong W**, Wang G, Kumar D, Liu Y, Jiang M, Wang L, Hoffman E, McLennan G, McCray P, Zabner J, Cong A. Practical reconstruction method for bioluminescence tomography. *Opt Express* 2005; **13**: 6756-6771 [PMID: 19498692 DOI: 10.1364/OPEX.13.006756]
- 40 **Darne C**, Lu Y, Sevick-Muraca EM. Small animal fluorescence and bioluminescence tomography: a review of approaches, algorithms and technology update. *Phys Med Biol* 2014; **59**: R1-64 [PMID: 24334634 DOI: 10.1088/0031-9155/59/1/R1]



Breast dynamic contrast-enhanced-magnetic resonance imaging and radiomics: State of art

Alessia Orlando, Mariangela Dimarco, Roberto Cannella, Tommaso Vincenzo Bartolotta

ORCID number: Alessia Orlando [0000-0001-9048-1730](https://orcid.org/0000-0001-9048-1730); Mariangela Dimarco [0000-0003-0931-2302](https://orcid.org/0000-0003-0931-2302); Roberto Cannella [0000-0002-3808-0785](https://orcid.org/0000-0002-3808-0785); Tommaso Vincenzo Bartolotta [0000-0002-8808-379X](https://orcid.org/0000-0002-8808-379X).

Author contributions: Orlando A and Dimarco M wrote and revised the manuscript for important intellectual content; Cannella R and Bartolotta TV made critical revisions related to important intellectual content of the manuscript; all the authors approved the final version of the article.

Conflict-of-interest statement: No conflict of interests.

Open-Access: This article is an open-access article that was selected by an in-house editor and fully peer-reviewed by external reviewers. It is distributed in accordance with the Creative Commons Attribution NonCommercial (CC BY-NC 4.0) license, which permits others to distribute, remix, adapt, build upon this work non-commercially, and license their derivative works on different terms, provided the original work is properly cited and the use is non-commercial. See: <http://creativecommons.org/licenses/by-nc/4.0/>

Manuscript source: Invited

Alessia Orlando, Mariangela Dimarco, Roberto Cannella, Tommaso Vincenzo Bartolotta, Section of Radiology - BiND, University Hospital "Paolo Giaccone", Palermo 90127, Italy

Tommaso Vincenzo Bartolotta, Department of Radiology, Fondazione Istituto Giuseppe Giglio, Ct.da Pietrapollastra, Palermo 90015, Italy

Corresponding author: Tommaso Vincenzo Bartolotta, MD, PhD, Associate Professor, Section of Radiology - BiND, University Hospital "Paolo Giaccone", Via Del Vespro 129, Palermo 90127, Italy. tommasovincenzo.bartolotta@unipa.it

Abstract

Breast cancer represents the most common malignancy in women, being one of the most frequent cause of cancer-related mortality. Ultrasound, mammography, and magnetic resonance imaging (MRI) play a pivotal role in the diagnosis of breast lesions, with different levels of accuracy. Particularly, dynamic contrast-enhanced MRI has shown high diagnostic value in detecting multifocal, multicentric, or contralateral breast cancers. Radiomics is emerging as a promising tool for quantitative tumor evaluation, allowing the extraction of additional quantitative data from radiological imaging acquired with different modalities. Radiomics analysis may provide novel information through the quantification of lesions heterogeneity, that may be relevant in clinical practice for the characterization of breast lesions, prediction of tumor response to systemic therapies and evaluation of prognosis in patients with breast cancers. Several published studies have explored the value of radiomics with good-to-excellent diagnostic and prognostic performances for the evaluation of breast lesions. Particularly, the integrations of radiomics data with other clinical and histopathological parameters have demonstrated to improve the prediction of tumor aggressiveness with high accuracy and provided precise models that will help to guide clinical decisions and patients management. The purpose of this article is to describe the current application of radiomics in breast dynamic contrast-enhanced MRI.

Key words: Radiomics; Texture analysis; Magnetic resonance imaging; Dynamic contrast-enhanced-magnetic resonance imaging; Breast; Cancer

©The Author(s) 2020. Published by Baishideng Publishing Group Inc. All rights reserved.

manuscript

Received: June 1, 2020**Peer-review started:** June 1, 2020**First decision:** June 5, 2020**Revised:** June 17, 2020**Accepted:** June 20, 2020**Article in press:** June 20, 2020**Published online:** June 28, 2020**P-Reviewer:** Li JF**S-Editor:** Wang JL**L-Editor:** A**E-Editor:** Xing YX

Core tip: Dynamic contrast-enhanced-magnetic resonance imaging (DCE-MRI) has been evaluated in most of radiomics studies on breast cancers. However, heterogeneity in study designs related to magnetic field, contrast media used, and software available to perform radiomics challenge the comparisons of available results. In this review we will focus on the following applications of radiomics in breast DCE-MRI: characterization of breast lesions, prediction of breast cancer histological types, correlation with receptor status, prediction of lymph node metastases, prediction of tumor response to neoadjuvant systemic therapy, prognosis and recurrence risks.

Citation: Orlando A, Dimarco M, Cannella R, Bartolotta TV. Breast dynamic contrast-enhanced-magnetic resonance imaging and radiomics: State of art. *Artif Intell Med Imaging* 2020; 1(1): 6-18

URL: <https://www.wjgnet.com/2644-3260/full/v1/i1/6.htm>

DOI: <https://dx.doi.org/10.35711/aimi.v1.i1.6>

INTRODUCTION

Breast cancer represents the most common malignancy in women^[1]. It is estimated that 268600 US women were newly diagnosed with invasive breast cancer in 2019, and that 41760 US women died of breast cancer^[1]. Because of its incidence and clinical impact, early and accurate tumor detection with imaging is of utmost importance. Ultrasound, mammography, and magnetic resonance imaging (MRI) play a pivotal role in the diagnosis of breast lesions, with different levels of accuracy. Particularly, MRI has shown a greater sensitivity than mammography (92% vs 75%, respectively)^[2] and ultrasound (90% vs 39% and 49% of ultrasound alone or associated with mammography, respectively)^[3] for the diagnosis of breast cancer. Thanks to the ability to provide both morphologic and hemodynamic features, dynamic contrast-enhanced MRI (DCE-MRI) provides high sensitivity (over 90%) in the detection of breast cancer, although specificity for lesion characterization is still suboptimal (72%)^[2,3]. DCE-MRI has shown high diagnostic value in detecting multifocal, multicentric, or contralateral disease not diagnosed on physical examination, mammography or ultrasound, recognition of ductal carcinoma *in situ* (DCIS), evaluation of treatment response to neoadjuvant chemotherapy, detection of occult primary breast cancer in patients with metastatic axillary nodes (the so-called “CUP syndrome”), and detection of cancer in dense breast tissue^[4].

Recently, an increasing interest for the clinical utility of quantitative imaging is developing. In this scenario, radiomics is emerging as a promising tool for quantitative tumor evaluation. Radiomics allow to extract quantitative data from medical images that be combined to provide models for clinical decision support^[5].

The purpose of this article in to describe the current application of radiomics in breast dynamic contrast-enhanced MRI.

CONCEPTS OF RADIOMICS ANALYSIS

Radiomics is a complex process that articulates into distinct steps, including: Acquisition of images, tumor segmentation, feature extraction, exploratory analysis, and model building. The first step of radiomics is acquisition of high-quality images. Potentially, all the radiologic techniques may be used for radiomics analysis. In the field of breast imaging, all the techniques (mammography, ultrasound, and MRI) have shown promising results in radiomics studies. Particularly, breast MRI is commonly performed using T2-weighted images acquired to characterized diseased tissue, diffusion-weighted imaging (DWI), and apparent diffusion coefficient (ADC) that have an important clinical role in the evaluation of breast lesions, and post-contrast dynamic imaging that are mandatory for the differentiation of benign and malignant lesions. Next step is the segmentation of the lesion (Figure 1), with selection of a region of interest (ROI) and delineation of the borders of its volume. The ROI selection process is not yet standardized and it is linked to high levels of variability between different studies, as it can include the whole tumor or single slice segmentation^[6].

Feature extraction may be performed with different radiomics software that are able

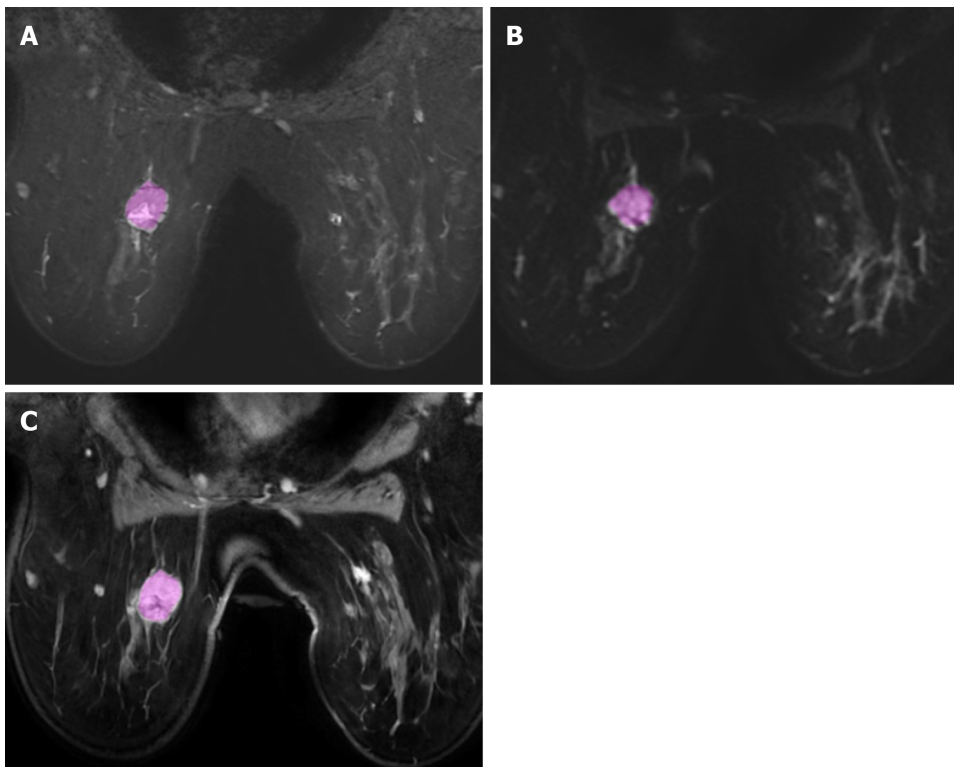


Figure 1 Examples of lesion segmentation in dynamic contrast-enhanced-magnetic resonance imaging in a 70-year-old woman with 3.0 cm breast cancer lesion. A: Short tau inversion recovery; B: Diffusion-weighted imaging; C: Contrast-enhanced sequences.

to provide a large number of quantitative features. Quantitative radiomics features can be divided into morphological (basic features that describe the shape of the ROI and its geometric properties such as volume, diameter, sphericity), and statistical (calculated using statistical methods). These features can be further divided into first order (histogram-based) features that describe the distribution of voxel values without considering the spatial relationships (*i.e.* mean, median, skewness, kurtosis, and entropy); second order texture features that are obtained by calculating the relationships between neighboring voxels (*i.e.* grey level co-occurrence matrix, grey level run length matrix, grey level size zone matrix); and third order features that are obtained by statistical methods after applying filters or mathematical transforms to the images (*i.e.* wavelet transform, Laplacian transforms of Gaussian-filtered images)^[7].

The next and last step in the workflow is building the statistical radiomics model with the purpose to predict an outcome or response variables. Different models can be evaluated to predict a specific outcome or a response using a variety of classifiers.

APPLICATION OF RADIOMICS IN BREAST DCE-MRI

The emerging field of radiomics was applied to several breast imaging modalities^[8,9]. Nevertheless, DCE-MRI was used in most studies but with heterogeneity in study designs related to magnetic field (1.5T or 3T), contrast media used, and software available to perform radiomics^[10]. In this review we will focus the following applications of radiomics in breast DCE-MRI: Characterization of breast lesions, prediction of breast cancer histological types, correlation with receptor status, prediction with lymph node metastases, prediction of tumor response to neoadjuvant systemic therapy (NST), prognosis and recurrence risks.

Characterization of breast lesions

Radiomics features extracted from multiple MRI sequences have shown to be helpful in establishing predictive models that could help differentiate between benign and malignant breast lesions. Several radiomics models were proposed with promising results, with most texture analysis performed on post-contrast T1-weighted images, alone or in association with other sequences (T2w and ADC maps).

Since the very first studies in literature, conducted on small populations analyzing

different types of features extracted (dynamic, textural, spatio-temporal) from breast contrast-enhanced MRI, the dynamic subset revealed the best performance for the characterization of breast lesions for Fusco *et al*^[11]. Testing a multi-layer perceptron neural network classifier, with an automatic ROI segmentation or ROI classification, they found an accuracy for dynamic features subset of about 80%, with the major discrimination power in differentiating benign from malignant lesions found for “basal signal”, “sum of intensities difference”, “relative enhancement slope” and “relative enhancement” features.

Nie *et al*^[12] investigated the utility of breast lesions morphology and textural features for differentiating between benign and malignant lesions, with both manual and automated segmentation and performing diagnostic feature selection using artificial neural network. They found that among morphological features “Compactness” and “Normalized Radial Length Entropy” showed significant differences between the benign and the malignant groups, whereas among “Gray Level Co-occurrence Matrices” texture features, “Gray Level Entropy” and “Gray Level Sum Average” were significantly lower in benign compared to malignant lesions. Analyzing the diagnostic performance of individual and combined features the highest AUROC (0.86) was obtained combining the following 6 features: Compactness, NRL entropy, volume, gray level entropy, gray level sum average, and homogeneity. Entropy is an important feature associated with tumor aggressiveness. It represents one of the most reliable feature to distinguish malignant from benign lesions, with the irregularity of texture reflecting the tumor heterogeneity, and tumor aggressiveness^[13-15]. Gibbs *et al*^[16], testing texture analysis with the aim to characterize breast lesions, concluded that texture features of variance, sum entropy, and entropy were the most significant when discriminating between benign and malignant lesions.

Radiomics model of quantitative pharmacokinetic maps demonstrated a strong ability to discriminate between benign and malignant breast lesions, directly reflecting the physiological properties of tissues, such as vessel permeability, perfusion, and volume of the extravascular/extracellular space^[13,17]. Nagarajan *et al*^[18] studied texture features extracted from the lesion enhancement pattern on all five post-contrast images, thus using a dynamic texture quantification approach. In this study, the highest AUROC (0.82) was achieved with texture features responsible for capturing aspects of lesion heterogeneity. Gibbs *et al*^[19] also assessed the efficacy of radiomics analysis with quantitative pharmacokinetic maps in small breast lesions (less than 1 cm). Their results showed that texture parameters calculated from initial enhancement, overall enhancement, and area under the enhancement curve maps offered similar discriminatory power in discriminating benign and malignant breast lesions, whereas texture features obtained from washout maps did not demonstrate any diagnostic value^[19].

While many studies focused on discriminatory capacities of specific texture features extracted from combining quantitative pharmacokinetic parameters of DCE-MRI sequences, few studies used a multiparametric approach analyzing also feature extracted from other sequences, such as T2-weighted and T1-weighted imaging, diffusion kurtosis imaging, and ADC maps. The multimodal MRI-based radiomics model developed by Zhang *et al*^[13] demonstrated higher diagnostic ability for differentiating benign and malignant breast lesions [Area under curve (AUC) = 0.921], increasing the discriminatory power of radiomics features extracted from DCE pharmacokinetic parameter maps alone (AUC = 0.836). In particular, analyzing textural features included in the radiomics models, malignant breast lesions had higher entropy and nonuniformity than benign lesions. The multiview IsoSVM (hybrid isomap and support vector machine) model applied by Parekh *et al*^[20] to radiomics features extracted from multiparametric breast MR imaging at 3T, classified benign and malignant breast tumors with an AUROC of 0.91, sensitivity of 93%, and specificity of 85%. In this study, entropy features maps obtained demonstrated significantly higher entropy for malignant than benign lesions on post contrast DCE-MRI and ADC maps^[20]. The same authors developed a multiparametric imaging radiomics framework for extraction of first and second order radiomics features from multiparametric radiological datasets which provided a 9%-28% increase in AUROC over single radiomics parameters. Similar results were reported by Bhooshan *et al*^[21], who found the better performance applying a multiparametric feature vector, with T2-weighted MRI textural features added to DCE-MRI kinetic ones.

Radiomics features extracted from unenhanced MRI sequences were also evaluated for the prediction of malignancies. In the study of Bickelhaupt *et al*^[22] an unenhanced, abbreviated DWI protocol (ueMRI), including T2-weighted, DWI, DWI with background suppression sequences, and corresponding ADC maps, was used to test three machine learning classifiers including univariate mean ADC model,

unconstrained radiomics model, constrained radiomics model with mandatory inclusion of mean ADC. The last two radiomics classifiers were found to be able to distinguish benign from malignant lesions more accurately (AUROC of 0.842 and 0.851) than the mean ADC parameter alone (AUROC of 0.774)^[22]. Nevertheless, the performance remained lower than that of the experienced breast radiologist using standard DCE-MRI protocol^[22]. ADC radiomics features reflect the heterogeneity of diffusion in tumors, relative to the cell density and the microenvironment distribution inside the lesion. Hu *et al*^[23] found that ADC radiomics score was more accurate than ADC values alone and they developed a prediction model based on ADC radiomics, pharmacokinetics and clinical features, which showed good diagnostic performance in differentiating benign and malignant lesions classified as BI-RADS 4. A radiomics model based on kurtosis diffusion-weighted imaging was evaluated by Bickelhaupt *et al*^[24] who conducted a multicentric and prospective study on BI-RADS 4 and 5 lesions, by using MRI scanners from different vendors, showing reliable results, with a real benefit for BI-RADS 4a and 4b breast lesions.

Finally, more recent studies are using DCE-MRI focusing their attention on peritumoural tissues inclusion during segmentation. Zhou *et al*^[25] found that the smallest bounding box, that included a small amount of peritumoural tissue adjacent to the tumor, had higher accuracy compared to tumor alone or larger input boxes.

Prediction of breast cancer histological types

Few studies employed radiomics models and texture analysis to distinguish between the heterogeneous histopathologic subtypes of breast cancer and entropy-based features from the co-occurrence matrix appear to be most crucial, with promising results. Invasive ductal (IDC) and lobular (ILC) carcinoma are the most common pathologic types. The different growth patterns may manifest with different heterogeneity of internal enhancement in DCE-MRI, and could be the basis to differentiate between these two histological types by means of textural analysis^[14,26]. Holli *et al*^[26] found that the co-occurrence matrix texture features group was statistically significant different between ductal and lobular invasive cancers on DCE-MR images. Similar conclusions were reported by Waugh *et al*^[14] analyzing differences between IDC, ILC and in situ ductal carcinoma (DCIS). Chou *et al*^[27] investigated the potential role of radiomics in classifying DCIS nuclear grade and found that only one heterogeneity metric, surface-to-volume ratio from the “shape and morphology” metrics group, was significantly different between “high nuclear grade” and “non-high nuclear grade” DCIS.

Correlation with receptor status and molecular subtypes

Expression of Ki-67, estrogen receptor (ER), progesterone receptor, human epidermal growth factor 2 receptor (HER2) are crucial factors to differentiate breast cancers into four main molecular subtypes (Luminal A, Luminal B, Her2 over-expressing, and triple negative, TN) with different outcomes and therapeutic strategies. According to the molecular subtypes different strategies, including surgery, adjuvant or neoadjuvant therapies, can be undertaken^[28-31]. Current assessment of molecular subtypes is mostly based on immunohistochemistry (IHC)^[32]. When IHC is tested in tissue specimens obtained by needle biopsy, could be not totally representative of the entire tumor or provide inconclusive results due to insufficient material. In this setting, according to prior studies, DCE-MRI may provide information suggesting the molecular subtype of breast cancer. In 2018, the American Joint Committee on Cancer updated the breast cancer staging guidelines to add other cancer characteristics to the TNM system to determine a cancer’s stage, including receptorial status^[33]. When developing a treatment plan, a correct assessment of receptorial status is crucial. Several published studies revealed that rim enhancement, heterogeneous internal enhancement, and peritumoural edema are more frequently associated with TN than Luminal subtypes^[34,35]. In the study of Blaschke *et al*^[36] HER2-enriched tumors showed the percent volume with > 50% and > 100% early phase uptake higher than Luminal A/B lesions at kinetic assessment. TN tends to be more frequently round in shape^[32,37], Her2 cancers with smooth margins than other subtypes^[37]. Controversial results were reported for diffusion-weighted imaging, suggesting that high ADC values are associated with HER2 subtypes^[38] or with Luminal A^[39], and for spectroscopy, suggesting that high values of tCho are statistically correlated to the TN subtype for some authors^[39,40], and with non-TN and Luminal B^[41].

Several studies investigated the relationship between radiomics MRI features and breast cancer receptor status^[42-44]. Wu *et al*^[45] reported only few features significantly associated with Luminal A, Luminal B or TN in their study cohorts for distinguishing different molecular subtypes of breast cancers. Radiomics analysis conducted by Li

et al^[46] showed a statistically significant trend for the relationship between enhancement textures (entropy) and molecular subtypes in the task of distinguishing between ER+ versus ER-. Indeed, heterogeneous nature of contrast uptake within the breast tumor is related to molecular subtype. Similar observations were reported by Waugh *et al*^[44], revealing that HER2-enriched and TN cancers showed a significant increase in entropy value. In the study of Chang *et al*^[47] the quantitative region-based features extracted from breast DCE-MRI were used to interpret the intra-tumoral heterogeneity and correlated with ER, HER2, and TNBC, with better performance than morphological features (texture features and shape feature) and the pharmacokinetic model. Fan *et al*^[48] investigated the use of features extracted from DCE-MRI for the prediction of the molecular subtypes of breast cancer and observed low kurtosis and skewness for the luminal A subtype, the highest enhancement values in the normal breasts for Her 2 subtypes and the lowest for luminal A and luminal B tumors. Furthermore, other studies suggested the value of the heterogeneity of the surrounding parenchyma, including background parenchymal enhancement features in differentiating TN breast cancers from others, as observed by Wang *et al*^[49]. The evaluation of both peritumoral and intratumoral features allowed to identify HER2 subtype with better accuracy than intratumoral features alone in the study of Braman *et al*^[50]. According to the results of Leithner *et al*^[51] radiomics analysis from DWI with ADC mapping allows evaluation of breast cancer receptor status and molecular subtyping. For differentiating ER positive breast cancer molecular subtypes (Luminal A vs Luminal B) the two most discriminative texture parameters extracted from the dynamic T1-weighted sequences by Holli-Helenius *et al*^[52] were sum entropy and sum variance, which also showed positive correlation with higher Ki-67 index.

High Ki-67 expression is a well-known prognostic factor, related to better neo-adjuvant therapy response but poorer prognosis. Assessment of Ki-67 based on immunohistochemistry on tissue specimens obtained by needle biopsy sample may not be representative of the whole tumor because of the relatively small tissue sample size and tumor heterogeneity. In the attempt to predict the expression of Ki-67 several studies have explored the potential of radiomics imaging features, with promising results. In their retrospective study, Ma *et al*^[53] showed that texture features extracted on the first post-contrast images were associated with breast cancer Ki-67 expression. Similar results were obtained by Juan *et al*^[54]. A correlation between Ki-67 expression and radiomics features were observed also performing features extraction from T2-weighted images^[55] and ADC maps^[56].

Prediction of lymph node status

Involvement of axillary lymph nodes (LN) in patients with breast cancers represents a crucial prognostic factor, as it guides therapeutic management. Non-invasive methods to preoperatively evaluate LN metastasis are highly needed. Some promising studies suggested that radiomics models could be able to achieve this objective. In recent studies, specific lesions textural features extracted from anatomical and functional MRI images, improved the performance of radiomics models in predicting LN metastasis^[57,58]. Liu *et al*^[59] demonstrated that DCE-MRI radiomics features, particularly features extracted from peritumoral regions, associated with clinico-pathologic informations were able to predict LN metastasis in breast cancer patients. Indeed, the area surrounding tumors, is thought to carry informations such as peritumoral lymphatic vessel invasion, lymphocytic infiltration, and edema^[59,60]. Other authors reported that the best results were obtained when the features extraction was performed in the strongest phases of tumor enhancement, probably because it shows more clearly the lesion boundaries and better reflects the tumor heterogeneity and invasiveness^[61]. The radiomics nomogram developed by Han *et al*^[62] demonstrated excellent performance to predict LN metastases, and good ability in distinguishing the number of metastatic LNs. Similar performances were reported by several other evidences^[59,63-65]. Finally, only very few studies evaluated texture analysis in identified index lymph nodes in postcontrast T1-weighted images, concluding that morphologic features were more predictive than kinetic and texture features^[66,67].

Prediction of tumor response to neo-adjuvant therapy

NST is often the first line treatment for those patients diagnosed with locally advanced breast cancer, with several potential advantages, including the reduction of tumor size to allow breast-conservative surgery instead of mastectomy, as well as a prognostic indicator^[68]. The pathologic complete response (pCR) rate range from 0.3%–38.7%, depending on cancer subtype and breast cancer stage^[69]. Early identification of patients who are not likely to achieve pCR is crucial as they could benefit from changes to their initial NST regimens. DCE-MRI is considered as the most reliable technique for

evaluating the responses to NST. According to a meta-analysis based on 25 studies, breast MRI had high specificity (up to 90.7%), but low sensitivity (63.1%) in predicting pathologic complete remission after preoperative therapy in patients with breast cancer^[70]. According to another recent meta-analysis, accuracy in detection of residual malignancy with breast MRI varies also in consideration of the treatment type, with AUC values ranging from 0.83 to 0.89, and on the basis of response definition, for instance volume reduction, absence of enhancement or enhancement equal or less than breast parenchyma^[71,72]. The wide heterogeneity of studies, with controversial results, suggests to standardize definitions and primary endpoints to produce clinically significant results^[73].

The identification of pCR is still a challenge and according with several studies, radiomics can be helpful in a non-invasive prediction of response to NST^[74-78]. In most studies, GLCM features were the most predictive of therapy response, particularly entropy^[79-81]. Noteworthy, in the study of Parikh *et al.*^[82], responders to NST showed increase in lesion homogeneity after one round of therapy. Cao *et al.*^[83] demonstrated that texture analysis may help to improve the performance of post-NST MRI in identifying pCR in mass-like breast cancer, showing that entropy was an independent risk factor. Intratumoral spatial heterogeneity at perfusion MRI appeared to be an independent prognostic factor of recurrence-free-survival in patients with locally advanced breast cancers treated with NST^[84]. Significant differences between pCR and non-pCR patients were found for texture parameters also by Fusco *et al.*^[85]. Peritumoral region includes prognostic informations, such as angiogenic and lymphangiogenic activity, peritumoral invasion of lymphatics and blood vessels and peritumoral lymphocytic infiltration^[86]. In their retrospective study, Braman *et al.*^[87] demonstrated that with combined intratumoral and peritumoral radiomics approach, analyzing textural features extracted from T1-weighted contrast-enhanced MRI scans, it is possible to successfully predict pCR to NST from pretreatment breast DCE-MRI, both with and without a priori knowledge of receptor status. Later, the same authors, confirmed that an intratumoral and peritumoral imaging signature was capable to predict the response to preroperative targeted therapy in another retrospective study conducted on HER2-positive breast cancers, highlighting again the relationship between immune-response and the peritumoral environment^[50]. Zhou *et al.*^[88] investigated the role of wavelet-transformed textures, which can provide comprehensive spatial, and frequency distributions for characterizing intratumoral and peritumoral regions in terms of low and high frequency signals. In their study wavelet-transformed textures outperformed volumetric and peripheral textures in the radiomics MRI prediction of pCR to NST for patients with locally advanced breast cancers.

DWI is considerably sensitive to NST-induced intratumoral changes, resulting in an additional value when associated to contrast-enhanced MRI in radiomics models. Radiomics signatures combining multi-parametric MRI achieved a good performance for predicting complete response in BC, in both Luminal and TN cancers, in the study conducted by Liu *et al.*^[89]. With a radiomics signature, combining radiomics features from DCE-MRI and ADC maps, Chen *et al.*^[90] obtained similar results, with a higher performance than the models with DCE-MRI or ADC maps alone, in predicting PCR.

Sentinel lymph node biopsy has replaced axillary lymph node dissection in patients who convert to node-negative status after NST. Several studies assessed whether breast MRI can be used to assess lymph node residual metastasis after NST allowing breast cancer patients to avoid unnecessary axillary surgery. In the study of Hyun *et al.*^[91], DCE-MRI was able to rule out the presence of advanced nodal disease with a NPV of 94% in NAC patients. Nevertheless, in the work of Mattingly *et al.*^[92], post-treatment MRI and surgical pathologic findings revealed a slight strength of agreement and DCE-MRI revealed specificity and sensitivity of 63% and 55%, respectively. Ha *et al.*^[93] found different results, with sensitivity and specificity of 57% and 72%, with positive estrogen receptor status significantly associated with misdiagnosis by MRI. These latter evidences, revealing that post-treatment MRI findings were not exactly predictive of residual axillary disease, suggest to use DCE-MRI results with caution when planning treatment and to avoid omitting sentinel lymph node biopsy or axillary lymph node dissection for staging in women determined to be node-positive pre-treatment. In this setting, convolutional neural networks (CNN), were employed to predict the likelihood of axillary LN metastasis and NAC treatment response, using MRI datasets prior to initiation of NAC in few studies with controversial results^[79,94-96]. Ha *et al.*^[96] reported an accuracy of 83% with AUC of 0.93 for CNN in predicting axillary response. Nevertheless, in the study of Golden *et al.*^[79] the GLCM texture features extracted from pre- chemotherapy MRI was able to predict pCR and residual lymph node metastasis with an AUC of 0.68.

Prognosis

Radiomics models demonstrated promising results in predicting cancer prognosis of patients with tumors of various organs, reporting that several texture features, such as uniformity and entropy, can be used in risk stratification^[15,97,98]. By using the genomic-based scores for the multigene assays MammaPrint, Oncotype DX, and PAM50 as the reference standards, Li *et al*^[99] demonstrated that breast MRI radiomics show a promising role for image-based phenotyping in assessing the risk of recurrence. Noteworthy, enhancement texture features were consistently associated with recurrence score, highlighting how microvascular density and/or central necrosis, responsible of tumor heterogeneity, play an important biological role in recurrence. Other authors confirmed these results, finding that tumors with higher entropy on T2-weighted images and lower entropy on T1w subtraction images were associated with poorer recurrence-free survival^[15]. A CNN developed by Ha *et al*^[100] was able to predict with an accuracy of up to 84%, the Oncotype Dx Recurrence Score (ODRS), an expensive but validated recurrence score, recommended by American Society of Clinical Oncology guidelines to decide on adjuvant systemic chemotherapy in ER+/HER-/node negative lesions^[101]. Nevertheless, this result was not confirmed by Saha *et al*^[102], who tested two machine learning-based models, finding only a moderate association between imaging and ODRS. The study of Park *et al*^[103] was the first performed, using ROIs drawn on entire tumors, to demonstrate that a radiomics signature can estimate survival in patients with BC. They generated a multivariate feature vector based on morphologic, histogram texture, and GLCM texture features to stratify patients at risk for recurrence. They also showed that a combined radiomics-clinical-pathological nomogram achieved superior prognostic performance than either the Rad-score-only or the clinico-pathological nomograms. Nevertheless, controversial results were recently reported applying radiomics models to predict prognosis for TN (triple-negative) breast cancers^[104,105]. While in the study conducted by Kim *et al*^[105] the radiomics score was significantly associated with worse disease free survival, but comparable in performance with the clinico-pathologic model, in both the training and validation sets, the work performed by Koh *et al*^[104] showed that their Radiomics model was able to predict systemic recurrence better than the Clinical model only in the training set.

LIMITATIONS AND FUTURE APPLICATIONS

Radiomics techniques require further studies, as they have not yet achieved widespread, demonstrated and accepted, clinical relevance and applicability. The main challenge is the standardization of MRI acquisition protocol, method of segmentation, feature extraction and selection, or classification. Another hurdle is the current lack of evidences regarding reproducibility of feature extraction systems and radiomics models. Furthermore, most studies are retrospectively designed, with relatively small sample size and wide methodological differences. Larger and prospective studies, with standardized radiomics methods are needed to prove and improve potential clinical applications of radiomics in BC. Further studies are necessary to prove and understand the relationships between image-derived texture features and histopathologic or even genomic expression data. The main future directions include the correlation between proteomic and genomic tumor analyses with radiomics features, through the field of radiogenomics. These last investigations could have a potential role in explaining tumor biology, contributing in the main future objective of personalized diagnosis and treatment of breast cancer patients.

REFERENCES

- 1 Siegel RL, Miller KD, Jemal A. Cancer statistics, 2019. *CA Cancer J Clin* 2019; **69**: 7-34 [PMID: 30620402 DOI: 10.3322/caac.21551]
- 2 Zhang Y, Ren H. Meta-analysis of diagnostic accuracy of magnetic resonance imaging and mammography for breast cancer. *J Cancer Res Ther* 2017; **13**: 862-868 [PMID: 29237918 DOI: 10.4103/jcr.t.JCRT_678_17]
- 3 Kuhl CK, Schrading S, Leutner CC, Morakkabati-Spitz N, Wardelmann E, Fimmers R, Kuhn W, Schild HH. Mammography, breast ultrasound, and magnetic resonance imaging for surveillance of women at high familial risk for breast cancer. *J Clin Oncol* 2005; **23**: 8469-8476 [PMID: 16293877 DOI: 10.1200/JCO.2004.00.4960]
- 4 Menezes GL, Knuttel FM, Stehouwer BL, Pijnappel RM, van den Bosch MA. Magnetic resonance imaging in breast cancer: A literature review and future perspectives. *World J Clin Oncol* 2014;

- 5: 61-70 [PMID: 24829852 DOI: 10.5306/wjco.v5.i2.61]
- 5 **Gillies RJ**, Kinahan PE, Hricak H. Radiomics: Images Are More than Pictures, They Are Data. *Radiology* 2016; **278**: 563-577 [PMID: 26579733 DOI: 10.1148/radiol.2015151169]
 - 6 **Tagliafico AS**, Piana M, Schenone D, Lai R, Massone AM, Houssami N. Overview of radiomics in breast cancer diagnosis and prognostication. *Breast* 2020; **49**: 74-80 [PMID: 31739125 DOI: 10.1016/j.breast.2019.10.018]
 - 7 **Rizzo S**, Botta F, Raimondi S, Origi D, Fanciullo C, Morganti AG, Bellomi M. Radiomics: the facts and the challenges of image analysis. *Eur Radiol Exp* 2018; **2**: 36 [PMID: 30426318 DOI: 10.1186/s41747-018-0068-z]
 - 8 **Valdora F**, Houssami N, Rossi F, Calabrese M, Tagliafico AS. Rapid review: radiomics and breast cancer. *Breast Cancer Res Treat* 2018; **169**: 217-229 [PMID: 29396665 DOI: 10.1007/s10549-018-4675-4]
 - 9 **Rogers W**, Thulasi Seetha S, Refae TAG, Lieverse RIY, Granzier RWY, Ibrahim A, Keek SA, Sanduleanu S, Primakov SP, Beuque MPL, Marcus D, van der Wiel AMA, Zerka F, Oberije CJG, van Timmeren JE, Woodruff HC, Lambin P. Radiomics: from qualitative to quantitative imaging. *Br J Radiol* 2020; **93**: 20190948 [PMID: 32101448 DOI: 10.1259/bjr.20190948]
 - 10 **Antropova N**, Huynh BQ, Giger ML. A deep feature fusion methodology for breast cancer diagnosis demonstrated on three imaging modality datasets. *Med Phys* 2017; **44**: 5162-5171 [PMID: 28681390 DOI: 10.1002/mp.12453]
 - 11 **Fusco R**, Sansone M, Sansone C, Petrillo A. Segmentation and classification of breast lesions using dynamic and textural features in Dynamic Contrast Enhanced-Magnetic Resonance Imaging. *IEEE* 2012 [DOI: 10.1109/CBMS.2012.6266312]
 - 12 **Nie K**, Chen JH, Yu HJ, Chu Y, Nalcioglu O, Su MY. Quantitative analysis of lesion morphology and texture features for diagnostic prediction in breast MRI. *Acad Radiol* 2008; **15**: 1513-1525 [PMID: 19000868 DOI: 10.1016/j.acra.2008.06.005]
 - 13 **Zhang Q**, Peng Y, Liu W, Bai J, Zheng J, Yang X, Zhou L. Radiomics Based on Multimodal MRI for the Differential Diagnosis of Benign and Malignant Breast Lesions. *J Magn Reson Imaging* 2020 [PMID: 32061014 DOI: 10.1002/jmri.27098]
 - 14 **Waugh SA**, Purdie CA, Jordan LB, Vinnicombe S, Lerski RA, Martin P, Thompson AM. Magnetic resonance imaging texture analysis classification of primary breast cancer. *Eur Radiol* 2016; **26**: 322-330 [PMID: 26065395 DOI: 10.1007/s00330-015-3845-6]
 - 15 **Kim JH**, Ko ES, Lim Y, Lee KS, Han BK, Ko EY, Hahn SY, Nam SJ. Breast Cancer Heterogeneity: MR Imaging Texture Analysis and Survival Outcomes. *Radiology* 2017; **282**: 665-675 [PMID: 27700229 DOI: 10.1148/radiol.2016160261]
 - 16 **Gibbs P**, Turnbull LW. Textural analysis of contrast-enhanced MR images of the breast. *Magn Reson Med* 2003; **50**: 92-98 [PMID: 12815683 DOI: 10.1002/mrm.10496]
 - 17 **Kim SG**, Freed M, Leite APK, Zhang J, Seuss C, Moy L. Separation of benign and malignant breast lesions using dynamic contrast enhanced MRI in a biopsy cohort. *J Magn Reson Imaging* 2017; **45**: 1385-1393 [PMID: 27766710 DOI: 10.1002/jmri.25501]
 - 18 **Nagarajan MB**, Huber MB, Schlossbauer T, Leinsinger G, Krol A, Wismüller A. Classification of Small Lesions in Breast MRI: Evaluating The Role of Dynamically Extracted Texture Features Through Feature Selection. *J Med Biol Eng* 2013; **33** [PMID: 24223533 DOI: 10.5405/jmbe.1183]
 - 19 **Gibbs P**, Onishi N, Sadinski M, Gallagher KM, Hughes M, Martinez DF, Morris EA, Sutton EJ. Characterization of Sub-1 cm Breast Lesions Using Radiomics Analysis. *J Magn Reson Imaging* 2019; **50**: 1468-1477 [PMID: 30916835 DOI: 10.1002/jmri.26732]
 - 20 **Parekh VS**, Jacobs MA. Integrated radiomic framework for breast cancer and tumor biology using advanced machine learning and multiparametric MRI. *NPJ Breast Cancer* 2017; **3**: 43 [PMID: 29152563 DOI: 10.1038/s41523-017-0045-3]
 - 21 **Bhooshan N**, Giger M, Lan L, Li H, Marquez A, Shimauchi A, Newstead GM. Combined use of T2-weighted MRI and T1-weighted dynamic contrast-enhanced MRI in the automated analysis of breast lesions. *Magn Reson Med* 2011; **66**: 555-564 [PMID: 21523818 DOI: 10.1002/mrm.22800]
 - 22 **Bickelhaupt S**, Paech D, Kickingeder P, Steudle F, Lederer W, Daniel H, Götz M, Gählerl N, Tichy D, Wiesenfarth M, Laun FB, Maier-Hein KH, Schlemmer HP, Bonekamp D. Prediction of malignancy by a radiomic signature from contrast agent-free diffusion MRI in suspicious breast lesions found on screening mammography. *J Magn Reson Imaging* 2017; **46**: 604-616 [PMID: 28152264 DOI: 10.1002/jmri.25606]
 - 23 **Hu B**, Xu K, Zhang Z, Chai R, Li S, Zhang L. A radiomic nomogram based on an apparent diffusion coefficient map for differential diagnosis of suspicious breast findings. *Chin J Cancer Res* 2018; **30**: 432-438 [PMID: 30210223 DOI: 10.21147/j.issn.1000-9604.2018.04.06]
 - 24 **Bickelhaupt S**, Jaeger PF, Laun FB, Lederer W, Daniel H, Kuder TA, Wuesthof L, Paech D, Bonekamp D, Radbruch A, Delorme S, Schlemmer HP, Steudle FH, Maier-Hein KH. Radiomics Based on Adapted Diffusion Kurtosis Imaging Helps to Clarify Most Mammographic Findings Suspicious for Cancer. *Radiology* 2018; **287**: 761-770 [PMID: 29461172 DOI: 10.1148/radiol.2017170273]
 - 25 **Zhou J**, Zhang Y, Chang KT, Lee KE, Wang O, Li J, Lin Y, Pan Z, Chang P, Chow D, Wang M, Su MY. Diagnosis of Benign and Malignant Breast Lesions on DCE-MRI by Using Radiomics and Deep Learning With Consideration of Peritumor Tissue. *J Magn Reson Imaging* 2020; **51**: 798-809 [PMID: 31675151 DOI: 10.1002/jmri.26981]
 - 26 **Holli K**, Lääperi AL, Harrison L, Luukkaala T, Toivonen T, Ryymin P, Dastidar P, Soimakallio S, Eskola H. Characterization of breast cancer types by texture analysis of magnetic resonance images. *Acad Radiol* 2010; **17**: 135-141 [PMID: 19945302 DOI: 10.1016/j.acra.2009.08.012]
 - 27 **Chou SS**, Gombos EC, Chikarmane SA, Giess CS, Jayender J. Computer-aided heterogeneity analysis in breast MR imaging assessment of ductal carcinoma in situ: Correlating histologic grade and receptor status. *J Magn Reson Imaging* 2017; **46**: 1748-1759 [PMID: 28371110 DOI: 10.1002/jmri.25712]
 - 28 **Goldhirsch A**, Wood WC, Coates AS, Gelber RD, Thürlimann B, Senn HJ; Panel members. Strategies for subtypes--dealing with the diversity of breast cancer: highlights of the St. Gallen International Expert Consensus on the Primary Therapy of Early Breast Cancer 2011. *Ann Oncol* 2011; **22**: 1736-1747 [PMID:

- 21709140 DOI: [10.1093/annonc/mdr304](https://doi.org/10.1093/annonc/mdr304)]
- 29 **Goldhirsch A**, Winer EP, Coates AS, Gelber RD, Piccart-Gebhart M, Thürlimann B, Senn HJ; Panel members. Personalizing the treatment of women with early breast cancer: highlights of the St Gallen International Expert Consensus on the Primary Therapy of Early Breast Cancer 2013. *Ann Oncol* 2013; **24**: 2206-2223 [PMID: [23917950](https://pubmed.ncbi.nlm.nih.gov/23917950/) DOI: [10.1093/annonc/mdt303](https://doi.org/10.1093/annonc/mdt303)]
 - 30 **Balic M**, Thomssen C, Würstlein R, Gnant M, Harbeck N. St. Gallen/Vienna 2019: A Brief Summary of the Consensus Discussion on the Optimal Primary Breast Cancer Treatment. *Breast Care (Basel)* 2019; **14**: 103-110 [PMID: [31798382](https://pubmed.ncbi.nlm.nih.gov/31798382/) DOI: [10.1159/000499931](https://doi.org/10.1159/000499931)]
 - 31 **Öztürk VS**, Polat YD, Soyder A, Tanyeri A, Karaman CZ, Taşkın F. The Relationship Between MRI Findings and Molecular Subtypes in Women With Breast Cancer. *Curr Probl Diagn Radiol* 2019 [PMID: [31351695](https://pubmed.ncbi.nlm.nih.gov/31351695/) DOI: [10.1067/j.cpradiol.2019.07.003](https://doi.org/10.1067/j.cpradiol.2019.07.003)]
 - 32 **Guiu S**, Michiels S, André F, Cortes J, Denkert C, Di Leo A, Hennessy BT, Sorlie T, Sotiriou C, Turner N, Van de Vijver M, Viale G, Loi S, Reis-Filho JS. Molecular subclasses of breast cancer: how do we define them? The IMPAKT 2012 Working Group Statement. *Ann Oncol* 2012; **23**: 2997-3006 [PMID: [23166150](https://pubmed.ncbi.nlm.nih.gov/23166150/) DOI: [10.1093/annonc/mds586](https://doi.org/10.1093/annonc/mds586)]
 - 33 **Giuliano AE**, Connolly JL, Edge SB, Mittendorf EA, Rugo HS, Solin LJ, Weaver DL, Winchester DJ, Hortobagyi GN. Breast Cancer-Major changes in the American Joint Committee on Cancer eighth edition cancer staging manual. *CA Cancer J Clin* 2017; **67**: 290-303 [PMID: [28294295](https://pubmed.ncbi.nlm.nih.gov/28294295/) DOI: [10.3322/caac.21393](https://doi.org/10.3322/caac.21393)]
 - 34 **Net JM**, Whitman GJ, Morris E, Brandt KR, Burnside ES, Giger ML, Ganott M, Sutton EJ, Zuley ML, Rao A. Relationships Between Human-Extracted MRI Tumor Phenotypes of Breast Cancer and Clinical Prognostic Indicators Including Receptor Status and Molecular Subtype. *Curr Probl Diagn Radiol* 2019; **48**: 467-472 [PMID: [30270031](https://pubmed.ncbi.nlm.nih.gov/30270031/) DOI: [10.1067/j.cpradiol.2018.08.003](https://doi.org/10.1067/j.cpradiol.2018.08.003)]
 - 35 **Jinguji M**, Kajiya Y, Kamimura K, Nakajo M, Sagara Y, Takahama T, Ando M, Rai Y, Sagara Y, Ohi Y, Yoshida H. Rim enhancement of breast cancers on contrast-enhanced MR imaging: relationship with prognostic factors. *Breast Cancer* 2006; **13**: 64-73 [PMID: [16518064](https://pubmed.ncbi.nlm.nih.gov/16518064/) DOI: [10.2325/jbcs.13.64](https://doi.org/10.2325/jbcs.13.64)]
 - 36 **Blaschke E**, Abe H. MRI phenotype of breast cancer: Kinetic assessment for molecular subtypes. *J Magn Reson Imaging* 2015; **42**: 920-924 [PMID: [25758675](https://pubmed.ncbi.nlm.nih.gov/25758675/) DOI: [10.1002/jmri.24884](https://doi.org/10.1002/jmri.24884)]
 - 37 **Grimm LJ**, Zhang J, Baker JA, Soo MS, Johnson KS, Mazurowski MA. Relationships Between MRI Breast Imaging-Reporting and Data System (BI-RADS) Lexicon Descriptors and Breast Cancer Molecular Subtypes: Internal Enhancement is Associated with Luminal B Subtype. *Breast J* 2017; **23**: 579-582 [PMID: [28295860](https://pubmed.ncbi.nlm.nih.gov/28295860/) DOI: [10.1111/tbj.12799](https://doi.org/10.1111/tbj.12799)]
 - 38 **Martincich L**, Deantoni V, Bertotto I, Redana S, Kubatzki F, Sarotto I, Rossi V, Liotti M, Ponzone R, Aglietta M, Regge D, Montemurro F. Correlations between diffusion-weighted imaging and breast cancer biomarkers. *Eur Radiol* 2012; **22**: 1519-1528 [PMID: [22411304](https://pubmed.ncbi.nlm.nih.gov/22411304/) DOI: [10.1007/s00330-012-2403-8](https://doi.org/10.1007/s00330-012-2403-8)]
 - 39 **Montemezzi S**, Camera L, Giri MG, Pozzetto A, Caliò A, Meliàdò G, Caumo F, Cavedon C. Is there a correlation between 3T multiparametric MRI and molecular subtypes of breast cancer? *Eur J Radiol* 2018; **108**: 120-127 [PMID: [30396643](https://pubmed.ncbi.nlm.nih.gov/30396643/) DOI: [10.1016/j.ejrad.2018.09.024](https://doi.org/10.1016/j.ejrad.2018.09.024)]
 - 40 **Shin HJ**, Baek HM, Cha JH, Kim HH. Evaluation of breast cancer using proton MR spectroscopy: total choline peak integral and signal-to-noise ratio as prognostic indicators. *AJR Am J Roentgenol* 2012; **198**: W488-W497 [PMID: [22528931](https://pubmed.ncbi.nlm.nih.gov/22528931/) DOI: [10.2214/AJR.11.7292](https://doi.org/10.2214/AJR.11.7292)]
 - 41 **Sah RG**, Sharma U, Parshad R, Seenu V, Mathur SR, Jagannathan NR. Association of estrogen receptor, progesterone receptor, and human epidermal growth factor receptor 2 status with total choline concentration and tumor volume in breast cancer patients: an MRI and in vivo proton MRS study. *Magn Reson Med* 2012; **68**: 1039-1047 [PMID: [22213087](https://pubmed.ncbi.nlm.nih.gov/22213087/) DOI: [10.1002/mrm.24117](https://doi.org/10.1002/mrm.24117)]
 - 42 **Sutton EJ**, Dashevsky BZ, Oh JH, Veeraraghavan H, Apte AP, Thakur SB, Morris EA, Deasy JO. Breast cancer molecular subtype classifier that incorporates MRI features. *J Magn Reson Imaging* 2016; **44**: 122-129 [PMID: [26756416](https://pubmed.ncbi.nlm.nih.gov/26756416/) DOI: [10.1002/jmri.25119](https://doi.org/10.1002/jmri.25119)]
 - 43 **Agner SC**, Rosen MA, Englander S, Tomaszewski JE, Feldman MD, Zhang P, Mies C, Schnall MD, Madabhushi A. Computerized image analysis for identifying triple-negative breast cancers and differentiating them from other molecular subtypes of breast cancer on dynamic contrast-enhanced MR images: a feasibility study. *Radiology* 2014; **272**: 91-99 [PMID: [24620909](https://pubmed.ncbi.nlm.nih.gov/24620909/) DOI: [10.1148/radiol.14121031](https://doi.org/10.1148/radiol.14121031)]
 - 44 **Fan M**, Yuan W, Zhao W, Xu M, Wang S, Gao X, Li L. Joint Prediction of Breast Cancer Histological Grade and Ki-67 Expression Level Based on DCE-MRI and DWI Radiomics. *IEEE J Biomed Health Inform* 2020; **24**: 1632-1642 [PMID: [31794406](https://pubmed.ncbi.nlm.nih.gov/31794406/) DOI: [10.1109/JBHI.2019.2956351](https://doi.org/10.1109/JBHI.2019.2956351)]
 - 45 **Wu J**, Sun X, Wang J, Cui Y, Kato F, Shirato H, Ikeda DM, Li R. Identifying relations between imaging phenotypes and molecular subtypes of breast cancer: Model discovery and external validation. *J Magn Reson Imaging* 2017; **46**: 1017-1027 [PMID: [28177554](https://pubmed.ncbi.nlm.nih.gov/28177554/) DOI: [10.1002/jmri.25661](https://doi.org/10.1002/jmri.25661)]
 - 46 **Li H**, Zhu Y, Burnside ES, Huang E, Drukker K, Hoadley KA, Fan C, Conzen SD, Zuley M, Net JM, Sutton E, Whitman GJ, Morris E, Perou CM, Ji Y, Giger ML. Quantitative MRI radiomics in the prediction of molecular classifications of breast cancer subtypes in the TCGA/TCIA data set. *NPJ Breast Cancer* 2016; **2**: 16012 [PMID: [27853751](https://pubmed.ncbi.nlm.nih.gov/27853751/) DOI: [10.1038/npjbcancer.2016.12](https://doi.org/10.1038/npjbcancer.2016.12)]
 - 47 **Chang RF**, Chen HH, Chang YC, Huang CS, Chen JH, Lo CM. Quantification of breast tumor heterogeneity for ER status, HER2 status, and TN molecular subtype evaluation on DCE-MRI. *Magn Reson Imaging* 2016; **34**: 809-819 [PMID: [26968141](https://pubmed.ncbi.nlm.nih.gov/26968141/) DOI: [10.1016/j.mri.2016.03.001](https://doi.org/10.1016/j.mri.2016.03.001)]
 - 48 **Fan M**, Li H, Wang S, Zheng B, Zhang J, Li L. Radiomic analysis reveals DCE-MRI features for prediction of molecular subtypes of breast cancer. *PLoS One* 2017; **12**: e0171683 [PMID: [28166261](https://pubmed.ncbi.nlm.nih.gov/28166261/) DOI: [10.1371/journal.pone.0171683](https://doi.org/10.1371/journal.pone.0171683)]
 - 49 **Wang J**, Kato F, Oyama-Manabe N, Li R, Cui Y, Tha KK, Yamashita H, Kudo K, Shirato H. Identifying Triple-Negative Breast Cancer Using Background Parenchymal Enhancement Heterogeneity on Dynamic Contrast-Enhanced MRI: A Pilot Radiomics Study. *PLoS One* 2015; **10**: e0143308 [PMID: [26600392](https://pubmed.ncbi.nlm.nih.gov/26600392/) DOI: [10.1371/journal.pone.0143308](https://doi.org/10.1371/journal.pone.0143308)]
 - 50 **Braman N**, Prasanna P, Whitney J, Singh S, Beig N, Etesami M, Bates DDB, Gallagher K, Bloch BN, Vulchi M, Turk P, Bera K, Abraham J, Sikov WM, Somlo G, Harris LN, Gilmore H, Plecha D, Varadan V, Madabhushi A. Association of Peritumoral Radiomics With Tumor Biology and Pathologic Response to

- Preoperative Targeted Therapy for HER2 (ERBB2)-Positive Breast Cancer. *JAMA Netw Open* 2019; **2**: e192561 [PMID: 31002322 DOI: 10.1001/jamanetworkopen.2019.2561]
- 51 **Leithner D**, Horvat JV, Marino MA, Bernard-Davila B, Jochelson MS, Ochoa-Albiztegui RE, Martinez DF, Morris EA, Thakur S, Pinker K. Radiomic signatures with contrast-enhanced magnetic resonance imaging for the assessment of breast cancer receptor status and molecular subtypes: initial results. *Breast Cancer Res* 2019; **21**: 106 [PMID: 31514736 DOI: 10.1186/s13058-019-1187-z]
- 52 **Holli-Helenius K**, Salminen A, Rinta-Kiikka I, Koskivuo I, Brück N, Boström P, Parkkola R. MRI texture analysis in differentiating luminal A and luminal B breast cancer molecular subtypes - a feasibility study. *BMC Med Imaging* 2017; **17**: 69 [PMID: 29284425 DOI: 10.1186/s12880-017-0239-z]
- 53 **Ma W**, Ji Y, Qi L, Guo X, Jian X, Liu P. Breast cancer Ki67 expression prediction by DCE-MRI radiomics features. *Clin Radiol* 2018; **73**: 909.e1-909.e5 [PMID: 29970244 DOI: 10.1016/j.crad.2018.05.027]
- 54 **Juan MW**, Yu J, Peng GX, Jun LJ, Feng SP, Fang LP. Correlation between DCE-MRI radiomics features and Ki-67 expression in invasive breast cancer. *Oncol Lett* 2018; **16**: 5084-5090 [PMID: 30250576 DOI: 10.3892/ol.2018.9271]
- 55 **Liang C**, Cheng Z, Huang Y, He L, Chen X, Ma Z, Huang X, Liang C, Liu Z. An MRI-based Radiomics Classifier for Preoperative Prediction of Ki-67 Status in Breast Cancer. *Acad Radiol* 2018; **25**: 1111-1117 [PMID: 29428211 DOI: 10.1016/j.acra.2018.01.006]
- 56 **Zhang Y**, Zhu Y, Zhang K, Liu Y, Cui J, Tao J, Wang Y, Wang S. Invasive ductal breast cancer: preoperative predict Ki-67 index based on radiomics of ADC maps. *Radiol Med* 2020; **125**: 109-116 [PMID: 31696388 DOI: 10.1007/s11547-019-01100-1]
- 57 **Tan H**, Gan F, Wu Y, Zhou J, Tian J, Lin Y, Wang M. Preoperative Prediction of Axillary Lymph Node Metastasis in Breast Carcinoma Using Radiomics Features Based on the Fat-Suppressed T2 Sequence. *Acad Radiol* 2019 [PMID: 31879160 DOI: 10.1016/j.acra.2019.11.004]
- 58 **Dong Y**, Feng Q, Yang W, Lu Z, Deng C, Zhang L, Lian Z, Liu J, Luo X, Pei S, Mo X, Huang W, Liang C, Zhang B, Zhang S. Preoperative prediction of sentinel lymph node metastasis in breast cancer based on radiomics of T2-weighted fat-suppression and diffusion-weighted MRI. *Eur Radiol* 2018; **28**: 582-591 [PMID: 28828635 DOI: 10.1007/s00330-017-5005-7]
- 59 **Liu C**, Ding J, Spuhler K, Gao Y, Serrano Sosa M, Moriarty M, Hussain S, He X, Liang C, Huang C. Preoperative prediction of sentinel lymph node metastasis in breast cancer by radiomic signatures from dynamic contrast-enhanced MRI. *J Magn Reson Imaging* 2019; **49**: 131-140 [PMID: 30171822 DOI: 10.1002/jmri.26224]
- 60 **Liu Z**, Feng B, Li C, Chen Y, Chen Q, Li X, Guan J, Chen X, Cui E, Li R, Li Z, Long W. Preoperative prediction of lymphovascular invasion in invasive breast cancer with dynamic contrast-enhanced-MRI-based radiomics. *J Magn Reson Imaging* 2019; **50**: 847-857 [PMID: 30773770 DOI: 10.1002/jmri.26688]
- 61 **Liu J**, Sun D, Chen L, Fang Z, Song W, Guo D, Ni T, Liu C, Feng L, Xia Y, Zhang X, Li C. Radiomics Analysis of Dynamic Contrast-Enhanced Magnetic Resonance Imaging for the Prediction of Sentinel Lymph Node Metastasis in Breast Cancer. *Front Oncol* 2019; **9**: 980 [PMID: 31632912 DOI: 10.3389/fonc.2019.00980]
- 62 **Han L**, Zhu Y, Liu Z, Yu T, He C, Jiang W, Kan Y, Dong D, Tian J, Luo Y. Radiomic nomogram for prediction of axillary lymph node metastasis in breast cancer. *Eur Radiol* 2019; **29**: 3820-3829 [PMID: 30701328 DOI: 10.1007/s00330-018-5981-2]
- 63 **Cui X**, Wang N, Zhao Y, Chen S, Li S, Xu M, Chai R. Preoperative Prediction of Axillary Lymph Node Metastasis in Breast Cancer using Radiomics Features of DCE-MRI. *Sci Rep* 2019; **9**: 2240 [PMID: 30783148 DOI: 10.1038/s41598-019-38502-0]
- 64 **Burnside ES**, Drukker K, Li H, Bonaccio E, Zuley M, Ganott M, Net JM, Sutton EJ, Brandt KR, Whitman GJ, Conzen SD, Lan L, Ji Y, Zhu Y, Jaffe CC, Huang EP, Freymann JB, Kirby JS, Morris EA, Giger ML. Using computer-extracted image phenotypes from tumors on breast magnetic resonance imaging to predict breast cancer pathologic stage. *Cancer* 2016; **122**: 748-757 [PMID: 26619259 DOI: 10.1002/ncr.29791]
- 65 **Reig B**, Heacock L, Geras KJ, Moy L. Machine learning in breast MRI. *J Magn Reson Imaging* 2019 [PMID: 31276247 DOI: 10.1002/jmri.26852]
- 66 **Schacht DV**, Drukker K, Pak I, Abe H, Giger ML. Using quantitative image analysis to classify axillary lymph nodes on breast MRI: a new application for the Z 0011 Era. *Eur J Radiol* 2015; **84**: 392-397 [PMID: 25547328 DOI: 10.1016/j.ejrad.2014.12.003]
- 67 **Fusco R**, Sansone M, Granata V, Di Bonito M, Avino F, Catalano O, Botti G, Petrillo A. Use of Quantitative Morphological and Functional Features for Assessment of Axillary Lymph Node in Breast Dynamic Contrast-Enhanced Magnetic Resonance Imaging. *Biomed Res Int* 2018; **2018**: 2610801 [PMID: 30003092 DOI: 10.1155/2018/2610801]
- 68 **Thompson AM**, Moulder-Thompson SL. Neoadjuvant treatment of breast cancer. *Ann Oncol* 2012; **23** Suppl 10: x231-x236 [PMID: 22987968 DOI: 10.1093/annonc/nds324]
- 69 **Haque W**, Verma V, Hatch S, Suzanne Klimberg V, Brian Butler E, Teh BS. Response rates and pathologic complete response by breast cancer molecular subtype following neoadjuvant chemotherapy. *Breast Cancer Res Treat* 2018; **170**: 559-567 [PMID: 29693228 DOI: 10.1007/s10549-018-4801-3]
- 70 **Yuan Y**, Chen XS, Liu SY, Shen KW. Accuracy of MRI in prediction of pathologic complete remission in breast cancer after preoperative therapy: a meta-analysis. *AJR Am J Roentgenol* 2010; **195**: 260-268 [PMID: 20566826 DOI: 10.2214/AJR.09.3908]
- 71 **Marinovich ML**, Houssami N, Macaskill P, Sardanelli F, Irwig L, Mamounas EP, von Minckwitz G, Brennan ME, Ciatto S. Meta-analysis of magnetic resonance imaging in detecting residual breast cancer after neoadjuvant therapy. *J Natl Cancer Inst* 2013; **105**: 321-333 [PMID: 23297042 DOI: 10.1093/jnci/djs528]
- 72 **Hylton NM**, Blume JD, Bernreuter WK, Pisano ED, Rosen MA, Morris EA, Weatherall PT, Lehman CD, Newstead GM, Polin S, Marques HS, Esserman LJ, Schnall MD; ACRIN 6657 Trial Team and I-SPY 1 TRIAL Investigators. Locally advanced breast cancer: MR imaging for prediction of response to neoadjuvant chemotherapy--results from ACRIN 6657/I-SPY TRIAL. *Radiology* 2012; **263**: 663-672 [PMID: 22623692 DOI: 10.1148/radiol.12110748]

- 73 **Yu N**, Leung VWY, Meterissian S. MRI Performance in Detecting pCR After Neoadjuvant Chemotherapy by Molecular Subtype of Breast Cancer. *World J Surg* 2019; **43**: 2254-2261 [PMID: [31101952](#) DOI: [10.1007/s00268-019-05032-9](#)]
- 74 **Michoux N**, Van den Broeck S, Lacoste L, Fellah L, Galant C, Berlière M, Leconte I. Texture analysis on MR images helps predicting non-response to NAC in breast cancer. *BMC Cancer* 2015; **15**: 574 [PMID: [26243303](#) DOI: [10.1186/s12885-015-1563-8](#)]
- 75 **Wiechmann L**, Sampson M, Stempel M, Jacks LM, Patil SM, King T, Morrow M. Presenting features of breast cancer differ by molecular subtype. *Ann Surg Oncol* 2009; **16**: 2705-2710 [PMID: [19593632](#) DOI: [10.1245/s10434-009-0606-2](#)]
- 76 **Xiong Q**, Zhou X, Liu Z, Lei C, Yang C, Yang M, Zhang L, Zhu T, Zhuang X, Liang C, Liu Z, Tian J, Wang K. Multiparametric MRI-based radiomics analysis for prediction of breast cancers insensitive to neoadjuvant chemotherapy. *Clin Transl Oncol* 2020; **22**: 50-59 [PMID: [30977048](#) DOI: [10.1007/s12094-019-02109-8](#)]
- 77 **Cain EH**, Saha A, Harowicz MR, Marks JR, Marcom PK, Mazurowski MA. Multivariate machine learning models for prediction of pathologic response to neoadjuvant therapy in breast cancer using MRI features: a study using an independent validation set. *Breast Cancer Res Treat* 2019; **173**: 455-463 [PMID: [30328048](#) DOI: [10.1007/s10549-018-4990-9](#)]
- 78 **Granzier RWY**, van Nijnatten TJA, Woodruff HC, Smidt ML, Lobbes MBI. Exploring breast cancer response prediction to neoadjuvant systemic therapy using MRI-based radiomics: A systematic review. *Eur J Radiol* 2019; **121**: 108736 [PMID: [31734639](#) DOI: [10.1016/j.ejrad.2019.108736](#)]
- 79 **Golden DI**, Lipson JA, Telli ML, Ford JM, Rubin DL. Dynamic contrast-enhanced MRI-based biomarkers of therapeutic response in triple-negative breast cancer. *J Am Med Assoc* 2013; **20**: 1059-1066 [PMID: [23785100](#) DOI: [10.1136/amiajnl-2012-001460](#)]
- 80 **Teruel JR**, Heldahl MG, Goa PE, Pickles M, Lundgren S, Bathen TF, Gibbs P. Dynamic contrast-enhanced MRI texture analysis for pretreatment prediction of clinical and pathological response to neoadjuvant chemotherapy in patients with locally advanced breast cancer. *NMR Biomed* 2014; **27**: 887-896 [PMID: [24840393](#) DOI: [10.1002/nbm.3132](#)]
- 81 **Thibault G**, Tudorica A, Afzal A, Chui SY, Naik A, Troxell ML, Kemmer KA, Oh KY, Roy N, Jafarian N, Holtorf ML, Huang W, Song X. DCE-MRI Texture Features for Early Prediction of Breast Cancer Therapy Response. *Tomography* 2017; **3**: 23-32 [PMID: [28691102](#) DOI: [10.18383/j.tom.2016.00241](#)]
- 82 **Parikh J**, Selmi M, Charles-Edwards G, Glendenning J, Ganeshan B, Verma H, Mansi J, Harries M, Tutt A, Goh V. Changes in primary breast cancer heterogeneity may augment midtreatment MR imaging assessment of response to neoadjuvant chemotherapy. *Radiology* 2014; **272**: 100-112 [PMID: [24654970](#) DOI: [10.1148/radiol.14130569](#)]
- 83 **Cao K**, Zhao B, Li XT, Li YL, Sun YS. Texture Analysis of Dynamic Contrast-Enhanced MRI in Evaluating Pathologic Complete Response (pCR) of Mass-Like Breast Cancer after Neoadjuvant Therapy. *J Oncol* 2019; **2019**: 4731532 [PMID: [31949430](#) DOI: [10.1155/2019/4731532](#)]
- 84 **Wu J**, Cao G, Sun X, Lee J, Rubin DL, Napel S, Kurian AW, Daniel BL, Li R. Intratumoral Spatial Heterogeneity at Perfusion MR Imaging Predicts Recurrence-free Survival in Locally Advanced Breast Cancer Treated with Neoadjuvant Chemotherapy. *Radiology* 2018; **288**: 26-35 [PMID: [29714680](#) DOI: [10.1148/radiol.2018172462](#)]
- 85 **Fusco R**, Granata V, Maio F, Sansone M, Petrillo A. Textural radiomic features and time-intensity curve data analysis by dynamic contrast-enhanced MRI for early prediction of breast cancer therapy response: preliminary data. *Eur Radiol Exp* 2020; **4**: 8 [PMID: [32026095](#) DOI: [10.1186/s41747-019-0141-2](#)]
- 86 **Mohammed ZM**, McMillan DC, Edwards J, Mallon E, Doughty JC, Orange C, Going JJ. The relationship between lymphovascular invasion and angiogenesis, hormone receptors, cell proliferation and survival in patients with primary operable invasive ductal breast cancer. *BMC Clin Pathol* 2013; **13**: 31 [PMID: [24274633](#) DOI: [10.1186/1472-6890-13-31](#)]
- 87 **Braman NM**, Etesami M, Prasanna P, Dubchuk C, Gilmore H, Tiwari P, Plecha D, Madabhushi A. Intratumoral and peritumoral radiomics for the pretreatment prediction of pathological complete response to neoadjuvant chemotherapy based on breast DCE-MRI. *Breast Cancer Res* 2017; **19**: 57 [PMID: [28521821](#) DOI: [10.1186/s13058-017-0846-1](#)]
- 88 **Zhou J**, Lu J, Gao C, Zeng J, Zhou C, Lai X, Cai W, Xu M. Predicting the response to neoadjuvant chemotherapy for breast cancer: wavelet transforming radiomics in MRI. *BMC Cancer* 2020; **20**: 100 [PMID: [32024483](#) DOI: [10.1186/s12885-020-6523-2](#)]
- 89 **Liu Z**, Li Z, Qu J, Zhang R, Zhou X, Li L, Sun K, Tang Z, Jiang H, Li H, Xiong Q, Ding Y, Zhao X, Wang K, Liu Z, Tian J. Radiomics of Multiparametric MRI for Pretreatment Prediction of Pathologic Complete Response to Neoadjuvant Chemotherapy in Breast Cancer: A Multicenter Study. *Clin Cancer Res* 2019; **25**: 3538-3547 [PMID: [30842125](#) DOI: [10.1158/1078-0432.CCR-18-3190](#)]
- 90 **Chen X**, Chen X, Yang J, Li Y, Fan W, Yang Z. Combining Dynamic Contrast-Enhanced Magnetic Resonance Imaging and Apparent Diffusion Coefficient Maps for a Radiomics Nomogram to Predict Pathological Complete Response to Neoadjuvant Chemotherapy in Breast Cancer Patients. *J Comput Assist Tomogr* 2020; **44**: 275-283 [PMID: [32004189](#) DOI: [10.1097/RCT.0000000000000978](#)]
- 91 **Hyun SJ**, Kim EK, Moon HJ, Yoon JH, Kim MJ. Preoperative axillary lymph node evaluation in breast cancer patients by breast magnetic resonance imaging (MRI): Can breast MRI exclude advanced nodal disease? *Eur Radiol* 2016; **26**: 3865-3873 [PMID: [26843011](#) DOI: [10.1007/s00330-016-4235-4](#)]
- 92 **Mattingly AE**, Mooney B, Lin HY, Kiluk JV, Khakpour N, Hoover SJ, Laronga C, Lee MC. Magnetic Resonance Imaging for Axillary Breast Cancer Metastasis in the Neoadjuvant Setting: A Prospective Study. *Clin Breast Cancer* 2017; **17**: 180-187 [PMID: [27956116](#) DOI: [10.1016/j.clbc.2016.11.004](#)]
- 93 **Ha SM**, Cha JH, Kim HH, Shin HJ, Chae EY, Choi WJ. Diagnostic performance of breast ultrasonography and MRI in the prediction of lymph node status after neoadjuvant chemotherapy for breast cancer. *Acta Radiol* 2017; **58**: 1198-1205 [PMID: [28350255](#) DOI: [10.1177/0284185117690421](#)]
- 94 **Ha R**, Chang P, Karcich J, Mutasa S, Fardanesh R, Wynn RT, Liu MZ, Jambawalikar S. Axillary Lymph Node Evaluation Utilizing Convolutional Neural Networks Using MRI Dataset. *J Digit Imaging* 2018; **31**:

- 851-856 [PMID: 29696472 DOI: 10.1007/s10278-018-0086-7]
- 95 **Ha R**, Chin C, Karcich J, Liu MZ, Chang P, Mutasa S, Pascual Van Sant E, Wynn RT, Connolly E, Jambawalikar S. Prior to Initiation of Chemotherapy, Can We Predict Breast Tumor Response? Deep Learning Convolutional Neural Networks Approach Using a Breast MRI Tumor Dataset. *J Digit Imaging* 2019; **32**: 693-701 [PMID: 30361936 DOI: 10.1007/s10278-018-0144-1]
- 96 **Ha R**, Chang P, Karcich J, Mutasa S, Van Sant EP, Connolly E, Chin C, Taback B, Liu MZ, Jambawalikar S. Predicting Post Neoadjuvant Axillary Response Using a Novel Convolutional Neural Network Algorithm. *Ann Surg Oncol* 2018; **25**: 3037-3043 [PMID: 29978368 DOI: 10.1245/s10434-018-6613-4]
- 97 **Ashraf AB**, Daye D, Gavenonis S, Mies C, Feldman M, Rosen M, Kontos D. Identification of intrinsic imaging phenotypes for breast cancer tumors: preliminary associations with gene expression profiles. *Radiology* 2014; **272**: 374-384 [PMID: 24702725 DOI: 10.1148/radiol.14131375]
- 98 **Ganeshan B**, Panayiotou E, Burnand K, Dizdarevic S, Miles K. Tumour heterogeneity in non-small cell lung carcinoma assessed by CT texture analysis: a potential marker of survival. *Eur Radiol* 2012; **22**: 796-802 [PMID: 22086561 DOI: 10.1007/s00330-011-2319-8]
- 99 **Li H**, Zhu Y, Burnside ES, Drukker K, Hoadley KA, Fan C, Conzen SD, Whitman GJ, Sutton EJ, Net JM, Ganott M, Huang E, Morris EA, Perou CM, Ji Y, Giger ML. MR Imaging Radiomics Signatures for Predicting the Risk of Breast Cancer Recurrence as Given by Research Versions of MammaPrint, Oncotype DX, and PAM50 Gene Assays. *Radiology* 2016; **281**: 382-391 [PMID: 27144536 DOI: 10.1148/radiol.2016152110]
- 100 **Ha R**, Chang P, Mutasa S, Karcich J, Goodman S, Blum E, Kalinsky K, Liu MZ, Jambawalikar S. Convolutional Neural Network Using a Breast MRI Tumor Dataset Can Predict Oncotype Dx Recurrence Score. *J Magn Reson Imaging* 2019; **49**: 518-524 [PMID: 30129697 DOI: 10.1002/jmri.26244]
- 101 **Harris LN**, Ismaila N, McShane LM, Andre F, Collyar DE, Gonzalez-Angulo AM, Hammond EH, Kuderer NM, Liu MC, Mennel RG, Van Poznak C, Bast RC, Hayes DF; American Society of Clinical Oncology. Use of Biomarkers to Guide Decisions on Adjuvant Systemic Therapy for Women With Early-Stage Invasive Breast Cancer: American Society of Clinical Oncology Clinical Practice Guideline. *J Clin Oncol* 2016; **34**: 1134-1150 [PMID: 26858339 DOI: 10.1200/JCO.2015.65.2289]
- 102 **Saha A**, Harowicz MR, Wang W, Mazurowski MA. A study of association of Oncotype DX recurrence score with DCE-MRI characteristics using multivariate machine learning models. *J Cancer Res Clin Oncol* 2018; **144**: 799-807 [PMID: 29427210 DOI: 10.1007/s00432-018-2595-7]
- 103 **Park H**, Lim Y, Ko ES, Cho HH, Lee JE, Han BK, Ko EY, Choi JS, Park KW. Radiomics Signature on Magnetic Resonance Imaging: Association with Disease-Free Survival in Patients with Invasive Breast Cancer. *Clin Cancer Res* 2018; **24**: 4705-4714 [PMID: 29914892 DOI: 10.1158/1078-0432.CCR-17-3783]
- 104 **Koh J**, Lee E, Han K, Kim S, Kim DK, Kwak JY, Yoon JH, Moon HJ. Three-dimensional radiomics of triple-negative breast cancer: Prediction of systemic recurrence. *Sci Rep* 2020; **10**: 2976 [PMID: 32076078 DOI: 10.1038/s41598-020-59923-2]
- 105 **Kim S**, Kim MJ, Kim EK, Yoon JH, Park VY. MRI Radiomic Features: Association with Disease-Free Survival in Patients with Triple-Negative Breast Cancer. *Sci Rep* 2020; **10**: 3750 [PMID: 32111957 DOI: 10.1038/s41598-020-60822-9]



Artificial intelligence in pancreatic disease

Bang-Bin Chen

ORCID number: Bang-Bin Chen
0000-0001-7058-1427.

Author contributions: Chen BB wrote and revised the manuscript.

Supported by grants from the Ministry of Science and Technology (Taiwan), No. 104-2314-B-002-080-MY3 and No. 107-2314-B-002-102-MY3.

Conflict-of-interest statement: No conflict of interest.

Open-Access: This article is an open-access article that was selected by an in-house editor and fully peer-reviewed by external reviewers. It is distributed in accordance with the Creative Commons Attribution NonCommercial (CC BY-NC 4.0) license, which permits others to distribute, remix, adapt, build upon this work non-commercially, and license their derivative works on different terms, provided the original work is properly cited and the use is non-commercial. See: <http://creativecommons.org/licenses/by-nc/4.0/>

Manuscript source: Invited manuscript

Received: June 9, 2020

Peer-review started: June 9, 2020

First decision: June 15, 2020

Revised: June 18, 2020

Accepted: June 20, 2020

Article in press: June 20, 2020

Bang-Bin Chen, Department of Medical Imaging, National Taiwan University Hospital, Taipei 10016, Taiwan

Bang-Bin Chen, Department of Radiology, College of Medicine, National Taiwan University, Taipei 10016, Taiwan

Corresponding author: Bang-Bin Chen, MD, Associate Professor, Department of Medical Imaging, National Taiwan University College of Medicine and Hospital, No. 7, Chung-Shan South Road, Taipei 10016, Taiwan. bangbin@gmail.com

Abstract

In recent years, the application of artificial intelligence (AI) in radiology has been growing rapidly, fueled by the availability of large datasets, advances in computing power, and newly developed algorithms. Progress in AI applied to medical imaging analyses has transformed these images into quantitative data, termed radiomics. When combined with patients' clinical data, these models, when developed by machine learning, have the potential to improve diagnostic, prognostic, and predictive accuracy. Currently, limited literature is available on the use of radiomics for pancreatic disease. Here, we will review recent studies in the application of AI in a variety of pancreatic diseases, mainly involving lesion detection, tumor characterization, tumor grading, response, and prognosis evaluation. Finally, we will also discuss the challenges and prospects in the field of radiomics for pancreatic disease.

Key words: Artificial intelligence; Machine learning; Deep learning; Radiomics; Texture analysis, Pancreas

©The Author(s) 2020. Published by Baishideng Publishing Group Inc. All rights reserved.

Core tip: The integration of radiomics, clinical data, and advanced machine-learning methodologies will improve diagnostic, prognostic, and predictive accuracy in patients with pancreatic disease, and facilitate clinical decision and management towards precision medicine.

Citation: Chen BB. Artificial intelligence in pancreatic disease. *Artif Intell Med Imaging* 2020; 1(1): 19-30

URL: <https://www.wjnet.com/2644-3260/full/v1/i1/19.htm>

DOI: <https://dx.doi.org/10.35711/aimi.v1.i1.19>

Published online: June 28, 2020

P-Reviewer: Cimen SG

S-Editor: Wang JL

L-Editor: A

E-Editor: Xing YX



INTRODUCTION

Artificial intelligence (AI) describes the use of computers to simulate performance and critical thinking equivalent to a human being. Its application in radiology has been growing rapidly, powered by the availability of large datasets, advances in computing power, and newly developed algorithms^[1]. The progress in AI of medical imaging analyses has converted these images into quantitative and minable data to facilitate better clinical decisions and management^[2,3]. This comprehensive method, when used to analyze high-dimensional quantitative features from multimodality medical images, is known as radiomics^[4].

To establish robust quantitative image analyses, standardized methodologies are required based on various image modalities, such as those of computed tomography (CT), magnetic resonance imaging (MRI), and positron emission tomography (PET), especially for texture- and filter-based features^[5,6]. After the mining of correlations between these features and diagnosis/prognosis of tumors, tumors can then be decoded into different imaging phenotypes^[7]. These data are then combined with other patients' data to develop models that can potentially enhance diagnostic, prognostic, and predictive accuracy^[8]. Because these analyses are based on the standard of care images, it is imaginable that radiomics analysis will eventually become routine practice^[9,10].

There are three approaches to data-mining for radiomics, including hand-crafted features, deep features, and a hybrid method. Traditional radiomics is done with the computation of agnostic hand-crafted features, which are computed automatically by image analysis algorithms^[5]. For instance, texture analysis has been widely used to quantify intuitive qualities by measuring the spatial variation in pixel intensities on images. In contrast to traditional radiomics, deep-learning extracts deep features from medical images based on the specifications of a pre-defined task, including disease diagnostics, cancer type prediction, or survival prediction. These deep features can be obtained via various architectures, such as a convolutional neural network (CNN), to find the most relevant features related to a pre-defined task^[11]. Thus, they can automatically learn the best features for a given task, without the need for human involvement for feature design. Recent studies have shown better performance by deep learning methods over traditional radiomics^[12,13]. Besides, the hybrid method, which combines hand-crafted and deep features, could provide complementary information for the radiological evaluation in cancer patients^[14-16].

The currently available literature on the use of radiomics for pancreatic disease is limited. Here, we will review recent studies in the application of texture analysis and radiomics in pancreatic malignancy, mainly involving cancer detection, grading, response, and prognosis evaluation. We will also review the performance of radiomics in differentiating between pancreatic cancer and other benign pancreatic lesions, such as autoimmune pancreatitis (AIP) and mass-forming pancreatitis (MFP). Finally, we will discuss the challenges and prospects in the field of radiomics for pancreatic disease. A summary table (Table 1) is also presented based on our review of the recent literature.

PANCREATIC DUCTAL ADENOCARCINOMA

Pancreatic ductal adenocarcinoma (PDAC) is the third leading cause of cancer-related deaths in the USA. The 5-year survival for PDAC is only 8%, due to its aggressive nature and late-stage presentation when discovered in most patients^[17]. Therefore, early detection of PDAC is critical, because surgical resection is the only method to cure this disease. In patients receiving a surgical intervention, the involvement of regional lymph nodes and residual tumor at the surgical margin are also important issues related to survival outcome. In patients with metastatic disease receiving chemotherapy or radiotherapy, the use of radiomics to predict treatment response is being investigated.

Early detection of pancreatic ductal adenocarcinoma

Radiomics might offer an advantage over other techniques in the early detection of PDAC. This is because the subtle difference of the texture patterns between early cancer and normal pancreas might be discernable using radiomic features prior to visual detection.

Chu *et al*^[18] used 3D CT radiomic features to differentiate PDAC and normal pancreas by manually segmented features of the pancreas. The dataset included 190

Table 1 Recent publications using artificial intelligence and radiomics in pancreatic disease

Ref.	Year	Disease	Number	Training/testing	Modality	Design	Feature selection	Results
PADC detection								
Chu <i>et al</i> ^[18]	2019	PDAC vs normal	190:190	255/125	CT	Retrospective	RF	Accuracy: 99.2%; AUC: 0.99
Liu <i>et al</i> ^[19]	2020	PDAC vs normal	370:320	PDAC: 295/256; Normal: 75/64	CT	Retrospective	CNN	Accuracy: 98.6-98.9%; AUC: 0.997-0.999
Li <i>et al</i> ^[21]	2020	LN metastasis	159	118/41	CT	Retrospective	LASSO	Combined model; AUC: Training/test = 0.944/0.912
Bian <i>et al</i> ^[22]	2019	LN metastasis	225	-	CT	Retrospective	LASSO	The arterial rad-score is associated with the risk of LN metastasis.
Hui <i>et al</i> ^[25]	2020	R0 vs R1 after PD	34:52	-	CT	Retrospective	SVM	AUC: 0.8614 Accuracy: 84.88%
Bian <i>et al</i> ^[26]	2020	SMV margin (R0 vs R1) after PD	127:54	-	CT	Retrospective	LASSO	AUC: 0.75
Zhang <i>et al</i> ^[28]	2018	POPF after PD	117	80/37	CT	Retrospective	LASSO	AUC: Training/test 0.8248/0.7609
Xie <i>et al</i> ^[32]	2020	PFS and OS	220	147/73	CT	Retrospective	LASSO	Rad-score is better than clinical model and TNM system
Cozzi <i>et al</i> ^[33]	2019	OS and local control after SBRT	100	60/40	CT	Retrospective	Elastic net regularization, Cox regression models	Identify low and high-risk groups
IPMN								
Chakraborty <i>et al</i> ^[41]	2018	Low risk vs high risk	103	-	CT	Retrospective	RF, SVM	AUC: 0.77
Corral <i>et al</i> ^[42]	2019	Normal pancreas, low-grade dysplasia, high-grade dysplasia, and adenocarcinoma	139 (31:48:20:40)	-	MRI	Retrospective	Deep learning	AUC: 0.78
PNET								
Liang <i>et al</i> ^[49]	2019	Grade 1 vs 2/3	137	86/51	CT	Retrospective	LASSO	AUC: Training/test = 0.907/0.891
Gu <i>et al</i> ^[50]	2019	Grade 1 vs 2/3	138	104/34	CT	Retrospective	MRMR, RF	AUC: Training/test = 0.974/0.902
Bian <i>et al</i> ^[51]	2020	Grade 1 vs 2/3 (non-functional)	139	97/42	MRI	Retrospective	LASSO and LDA	AUC: Training/test = 0.851/0.736
Other pancreatic lesions								
Park <i>et al</i> ^[54]	2020	AIP vs PDAC	85: 93	60/29: 60/33	CT	Retrospective	RF	Accuracy: 95.2%; AUC: 0.975
Zhang <i>et al</i> ^[55]	2019	AIP vs PDAC	45: 66	-	PET/CT	Retrospective	RF, adaptive boosting, SVM	Accuracy: 85%; AUC: 0.93
Ren <i>et al</i> ^[56]	2019	MFP vs PDAC	79: 30	69/40	CT	Retrospective	Mann-Whitney U test, MRMR	AUC: 0.98

Mashayekhi <i>et al</i> ^[57]	2020	Functional abdominal pain, recurrent acute pancreatitis, chronic pancreatitis	20:19:17	-	CT	Retrospective	Isomap and SVM	Accuracy: 82.1%
Yang <i>et al</i> ^[58]	2019	Serous <i>vs</i> mucinous cystadenoma	53: 25	4:1	CT	Retrospective	RF	Accuracy: 83%; AUC: 0.75

AIP: Autoimmune pancreatitis; AUC: Area under receiver operating characteristic curve; CNN: Convolutional neural network; DFS: Disease-free survival; IPMN: Intraductal papillary mucinous neoplasms; LASSO: Least absolute shrinkage and selection operator; LDA: Linear discriminative analysis; LN: Lymph node; MFP: Mass-forming pancreatitis; MRMR: Minimum redundancy maximum relevance; OS: Overall survival; PD: Pancreaticoduodenectomy; PDAC: Pancreatic ductal adenocarcinoma; PET: Positron emission tomography; PFS: Progression-free survival; PNET: Pancreatic neuroendocrine tumor; POPF: Postoperative pancreatic fistula; RF: Random forest; SBRT: Stereotactic body radiation therapy; SVM: Support vector machine; SMV: Superior mesenteric vein.

patients with PDAC and 190 healthy controls, and was divided into 255 training and 125 validation cases. A total of 478 features was extracted, and 40 features were selected for analysis by a random forest (RF) classifier. The overall accuracy was 99.2%, and the area under the curve (AUC) was 99.9%. The results were encouraging for using radiomics in the early detection of PDAC, but a limitation of this study was that the manual segmentation of pancreas boundaries was a labor-intensive work and required expert knowledge of radiologists.

To overcome this limitation, Liu *et al*^[19] used CNN to distinguish 370 patients with pancreatic cancer and 320 normal controls. CT images were preprocessed into patches to classify as cancerous or non-cancerous. In local test sets, CNN-based analysis had an accuracy of 0.986–0.989 and AUC of 0.997–0.999. In the test set (281 pancreatic cancers and 82 controls) of a different country, the accuracy was 0.832 and AUC was 0.920. The sensitivity for tumors smaller than 2 cm was 92.1% in the local test sets and 63.1% in the other country test set. When compared with radiologists' interpretation, CNN-based analysis achieved higher sensitivity than radiologists. Therefore, this method could be incorporated into the development of computer-aided detection software for pancreatic cancer detection. In clinical practice, other benign lesions, such as MFP or AIP, might mimic PDAC. Whether CNNs can distinguish between PDAC and other pancreatic pathologies, such as pancreatitis and other pancreatic tumors, must also be further studied. Besides, about 11%–27% of pancreatic cancer is enhancing the pancreatic parenchyma and not visible on contrast-enhanced CT^[20]. It is interesting to see whether radiomics can detect this particular type of PDAC.

Predicting lymph node metastasis

Accurate identification of the extent of lymph node (LN) metastasis is critical for the determination of surgical methods in resectable PDAC.

Li *et al*^[21] developed a model integrating clinical data and imaging features extracted from venous phase CT to predict LN metastasis. Their study included 159 patients with PDAC (118 in the primary cohort and 41 in the validation cohort). A total of 2041 radiomics features were extracted, and 15 features were selected for constructing the radiomics signature in the primary cohort. A combined prediction model was built by integrating the radiomics signature and clinical characteristics selected by using multivariable logistic regression. The combined prediction model reached a better discrimination power than the clinical prediction model, with an AUC of 0.944 *vs* 0.666 in the primary cohort, and 0.912 *vs* 0.713 in the validation cohort.

Bian *et al*^[22] used arterial phase CT images to predict LN metastasis in 225 patients. A total of 1029 radiomics features of the arterial phase were extracted and then reduced using the least absolute shrinkage and selection operator logistic regression (LASSO) algorithm. Multivariate logistic regression models were used to analyze the association. The radiomics score (rad-score), which consisted of 12 selected features, was significantly associated with LN status, both in univariate and multivariate analyses. Higher arterial rad-score was also associated with LN metastasis. In the future, it is necessary to establish a one-to-one correlation between the imaging findings and the pathological evidence of LN metastasis.

Predicting surgical margin and postoperative pancreatic fistula after pancreaticoduodenectomy

In a pathological examination after pancreaticoduodenectomy (PD), a resection margin

without cancer cells in 1 mm is considered as R0; a resection margin with cancer cells in 1 mm is considered as R1. The preoperative identification of R0 and R1 is a determining factor for surgical decisions and prognosis^[23,24].

Hui *et al*^[25] retrospectively analyzed CT images of 86 patients (34 cases of R0 and 52 cases of R1) with pancreatic head PDAC and that underwent PD. The radiomics features were reduced using principal component analysis. The support vector machine (SVM) with a linear kernel was used to classify the resection margins with leave-one-out cross-validation. The results achieved an AUC of 0.8614 and an accuracy of 84.88%. Two features of the run-length matrix, which are derived from diagonal sub-bands in wavelet decomposition, showed significant differences between R0 and R1.

Similarly, Yun *et al*^[26] used a portal rad-score to predict pathologic superior mesenteric vein (SMV) resection margin in 181 patients. For each patient, 1029 radiomics features of the portal phase were extracted, which were reduced using the LASSO logistic regression algorithm. The rad-score was significantly associated with the SMV resection margin status. The portal rad-score had an accuracy of 71.3% and AUC of 0.750. Although radiomics seem promising in predicting SMV section margin, assessment of all pancreatic resection margins is needed to predict patients' outcomes. Furthermore, the radiomic features of mesopancreas (located between the superior mesenteric artery and the uncinate process) are more likely to predict the status of the section margin than those of a primary tumor, because it is regarded as the primary site of cancer cell infiltration^[27].

Zhang *et al*^[28] used radiomic features extracted from the portal venous phase CT for the preoperative prediction of postoperative pancreatic fistula (POPF) in 117 patients receiving PD. The rad-score was constructed by LASSO, and its performance was compared with standard pancreatic Fistula Risk Score. Their rad-score could predict POPF with an AUC of 0.8248 in the training cohort (80 patients) and of 0.7609 in the validation cohort (39 patients). In addition, the AUC of the rad-score was statistically higher than the Fistula Risk Score for predicting POPF in both cohorts.

Predicting therapy response

Many researchers have utilized radiomic features derived from pretreatment CT to identify imaging phenotypes that might predict the treatment response in patients with PDAC.

Chen *et al*^[29] assessed the response of pancreatic head cancer during chemoradiation therapy in 20 patients. They found that significant changes in CT radiomic features were observed during therapy based on quantitative analysis of daily CT. In cases of good response, patients tend to have large reductions in mean histograms of CT number and skewness, and large increases in standard deviation and kurtosis. Thus, a high reduction of these features might suggest early treatment response and could be used to identify patients that need therapeutic intensification.

Borazanci *et al*^[30] used texture analysis to predict treatment response to poly adenosine diphosphate-ribose polymerase (PARP) inhibitors. In 13 patients with PDAC who have deoxyribonucleic acid damage repair deficiency mutations, exploratory analysis of index lesions revealed correlations between lesion texture features with overall survival (OS), and also with time on PARP inhibitors.

Yue *et al*^[31] stratified patients into low and high-risk groups using pre- and post-radiotherapy 18F-FDG-PET/CT images from 26 patients. A total of 48 texture and clinical variables were identified, and the prognostic heterogeneity features were selected using LASSO/elastic net regression and multivariate Cox analysis. After radiotherapy, the metabolic activity in the primary tumor was suppressed, and underlying tissue heterogeneity was reduced. The authors identified five significant variables: Age, node stage, variations of homogeneity, variance, and cluster tendency. These patients could be stratified into two risk groups: A low-risk group ($n = 11$) with a longer mean OS and higher texture variation ($> 30\%$), and a high-risk group ($n = 15$) with a shorter mean OS and lower texture variation ($< 15\%$). The authors concluded that locoregional metabolic texture response might predict clinical outcomes following radiotherapy.

Predicting prognosis

Recent studies have suggested that radiomic features extracted from CT and PET were predictive of the survival outcome of PDAC patients.

Xie *et al*^[32] developed a CT-based radiomics nomogram for survival prediction in patients with resected PDAC in 220 patients (training = 147; validation = 73). A total of 300 radiomic features were extracted, followed by LASSO with multivariate regression analysis. The rad-score was significantly associated with disease-free survival (DFS)

and OS. Radiomics nomogram could better predict survival than the clinical model, and the TNM staging system could. However, there was no association between the rad-score and recurrence patterns.

Cozzi *et al*^[33] used CT radiomics signature to predict clinical outcomes after stereotactic body radiation therapy in 100 patients (training = 60; validation = 40) and found a clinical-radiomics signature was associated with OS and local control.

The value of texture features to predict prognosis and help clinical management in PDAC patients has been evaluated in several studies. In patients undergoing surgical resection, Kim *et al*^[34] found that high grey-level non-uniformity values suggested shorter recurrence-free survival in 116 patients, suggesting that high tumor heterogeneity was a poor prognostic indicator. However, Yun *et al*^[35] found that lower average values with homogeneous features (lower standard deviation and contrast and higher correlation) were significantly associated with poorer DFS in 18 patients. They conjectured that homogeneous texture features could represent more aggressive tumor nature, resulting from higher cellular density or dense desmoplasia. Besides, Eilaghi *et al*^[36] found that high tumor dissimilarity (high heterogeneity) and low inverse difference normalized (low heterogeneity) were associated with better OS in 30 patients. Therefore, the results of correlations between tumor heterogeneity with surgical outcome were contradictory and need further investigation.

In patients with unresectable PDAC treated with chemotherapy, Cheng *et al*^[37] found pretreatment CT texture analysis was associated with PFS and OS in 41 patients. Besides, a combination of pretreatment standard deviation (spatial scaling factor = 3) with tumor size in the survival model performed better than the standard deviation alone. Similarly, Sandrasegaran *et al*^[38] found that texture features of the mean value of positive pixels and kurtosis at medium spatial filters had a significant correlation with OS in 60 patients.

Hyun *et al*^[39] evaluated intratumoral heterogeneity measured by 18F-FDG PET texture analysis in 137 patients. The best imaging biomarker for OS prediction was first-order entropy (AUC = 0.720), followed by total lesion glycolysis (AUC = 0.697), metabolic tumor volume (AUC = 0.692), and maximum standard uptake value (AUC = 0.625). Multivariable Cox analysis demonstrated that higher entropy was independently associated with worse survival. Thus, first-order entropy is a better quantitative imaging biomarker of prognosis than conventional PET parameters.

INTRADUCTAL PAPILLARY MUCINOUS NEOPLASMS GRADE AND RISK

Intraductal papillary mucinous neoplasms (IPMN) represents 15%–30% of cystic lesions of the pancreas. They are premalignant tumors that can progress from low-grade dysplasia to high-grade dysplasia to invasive cancer, accounting for 20%–30% of pancreatic cancer^[40]. The ability to identify IPMNs with low or high risk and malignant transformation into invasive cancer would optimize treatment strategy and improve surgical decision-making.

Chakraborty *et al*^[41] retrospectively analyzed pancreatic cyst and parenchyma regions on preoperative CT in 103 patients with pathologically proven branch duct-IPMN to predict IPMN risk. Expert pathologists categorized IPMNs as low or high risk following resection. A total of 131 texture features were derived from each cyst and pancreas regions. Five clinical variables were combined with imaging features to design prediction models. Their results of CT features achieved an AUC of 0.77, and the combination model obtained an AUC of 0.81.

Corral *et al*^[42] developed a new deep learning protocol on MRI to identify neoplasia for IPMN in 139 cases. A computer-aided framework was designed using CNN to classify IPMN. Their cases included normal pancreas (20%), low-grade dysplasia (34%), high-grade dysplasia (14%), and adenocarcinoma (29%). The sensitivity and specificity of the deep learning protocol to detect dysplasia were 92% and 52%, and to detect high-grade dysplasia or cancer were 75% and 78%, respectively. The deep learning protocol showed accuracy (AUC = 0.78) comparable to current radiographic criteria (American Gastroenterology Association, AUC = 0.76; Fukuoka, AUC = 0.77). Their computer-aided frameworks could assist in identifying high-risk IPMN.

Hanania *et al*^[43] investigated 360 texture features on CT images in 53 patients with IPMN (34 high-grade and 19 low-grade). These authors identified 14 imaging features within the gray-level co-occurrence matrix that predicted histopathological grade. The most predictive feature differentiated low-grade and high-grade lesions with an AUC of 0.82 (sensitivity 85%, specificity 68%). Using a cross-validated design, the best logistic regression yielded an AUC of 0.96 (sensitivity 97%, specificity of 88%).

Permuth *et al*^[44] evaluated 38 IPMNs (20 benign, 18 malignant) with preoperative CT radiomic data and matched plasma-based miRNA genomic classifier data. The miRNA classifier, high-risk, and worrisome radiomic features had AUC values of 0.83, 0.84, and 0.54, respectively. Fourteen CT radiomic features differentiated malignant from benign IPMNs with an AUC of 0.77. Combining radiomic features with the miRNA classifier revealed an AUC of 0.92 and superior predictive performance than other models. This study suggested that radiogenomic approach might more accurately predict IPMN pathology than radiologic features in consensus guidelines.

PANCREATIC NEUROENDOCRINE TUMOR GRADES

Recent updates of the World Health Organization classification separate pancreatic neuroendocrine tumor (PNET) into two broad categories, including the Ki-67 proliferative index and mitotic counts: Well-differentiated PNET and poorly differentiated pancreatic neuroendocrine carcinoma (PNEC). The classification also incorporates a new subcategory of well-differentiated grade 3 (G3) PNET^[45]. The assessment of tumor grade is essential for the prediction of prognosis and choice of the proper treatment strategy.

D'Onofrio *et al*^[46] evaluated 3D CT-texture analysis in 100 patients with NET [grade 1 (G1) in 31, grade 2 (G2) in 52, and G3 in 17 cases]. Their results showed kurtosis was significantly different among the three groups, and entropy was significantly different between the G1 and G3 groups and between the G2 and G3 groups.

Guo *et al*^[47] evaluated CT images of 37 patients (G1 in 13, G2 in 11, and G3 in 13 cases). Arterial enhancement ratio and portal enhancement ratio showed the best sensitivity (0.86–0.94) and specificity (0.92–1.0) for differentiating G3 from G1/G2, while the mean grey-level intensity, entropy, and uniformity showed acceptable sensitivity (0.73–0.91) and specificity (0.85–1.0). Mean grey-level intensity also showed acceptable sensitivity (91% to 100%) and specificity (82% to 91%) in differentiating G1 from G2.

Canellas *et al*^[48] evaluated CT images of 101 patients (G1 in 63, G2 in 35, and G3 in 3 cases). The CT features predictive of G2/3 were size larger than 2.0 cm, presence of vascular involvement, pancreatic ductal dilatation, and lymphadenopathy. The texture parameter entropy was also predictive of more aggressive tumors. Tumors with high grade (G2/3), vascular invasion, and high entropy had shorter PFS after surgical resection.

Liang *et al*^[49] used arterial phase CT to preoperatively differentiate grade 1 and grade 2/3 NET of 137 patients (training = 86, validation = 51). The Mann-Whitney U test and LASSO were applied for feature selection, and an eight-feature-combined radiomics signature was constructed. The nomogram model combining the radiomics signature with the clinical stage had the best performance (training AUC = 0.907; validation AUC = 0.891). A significant correlation was found between the nomogram model and the Ki-67 index and the rate of nuclear mitosis. The survivals of predicted grade 1 and grade 2/3 groups were significantly different.

Gu *et al*^[50] used arterial and portal venous phase CT images for preoperatively predicting grade 1 and grade 2/3 NET in 138 patients (training = 104, validation = 34). A total of 853 radiomic features were extracted. Minimum redundancy, maximum relevance, and RF methods were adopted for the feature selection. The radiomics signature had a significant association with histologic grade. The nomogram incorporating independent clinical risk factor, tumor margin, and fusion radiomics signature showed strong discrimination in the training cohort (AUC = 0.974) and validation cohort (AUC = 0.902) with good calibration.

Bian *et al*^[51] used 3T MRI for the preoperative prediction of nonfunctional PNET grade in 139 cases (training = 97, validation = 42). The LASSO and linear discriminative analysis were used to select the features and to construct a radiomics model. The clinical model revealed an AUC of 0.769 in the training cohort and 0.729 in the validation cohort. The mixed model, which combined the radiomics signature and 14 imaging features, yielded AUC values of 0.870 and 0.701. Thus, the noncontrast MRI could be used as a screening tool to help differentiate G1 and G2/3 tumors.

Currently, most studies have attempted to differentiate between G1 and G2/3 PNETs. However, the 5-year survival rates were 75%, 62%, and 7% for G1, G2, and G3, respectively^[52]. It would be more valuable to show the diagnostic values of the nomogram model in differentiating G1/G2 and G3. Furthermore, the G3 tumors are divided into two subgroups: Well-differentiated PNETs G3 and PNEC^[53]. The prognosis of the two subgroups is also different. Further studies are now needed to

differentiate well-differentiated PNET G3 and PNEC, and between PNETs G1/G2 and G3.

PANCREATIC TUMOR CHARACTERIZATION

Autoimmune pancreatitis vs pancreatic ductal adenocarcinoma

AIP has similar clinical and radiological presentations to PDAC, but the treatments of these two entities are different. Patients with AIP might be treated with oral corticosteroids, but patients with PDAC need surgical resection and chemotherapy. Thus, the differentiation of these two entities is imperative to avoid unnecessary surgical resections in patients with AIP or delayed treatment in patients with PDAC.

Park *et al*^[54] used CT-based machine learning of radiomic features to distinguish AIP from PDAC. Eighty-nine patients with AIP and 93 patients with PDAC were retrospectively included. Four-hundred-thirty-one radiomic features were extracted, and a RF method was used to discriminate AIP from PDAC. The radiomic features help differentiate AIP from PDAC with a sensitivity of 89.7%, specificity of 100%, accuracy of 95.2%, and AUC of 0.975.

Zhang *et al*^[55] used 18F FDG PET/CT to distinguish AIP from PDAC in 111 patients (AIP = 45, PDAC = 66). They extracted 251 features from 2D and 3D images and recombined these features into five feature sets according to their modalities and dimensions. Four machine learning classifiers were evaluated. CT features and 3D features performed better than PET features and 2D features, respectively. Multidomain features were superior to single domain features. In addition, the combination of the SVM-recursive feature elimination feature selection strategy and linear SVM classifier had the best performance (AUC = 0.93, accuracy = 0.85). The radiomics model was significantly superior to both human doctors and clinical factors-based prediction models.

The results of these studies are encouraging. For future work, combined features extracted from CNNs and more clinical factors to differentiate these two diseases would be an interesting direction to pursue.

Mass-forming pancreatitis vs pancreatic ductal adenocarcinoma

Ren *et al*^[56] used arterial and portal phase CT texture analysis to differentiate 30 patients with MFP and 79 patients with PDAC. Arterial CT attenuation, arterial, and portal enhancement ratios of MFP were higher than PDAC. Arterial CT attenuation and pancreatic duct penetrating sign were independent predictors in multivariate analysis. AUC of imaging feature-based, texture feature-based in arterial and portal phases, and the combined models were 0.84, 0.96, 0.93, and 0.98, respectively. Thus, CT texture analysis holds great potential to differentiate MFP from PDAC.

Mashayekhi *et al*^[57] used CT radiomics to differentiate 56 patients with recurrent acute pancreatitis ($n = 20$), functional abdominal pain ($n = 19$), or chronic pancreatitis ($n = 17$). In 54 radiomic features extracted by one-vs-one Isomap SVM classifier, 11 radiomic features were significantly different between the patient groups with an overall accuracy of 82.1%.

Serous and mucinous cystadenomas

Yang *et al*^[58] used CT textural features in the differential diagnosis of pancreatic serous cystadenomas ($n = 53$) and mucinous cystadenomas ($n = 25$). Textural parameters were analyzed using RF and LASSO methods. Patients were divided into training and validation sets with a ratio of 4:1. Radiomic features were able to separate serous from mucinous cystadenomas in both the training group (slice thickness of 5 mm, AUC 0.72, accuracy 0.86) and the validation group (AUC 0.75, accuracy 0.83). These results might provide a noninvasive approach to determine whether surgery or imaging follow up is suitable for these patients.

CHALLENGES AND PROSPECTS OF ARTIFICIAL INTELLIGENCE IN THE PANCREAS

There are three main challenges for the application of AI in the pancreas. First, the image analysis methods are diverse and variable, so many study results are inconsistent and contradictory. To ensure the availability of accurate and reproducible radiomics data, the initiatives to standardize the development of quantitative imaging

biomarkers have recently been developed^[59]. Second, the public data of pancreatic imaging available for machine-learning is insufficient, because most early pancreatic lesions are small and occult, and require labor-intensive work from experienced radiologists to label the target lesion. Automatic detection and segmentation of these pancreatic lesions, either with or without the aid of a radiologist, is needed to solve this issue. Third, most studies are retrospective, with limited clinical, laboratory, and outcome data. Previous studies have shown that combined models of radiomic and clinical factors achieve better performance than each individual model. Upcoming prospective studies that combined radiomics and clinical data, even with genomic data, are warranted. Ultimately, it is only with the availability of robust integrated radiomics and comprehensive clinical data that we can proceed to deploy AI in daily practice to improve the care of our patients.

CONCLUSION

The pancreas has both an endocrine and an exocrine digestive function, and its imaging presentations are diverse and frequently pose a diagnostic dilemma in clinical settings. The use of AI will greatly facilitate accurate pancreatic lesion detection, characterization, treatment response evaluation, and prognosis prediction in these patients. Currently, radiomics is under rigorous investigation in various pancreatic diseases, and recent study results are promising. With the growth of advanced AI technology and the availability of standardized imaging data, it seems likely that we will accomplish the goal of precision medicine and increase patients' outcomes in the near future.

REFERENCES

- 1 **Hosny A**, Parmar C, Quackenbush J, Schwartz LH, Aerts HJWL. Artificial intelligence in radiology. *Nat Rev Cancer* 2018; **18**: 500-510 [PMID: 29777175 DOI: 10.1038/s41568-018-0016-5]
- 2 **Thrall JH**, Li X, Li Q, Cruz C, Do S, Dreyer K, Brink J. Artificial Intelligence and Machine Learning in Radiology: Opportunities, Challenges, Pitfalls, and Criteria for Success. *J Am Coll Radiol* 2018; **15**: 504-508 [PMID: 29402533 DOI: 10.1016/j.jacr.2017.12.026]
- 3 **Savadjiev P**, Chong J, Dohan A, Vakalopoulou M, Reinhold C, Paragios N, Gallix B. Demystification of AI-driven medical image interpretation: past, present and future. *Eur Radiol* 2019; **29**: 1616-1624 [PMID: 30105410 DOI: 10.1007/s00330-018-5674-x]
- 4 **Larue RT**, Defraene G, De Ruysscher D, Lambin P, van Elmpt W. Quantitative radiomics studies for tissue characterization: a review of technology and methodological procedures. *Br J Radiol* 2017; **90**: 20160665 [PMID: 27936886 DOI: 10.1259/bjr.20160665]
- 5 **Savadjiev P**, Chong J, Dohan A, Agnus V, Forghani R, Reinhold C, Gallix B. Image-based biomarkers for solid tumor quantification. *Eur Radiol* 2019; **29**: 5431-5440 [PMID: 30963275 DOI: 10.1007/s00330-019-06169-w]
- 6 **Aerts HJ**, Velazquez ER, Leijenaar RT, Parmar C, Grossmann P, Carvalho S, Bussink J, Monshouwer R, Haibe-Kains B, Rietveld D, Hoebers F, Rietbergen MM, Leemans CR, Dekker A, Quackenbush J, Gillies RJ, Lambin P. Decoding tumour phenotype by noninvasive imaging using a quantitative radiomics approach. *Nat Commun* 2014; **5**: 4006 [PMID: 24892406 DOI: 10.1038/ncomms5006]
- 7 **Aerts HJ**. The Potential of Radiomic-Based Phenotyping in Precision Medicine: A Review. *JAMA Oncol* 2016; **2**: 1636-1642 [PMID: 27541161 DOI: 10.1001/jamaoncol.2016.2631]
- 8 **Liu Z**, Wang S, Dong D, Wei J, Fang C, Zhou X, Sun K, Li L, Li B, Wang M, Tian J. The Applications of Radiomics in Precision Diagnosis and Treatment of Oncology: Opportunities and Challenges. *Theranostics* 2019; **9**: 1303-1322 [PMID: 30867832 DOI: 10.7150/thno.30309]
- 9 **Verma V**, Simone CB 2nd, Krishnan S, Lin SH, Yang J, Hahn SM. The Rise of Radiomics and Implications for Oncologic Management. *J Natl Cancer Inst* 2017; **109**: djx055 [PMID: 28423406 DOI: 10.1093/jnci/djx055]
- 10 **Gillies RJ**, Kinahan PE, Hricak H. Radiomics: Images Are More than Pictures, They Are Data. *Radiology* 2016; **278**: 563-577 [PMID: 26579733 DOI: 10.1148/radiol.2015151169]
- 11 **Afshar P**, Mohammadi A, Plataniotis KN, Oikonomou A, Benali H. From Handcrafted to Deep-Learning-Based Cancer Radiomics Challenges and opportunities. *IEEE Signal Process Mag* 2019; **36**: 132-160 [DOI: 10.1109/Msp.2019.2900993]
- 12 **Truhn D**, Schradling S, Haarbuerger C, Schneider H, Merhof D, Kuhl C. Radiomic versus Convolutional Neural Networks Analysis for Classification of Contrast-enhancing Lesions at Multiparametric Breast MRI. *Radiology* 2019; **290**: 290-297 [PMID: 30422086 DOI: 10.1148/radiol.2018181352]
- 13 **Zhu Y**, Man C, Gong L, Dong D, Yu X, Wang S, Fang M, Wang S, Fang X, Chen X, Tian J. A deep learning radiomics model for preoperative grading in meningioma. *Eur J Radiol* 2019; **116**: 128-134 [PMID: 31153553 DOI: 10.1016/j.ejrad.2019.04.022]
- 14 **Yang X**, Wu L, Zhao K, Ye W, Liu W, Wang Y, Li J, Li H, Huang X, Zhang W, Huang Y, Chen X, Yao S, Liu Z, Liang C. Evaluation of human epidermal growth factor receptor 2 status of breast cancer using preoperative multidetector computed tomography with deep learning and handcrafted radiomics features.

- Chin J Cancer Res* 2020; **32**: 175-185 [PMID: 32410795 DOI: 10.21147/j.issn.1000-9604.2020.02.05]
- 15 **Wu X**, Li Y, Chen X, Huang Y, He L, Zhao K, Huang X, Zhang W, Huang Y, Li Y, Dong M, Huang J, Xia T, Liang C, Liu Z. Deep Learning Features Improve the Performance of a Radiomics Signature for Predicting KRAS Status in Patients with Colorectal Cancer. *Acad Radiol* 2020 [PMID: 31982342 DOI: 10.1016/j.acra.2019.12.007]
 - 16 **Hasan AM**, Jalab HA, Meziane F, Kahtan H, Al-Ahmad AS. Combining Deep and Handcrafted Image Features for MRI Brain Scan Classification. *IEEE Access* 2019; **7**: 79959-79967 [DOI: 10.1109/Access.2019.2922691]
 - 17 **Rawla P**, Sunkara T, Gaduputi V. Epidemiology of Pancreatic Cancer: Global Trends, Etiology and Risk Factors. *World J Oncol* 2019; **10**: 10-27 [PMID: 30834048 DOI: 10.14740/wjon1166]
 - 18 **Chu LC**, Park S, Kawamoto S, Fouladi DF, Shayesteh S, Zinreich ES, Graves JS, Horton KM, Hruban RH, Yuille AL, Kinzler KW, Vogelstein B, Fishman EK. Utility of CT Radiomics Features in Differentiation of Pancreatic Ductal Adenocarcinoma From Normal Pancreatic Tissue. *AJR Am J Roentgenol* 2019; **213**: 349-357 [PMID: 31012758 DOI: 10.2214/AJR.18.20901]
 - 19 **Liu KL**, Wu TH, Chen PT, Tsai YM, Roth H, Wu MS, Liao WC, Wang WC. Deep learning to distinguish pancreatic cancer tissue from non-cancerous pancreatic tissue: a retrospective study with cross-racial external validation. *Lancet Digit Health* 2020; **2**: E303-E313 [DOI: 10.1016/S2589-7500(20)30078-9]
 - 20 **Pietryga JA**, Morgan DE. Imaging preoperatively for pancreatic adenocarcinoma. *J Gastrointest Oncol* 2015; **6**: 343-357 [PMID: 26261722 DOI: 10.3978/j.issn.2078-6891.2015.024]
 - 21 **Li K**, Yao Q, Xiao J, Li M, Yang J, Hou W, Du M, Chen K, Qu Y, Li L, Li J, Wang X, Luo H, Yang J, Zhang Z, Chen W. Contrast-enhanced CT radiomics for predicting lymph node metastasis in pancreatic ductal adenocarcinoma: a pilot study. *Cancer Imaging* 2020; **20**: 12 [PMID: 32000852 DOI: 10.1186/s40644-020-0288-3]
 - 22 **Bian Y**, Guo S, Jiang H, Gao S, Shao C, Cao K, Fang X, Li J, Wang L, Hua W, Zheng J, Jin G, Lu J. Relationship Between Radiomics and Risk of Lymph Node Metastasis in Pancreatic Ductal Adenocarcinoma. *Pancreas* 2019; **48**: 1195-1203 [PMID: 31593021 DOI: 10.1097/MPA.0000000000001404]
 - 23 **Tummers WS**, Groen JV, Sibinga Mulder BG, Farina-Sarasqueta A, Morreau J, Putter H, van de Velde CJ, Vahrmeijer AL, Bonsing BA, Mieog JS, Swijnenburg RJ. Impact of resection margin status on recurrence and survival in pancreatic cancer surgery. *Br J Surg* 2019; **106**: 1055-1065 [PMID: 30883699 DOI: 10.1002/bjs.11115]
 - 24 **Strobel O**, Hank T, Hinz U, Bergmann F, Schneider L, Springfield C, Jäger D, Schirmacher P, Hackert T, Büchler MW. Pancreatic Cancer Surgery: The New R-status Counts. *Ann Surg* 2017; **265**: 565-573 [PMID: 27918310 DOI: 10.1097/SLA.0000000000001731]
 - 25 **Hui B**, Qiu JJ, Liu JH, Ke NW. Identification of Pancreaticoduodenectomy Resection for Pancreatic Head Adenocarcinoma: A Preliminary Study of Radiomics. *Comput Math Methods Med* 2020; **2020**: 2761627 [PMID: 32377222 DOI: 10.1155/2020/2761627]
 - 26 **Bian Y**, Jiang H, Ma C, Cao K, Fang X, Li J, Wang L, Zheng J, Lu J. Performance of CT-based radiomics in diagnosis of superior mesenteric vein resection margin in patients with pancreatic head cancer. *Abdom Radiol (NY)* 2020; **45**: 759-773 [PMID: 31932878 DOI: 10.1007/s00261-019-02401-9]
 - 27 **Terakawa H**, Kitagawa H, Makino I, Hayashi H, Oyama K, Nakagawara H, Miyashita T, Tajima H, Takamura H, Fushida S, Ozaki N, Ohta T. Location of the meso-pancreatoduodenum as a regional lymphatic basin for pancreatic head carcinoma. *Oncol Lett* 2017; **14**: 397-403 [PMID: 28693182 DOI: 10.3892/ol.2017.6138]
 - 28 **Zhang W**, Cai W, He B, Xiang N, Fang C, Jia F. A radiomics-based formula for the preoperative prediction of postoperative pancreatic fistula in patients with pancreaticoduodenectomy. *Cancer Manag Res* 2018; **10**: 6469-6478 [PMID: 30568506 DOI: 10.2147/CMAR.S185865]
 - 29 **Chen X**, Oshima K, Schott D, Wu H, Hall W, Song Y, Tao Y, Li D, Zheng C, Knechtges P, Erickson B, Li XA. Assessment of treatment response during chemoradiation therapy for pancreatic cancer based on quantitative radiomic analysis of daily CTs: An exploratory study. *PLoS One* 2017; **12**: e0178961 [PMID: 28575105 DOI: 10.1371/journal.pone.0178961]
 - 30 **Borazanci E**, Korn R, Liang WS, Guarneri C, Haag S, Snyder C, Hendrickson K, Caldwell L, Von Hoff D, Jameson G. An Analysis of Patients with DNA Repair Pathway Mutations Treated with a PARP Inhibitor. *Oncologist* 2020; **25**: e60-e67 [PMID: 31391296 DOI: 10.1634/theoncologist.2018-0905]
 - 31 **Yue Y**, Osipov A, Fraass B, Sandler H, Zhang X, Nissen N, Hendifar A, Tuli R. Identifying prognostic intratumor heterogeneity using pre- and post-radiotherapy 18F-FDG PET images for pancreatic cancer patients. *J Gastrointest Oncol* 2017; **8**: 127-138 [PMID: 28280617 DOI: 10.21037/jgo.2016.12.04]
 - 32 **Xie T**, Wang X, Li M, Tong T, Yu X, Zhou Z. Pancreatic ductal adenocarcinoma: a radiomics nomogram outperforms clinical model and TNM staging for survival estimation after curative resection. *Eur Radiol* 2020; **30**: 2513-2524 [PMID: 32006171 DOI: 10.1007/s00330-019-06600-2]
 - 33 **Cozzi L**, Comito T, Fogliata A, Franzese C, Franceschini D, Bonifacio C, Tozzi A, Di Brina L, Clerici E, Tomatis S, Reggiori G, Lobefalo F, Stravato A, Mancosu P, Zerbi A, Sollini M, Kirienco M, Chiti A, Scorsetti M. Computed tomography based radiomic signature as predictive of survival and local control after stereotactic body radiation therapy in pancreatic carcinoma. *PLoS One* 2019; **14**: e0210758 [PMID: 30657785 DOI: 10.1371/journal.pone.0210758]
 - 34 **Kim HS**, Kim YJ, Kim KG, Park JS. Preoperative CT texture features predict prognosis after curative resection in pancreatic cancer. *Sci Rep* 2019; **9**: 17389 [PMID: 31757989 DOI: 10.1038/s41598-019-53831-w]
 - 35 **Yun G**, Kim YH, Lee YJ, Kim B, Hwang JH, Choi DJ. Tumor heterogeneity of pancreas head cancer assessed by CT texture analysis: association with survival outcomes after curative resection. *Sci Rep* 2018; **8**: 7226 [PMID: 29740111 DOI: 10.1038/s41598-018-25627-x]
 - 36 **Eilaghi A**, Baig S, Zhang Y, Zhang J, Karanicolas P, Gallinger S, Khalvati F, Haider MA. CT texture features are associated with overall survival in pancreatic ductal adenocarcinoma - a quantitative analysis. *BMC Med Imaging* 2017; **17**: 38 [PMID: 28629416 DOI: 10.1186/s12880-017-0209-5]

- 37 **Cheng SH**, Cheng YJ, Jin ZY, Xue HD. Unresectable pancreatic ductal adenocarcinoma: Role of CT quantitative imaging biomarkers for predicting outcomes of patients treated with chemotherapy. *Eur J Radiol* 2019; **113**: 188-197 [PMID: 30927946 DOI: 10.1016/j.ejrad.2019.02.009]
- 38 **Sandrasegaran K**, Lin Y, Asare-Sawiri M, Taiyini T, Tann M. CT texture analysis of pancreatic cancer. *Eur Radiol* 2019; **29**: 1067-1073 [PMID: 30116961 DOI: 10.1007/s00330-018-5662-1]
- 39 **Hyun SH**, Kim HS, Choi SH, Choi DW, Lee JK, Lee KH, Park JO, Lee KH, Kim BT, Choi JY. Intratumoral heterogeneity of (18)F-FDG uptake predicts survival in patients with pancreatic ductal adenocarcinoma. *Eur J Nucl Med Mol Imaging* 2016; **43**: 1461-1468 [PMID: 26872788 DOI: 10.1007/s00259-016-3316-6]
- 40 **Lim J**, Allen PJ. The diagnosis and management of intraductal papillary mucinous neoplasms of the pancreas: has progress been made? *Updates Surg* 2019; **71**: 209-216 [PMID: 31175628 DOI: 10.1007/s13304-019-00661-0]
- 41 **Chakraborty J**, Midya A, Gazit L, Attiyeh M, Langdon-Embry L, Allen PJ, Do RKG, Simpson AL. CT radiomics to predict high-risk intraductal papillary mucinous neoplasms of the pancreas. *Med Phys* 2018; **45**: 5019-5029 [PMID: 30176047 DOI: 10.1002/mp.13159]
- 42 **Corral JE**, Hussein S, Kandel P, Bolan CW, Bagci U, Wallace MB. Deep Learning to Classify Intraductal Papillary Mucinous Neoplasms Using Magnetic Resonance Imaging. *Pancreas* 2019; **48**: 805-810 [PMID: 31210661 DOI: 10.1097/MPA.0000000000001327]
- 43 **Hanania AN**, Bantis LE, Feng Z, Wang H, Tamm EP, Katz MH, Maitra A, Koay EJ. Quantitative imaging to evaluate malignant potential of IPMNs. *Oncotarget* 2016; **7**: 85776-85784 [PMID: 27588410 DOI: 10.18632/oncotarget.11769]
- 44 **Permuth JB**, Choi J, Balarunathan Y, Kim J, Chen DT, Chen L, Orcutt S, Doepker MP, Gage K, Zhang G, Latifi K, Hoffe S, Jiang K, Coppola D, Centeno BA, Magliocco A, Li Q, Trevino J, Merchant N, Gillies R, Malafa M; Florida Pancreas Collaborative. Combining radiomic features with a miRNA classifier may improve prediction of malignant pathology for pancreatic intraductal papillary mucinous neoplasms. *Oncotarget* 2016; **7**: 85785-85797 [PMID: 27589689 DOI: 10.18632/oncotarget.11768]
- 45 **Guilmette JM**, Nosé V. Neoplasms of the Neuroendocrine Pancreas: An Update in the Classification, Definition, and Molecular Genetic Advances. *Adv Anat Pathol* 2019; **26**: 13-30 [PMID: 29912000 DOI: 10.1097/PAP.0000000000000201]
- 46 **D'Onofrio M**, Ciaravino V, Cardobi N, De Robertis R, Cingarlini S, Landoni L, Capelli P, Bassi C, Scarpa A. CT Enhancement and 3D Texture Analysis of Pancreatic Neuroendocrine Neoplasms. *Sci Rep* 2019; **9**: 2176 [PMID: 30778137 DOI: 10.1038/s41598-018-38459-6]
- 47 **Guo C**, Zhuge X, Wang Z, Wang Q, Sun K, Feng Z, Chen X. Textural analysis on contrast-enhanced CT in pancreatic neuroendocrine neoplasms: association with WHO grade. *Abdom Radiol (NY)* 2019; **44**: 576-585 [PMID: 30182253 DOI: 10.1007/s00261-018-1763-1]
- 48 **Canellas R**, Burk KS, Parakh A, Sahani DV. Prediction of Pancreatic Neuroendocrine Tumor Grade Based on CT Features and Texture Analysis. *AJR Am J Roentgenol* 2018; **210**: 341-346 [PMID: 29140113 DOI: 10.2214/AJR.17.18417]
- 49 **Liang W**, Yang P, Huang R, Xu L, Wang J, Liu W, Zhang L, Wan D, Huang Q, Lu Y, Kuang Y, Niu T. A Combined Nomogram Model to Preoperatively Predict Histologic Grade in Pancreatic Neuroendocrine Tumors. *Clin Cancer Res* 2019; **25**: 584-594 [PMID: 30397175 DOI: 10.1158/1078-0432.CCR-18-1305]
- 50 **Gu D**, Hu Y, Ding H, Wei J, Chen K, Liu H, Zeng M, Tian J. CT radiomics may predict the grade of pancreatic neuroendocrine tumors: a multicenter study. *Eur Radiol* 2019; **29**: 6880-6890 [PMID: 31227882 DOI: 10.1007/s00330-019-06176-x]
- 51 **Bian Y**, Zhao Z, Jiang H, Fang X, Li J, Cao K, Ma C, Guo S, Wang L, Jin G, Lu J, Xu J. Noncontrast Radiomics Approach for Predicting Grades of Nonfunctional Pancreatic Neuroendocrine Tumors. *J Magn Reson Imaging* 2020 [PMID: 32343872 DOI: 10.1002/jmri.27176]
- 52 **Strosberg JR**, Weber JM, Feldman M, Coppola D, Meredith K, Kvols LK. Prognostic validity of the American Joint Committee on Cancer staging classification for midgut neuroendocrine tumors. *J Clin Oncol* 2013; **31**: 420-425 [PMID: 23248248 DOI: 10.1200/JCO.2012.44.5924]
- 53 **Lee L**, Ito T, Jensen RT. Prognostic and predictive factors on overall survival and surgical outcomes in pancreatic neuroendocrine tumors: recent advances and controversies. *Expert Rev Anticancer Ther* 2019; **19**: 1029-1050 [PMID: 31738624 DOI: 10.1080/14737140.2019.1693893]
- 54 **Park S**, Chu LC, Hruban RH, Vogelstein B, Kinzler KW, Yuille AL, Fouladi DF, Shayesteh S, Ghandili S, Wolfgang CL, Burkhart R, He J, Fishman EK, Kawamoto S. Differentiating autoimmune pancreatitis from pancreatic ductal adenocarcinoma with CT radiomics features. *Diagn Interv Imaging* 2020 [PMID: 32278586 DOI: 10.1016/j.diii.2020.03.002]
- 55 **Zhang Y**, Cheng C, Liu Z, Wang L, Pan G, Sun G, Chang Y, Zuo C, Yang X. Radiomics analysis for the differentiation of autoimmune pancreatitis and pancreatic ductal adenocarcinoma in ¹⁸F-FDG PET/CT. *Med Phys* 2019; **46**: 4520-4530 [PMID: 31348535 DOI: 10.1002/mp.13733]
- 56 **Ren S**, Zhang J, Chen J, Cui W, Zhao R, Qiu W, Duan S, Chen R, Chen X, Wang Z. Evaluation of Texture Analysis for the Differential Diagnosis of Mass-Forming Pancreatitis From Pancreatic Ductal Adenocarcinoma on Contrast-Enhanced CT Images. *Front Oncol* 2019; **9**: 1171 [PMID: 31750254 DOI: 10.3389/fonc.2019.01171]
- 57 **Mashayekhi R**, Parekh VS, Faghih M, Singh VK, Jacobs MA, Zaheer A. Radiomic features of the pancreas on CT imaging accurately differentiate functional abdominal pain, recurrent acute pancreatitis, and chronic pancreatitis. *Eur J Radiol* 2020; **123**: 108778 [PMID: 31846864 DOI: 10.1016/j.ejrad.2019.108778]
- 58 **Yang J**, Guo X, Ou X, Zhang W, Ma X. Discrimination of Pancreatic Serous Cystadenomas From Mucinous Cystadenomas With CT Textural Features: Based on Machine Learning. *Front Oncol* 2019; **9**: 494 [PMID: 31245294 DOI: 10.3389/fonc.2019.00494]
- 59 **Zwanenburg A**, Vallières M, Abdalah MA, Aerts HJWL, Andrearczyk V, Apte A, Ashrafinia S, Bakas S, Beukinga RJ, Boellaard R, Bogowicz M, Boldrini L, Buvat I, Cook GJR, Davatzikos C, Depeursinge A, Desseroit MC, Dinapoli N, Dinh CV, Echegaray S, El Naqa I, Fedorov AY, Gatta R, Gillies RJ, Goh V, Götz M, Guckenberger M, Ha SM, Hatt M, Isensee F, Lambin P, Leger S, Leijenaar RTH, Lenkiewicz J,

Lippert F, Losnegård A, Maier-Hein KH, Morin O, Müller H, Napel S, Nioche C, Orhac F, Pati S, Pfähler EAG, Rahmim A, Rao AUK, Scherer J, Siddique MM, Sijsema NM, Socarras Fernandez J, Spezi E, Steenbakkens RJHM, Tanadini-Lang S, Thorwarth D, Troost EGC, Upadhaya T, Valentini V, van Dijk LV, van Griethuysen J, van Velden FHP, Whybra P, Richter C, Löck S. The Image Biomarker Standardization Initiative: Standardized Quantitative Radiomics for High-Throughput Image-based Phenotyping. *Radiology* 2020; **295**: 328-338 [PMID: [32154773](https://pubmed.ncbi.nlm.nih.gov/32154773/) DOI: [10.1148/radiol.2020191145](https://doi.org/10.1148/radiol.2020191145)]



Machine learning for diagnosis of coronary artery disease in computed tomography angiography: A survey

Feng-Jun Zhao, Si-Qi Fan, Jing-Fang Ren, Karen M von Deneen, Xiao-Wei He, Xue-Li Chen

ORCID number: Feng-Jun Zhao 0000-0001-8658-8412; Si-Qi Fan 0000-0002-8805-7962; Jing-Fang Ren 0000-0002-8070-1282; Karen M von Deneen 0000-0002-5310-1003; Xiao-Wei He 0000-0003-2126-178X; Xue-Li Chen 0000-0002-3898-9892.

Author contributions: Zhao FJ performed the majority of the writing and the investigation of articles; Fan SQ performed writing for coronary plaque detection; Ren JF performed writing for coronary artery extraction; He XW and von Deneen KM polished the language and expression of the paper; Chen XL checked the organization and revised the writing of the paper.

Supported by the National Natural Science Foundation of China, Nos. 61971350, 81627807 and 11727813; the National Key R&D Program of China, No. 2016YFC1300300; the China Postdoctoral Science Foundation, No. 2019M653717; Shaanxi Science Funds for Distinguished Young Scholars, No. 2020JC-27; Fok Ying Tung Education Foundation, No. 161104; and Program for the Young Top-notch Talent of Shaanxi Province.

Conflict-of-interest statement: The authors declare they have no conflicts of interest.

Open-Access: This article is an open-access article that was

Feng-Jun Zhao, Si-Qi Fan, Jing-Fang Ren, Xiao-Wei He, School of Information Science and Technology, Northwest University, Xi'an 710069, Shaanxi Province, China

Feng-Jun Zhao, Si-Qi Fan, Jing-Fang Ren, Xiao-Wei He, Xi'an Key Lab of Radiomics and Intelligent Perception, Northwest University, Xi'an 710069, Shaanxi Province, China

Karen M von Deneen, Xue-Li Chen, Engineering Research Center of Molecular and Neuro Imaging, Ministry of Education, School of Life Science and Technology, Xidian University, Xi'an 710126, Shaanxi Province, China

Corresponding author: Xue-Li Chen, PhD, Professor, Engineering Research Center of Molecular and Neuro Imaging, Ministry of Education, School of Life Science and Technology, Xidian University, No. 266, Xinglong Section of Xifeng Road, Xi'an 710126, Shaanxi Province, China. xlchen@xidian.edu.cn

Abstract

Coronary artery disease (CAD) has become a major illness endangering human health. It mainly manifests as atherosclerotic plaques, especially vulnerable plaques without obvious symptoms in the early stage. Once a rupture occurs, it will lead to severe coronary stenosis, which in turn may trigger a major adverse cardiovascular event. Computed tomography angiography (CTA) has become a standard diagnostic tool for early screening of coronary plaque and stenosis due to its advantages in high resolution, noninvasiveness, and three-dimensional imaging. However, manual examination of CTA images by radiologists has been proven to be tedious and time-consuming, which might also lead to intra- and interobserver errors. Nowadays, many machine learning algorithms have enabled the (semi-)automatic diagnosis of CAD by extracting quantitative features from CTA images. This paper provides a survey of these machine learning algorithms for the diagnosis of CAD in CTA images, including coronary artery extraction, coronary plaque detection, vulnerable plaque identification, and coronary stenosis assessment. Most included articles were published within this decade and are found in the Web of Science. We wish to give readers a glimpse of the current status, challenges, and perspectives of these machine learning-based analysis methods for automatic CAD diagnosis.

Key words: Machine learning; Deep learning; Coronary artery disease; Atherosclerotic plaque; Vulnerability; Stenosis; Segmentation; Computed tomography angiography

selected by an in-house editor and fully peer-reviewed by external reviewers. It is distributed in accordance with the Creative Commons Attribution NonCommercial (CC BY-NC 4.0) license, which permits others to distribute, remix, adapt, build upon this work non-commercially, and license their derivative works on different terms, provided the original work is properly cited and the use is non-commercial. See: <http://creativecommons.org/licenses/by-nc/4.0/>

Manuscript source: Invited manuscript

Received: May 7, 2020

Peer-review started: May 7, 2020

First decision: June 4, 2020

Revised: June 12, 2020

Accepted: June 17, 2020

Article in press: June 17, 2020

Published online: June 28, 2020

P-Reviewer: Chello M, Dai X, Korosoglou G

S-Editor: Wang JL

L-Editor: Filipodia

E-Editor: Xing YX



©The Author(s) 2020. Published by Baishideng Publishing Group Inc. All rights reserved.

Core tip: There are reviews that contributed to the segmentation of the coronary artery, detection of calcified plaques, and calculation of fractional flow reserve. To the best of our knowledge, this is the first paper to survey the machine learning algorithms for the diagnosis of coronary artery disease in computed tomography angiography images, including extraction of coronary arteries, detection of calcified, soft and mixed plaques, identification of plaque vulnerability features including low density plaque, positive remodeling, spot calcification, and napkin ring sign, assessment of both anatomically and hemodynamically significant stenosis, and the challenges and perspectives of these machine learning-based analysis methods.

Citation: Zhao FJ, Fan SQ, Ren JF, von Deneen KM, He XW, Chen XL. Machine learning for diagnosis of coronary artery disease in computed tomography angiography: A survey. *Artif Intell Med Imaging* 2020; 1(1): 31-39

URL: <https://www.wjgnet.com/2644-3260/full/v1/i1/31.htm>

DOI: <https://dx.doi.org/10.35711/aimi.v1.i1.31>

INTRODUCTION

Coronary artery disease (CAD) has become a major illness endangering human health, which caused more than 17.6 million deaths worldwide in 2016^[1]. Atherosclerotic plaque is the pathological basis of CAD, especially vulnerable plaques without obvious symptoms in the early stage. Once a rupture occurs, it will lead to severe coronary stenosis, which in turn may trigger a major adverse cardiovascular event^[2]. Therefore in CAD diagnosis, it is urgent to accurately detect coronary plaques, identify their vulnerable features, and assess the resulting stenosis. Computed tomography angiography (CTA) has become a standard diagnostic tool for early screening of CAD due to its advantages in high resolution, noninvasiveness, and three-dimensional (3D) imaging^[3]. However, manual examination of CTA images by radiologists has been proven to be tedious and time-consuming, which might also lead to intra- and interobserver errors^[4].

To date, many state-of-the-art machine learning (ML) algorithms have enabled the (semi-)automatic diagnosis of CAD by extracting quantitative features from CTA images. These ML algorithms can be grouped into: (1) Conventional ML algorithms that are typically based on the predefined or hand-crafted features, such as linear regression, support vector machine (SVM), and random forests; and (2) Deep learning (DL) algorithms that can directly learn features from original medical images, such as the convolutional neural network (CNN) and recurrent neural network.

There are some reviews that contributed to the segmentation of the coronary artery^[5], detection of calcified plaques^[6], and calculation of fractional flow reserve (FFR) with both the rule-based (non-ML) and ML-based methods^[7]. This paper provides a survey of the above two groups of ML methods in (semi-)automatic diagnosis of CAD, including coronary artery extraction, coronary plaque detection, vulnerable plaque identification, and coronary stenosis assessment (Figure 1 and Table 1). Most included articles were published within this decade and appear in the Web of Science. Instead of exhaustively listing all of the ML methods of coronary plaque diagnosis, we focus on typical ML-based methods with CTA images in recent years and summarize the challenges regarding these methods.

CORONARY ARTERY EXTRACTION

Due to the tortuous structure of the coronary arteries, it is necessary to perform multiplanar reconstruction or curved planar reconstruction visualization of CTA images before CAD diagnosis^[8]. The reconstruction of both multiplanar reconstruction and curved planar reconstruction images relies on the extraction of coronary artery trees. In addition, some studies have directly carried out a plaque analysis along the cross-section perpendicular to the coronary artery^[9,10]. It can be seen that the accurate extraction of coronary arteries plays an indispensable role in CAD diagnosis. Manual

Table 1 Summary of different machine learning-based methods used in coronary artery disease diagnosis

CAD diagnosis	Method	Task	Category
Coronary artery extraction			
Schaap <i>et al</i> ^[14]	Linear and nonlinear regression	Artery	ML
Huang <i>et al</i> ^[15]	3D U-net	Artery	DL
Kong <i>et al</i> ^[16]	ConvRNN + ConvGRU	Artery	DL
Shen <i>et al</i> ^[17]	3D FCN + level set	Artery	DL
Wu <i>et al</i> ^[18]	CNN + nearest neighbor search	Artery	DL
Wolterink <i>et al</i> ^[19]	3D dilated CNN	Centerline	DL
Coronary plaque detection			
Mittal <i>et al</i> ^[20]	PBT, RF	Calcified	ML
Kurkure <i>et al</i> ^[21]	SVM	Calcified	ML
Wei <i>et al</i> ^[22]	Linear discriminant analysis	Soft	ML
Jawaid <i>et al</i> ^[23]	SVM	Soft	ML
Tessmann <i>et al</i> ^[24]	AdaBoost	Multiple	ML
Kelm <i>et al</i> ^[25]	PBT, RF	Multiple	ML
Zhao <i>et al</i> ^[26]	SVM	Multiple	ML
Zreik <i>et al</i> ^[27]	CNN + RNN	Multiple	DL
Huo <i>et al</i> ^[28]	Attention recognition dual network	Calcified	DL
Vulnerable plaque identification			
Kolossváry <i>et al</i> ^[33]	Radiomics	NRS	ML
Kolossváry <i>et al</i> ^[2]	Radiomics	LAP &NRS	ML
Kolossváry <i>et al</i> ^[34]	Logistic regression, K-nearest neighbors, RF, least angle regression, naive Bayes, Gaussian process classifier, decision trees, DNN	Advanced lesion	ML, DL
Coronary stenosis assessment			
Zuluaga <i>et al</i> ^[36]	SVM	ASS	ML
Kang <i>et al</i> ^[37]	SVM + formula-based analytical method	ASS	ML
Zreik <i>et al</i> ^[27]	CNN + RNN	ASS	DL
Itu <i>et al</i> ^[41]	DNN	HSS	DL
Wang <i>et al</i> ^[42]	DeepVessel-FFR	HSS	DL
Dey <i>et al</i> ^[43]	Boosted ensemble algorithm	HSS	ML
Kumamaru <i>et al</i> ^[44]	2D conditional generative adversarial network + 3D convolutional ladder network	HSS	DL

ASS: Anatomically significant stenosis; CAD: Coronary artery disease; CNN: Convolutional neural network; ConvGRU: Convolutional gated recurrent unit; ConvRNN: Convolutional recurrent neural network; DL: Deep learning method; DNN: Deep neural network; FCN: Fully convolutional network; FFR: Fractional flow reserve; HSS: Hemodynamically significant stenosis; LAP: Low density plaque; ML: Conventional machine learning method; NRS: Napkin ring sign; PBT: Probability boosting tree; RF: Random forest; RNN: Recurrent neural network; SVM: Support vector machine.

extraction of the coronary arteries is labor intensive and observer dependent. Therefore, automatic/semi-automatic extraction methods have been adopted, such as the Hessian matrix method, mathematical morphology, and minimal cost path^[5,11]. These traditional methods discriminate coronary arteries from the background based on intuitively and exquisitely designed models^[12].

ML methods transfer the segmentation into the problem of pixel classification by assigning each pixel as the coronary artery or background^[13]. Specifically, Schaap *et al*^[14] employed both linear regression and nonlinear regression to learn the arterial geometry and appearance from annotated CTA images, and then made full use of the

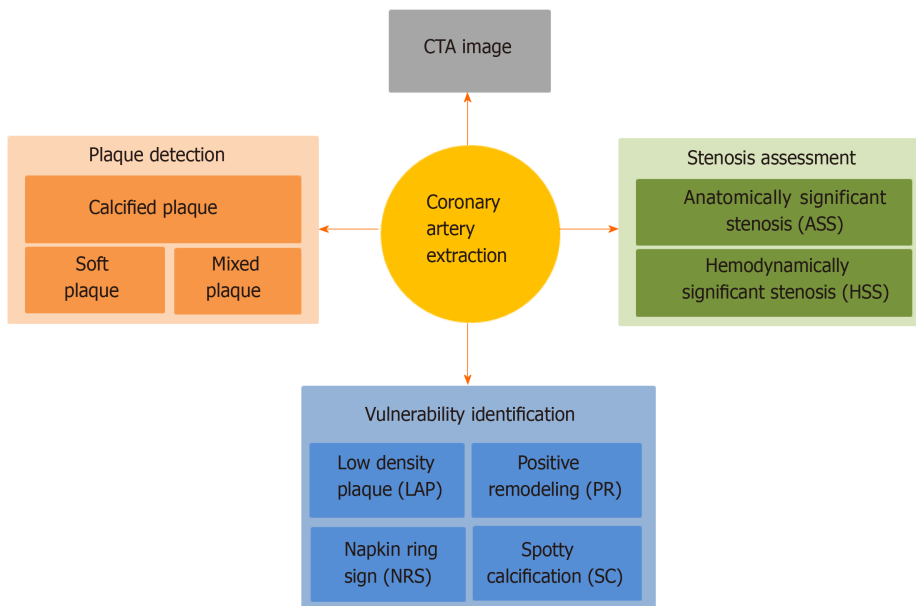


Figure 1 Main topics of this survey, including coronary artery extraction, coronary plaque detection, vulnerable plaque identification, and coronary stenosis assessment. CTA: Computed tomography angiography.

learned knowledge to segment coronary arteries in unseen CTA images. Huang *et al*^[15] introduced the 3D U-net, a typical fully convolutional network (FCN), to segment the coronary artery, which densely performed the pixel-wise classification *via* directly extracting features from CTA images. Alternatively, Kong *et al*^[16] employed a convolutional recurrent neural network and a tree-structured convolutional gated recurrent unit to learn the anatomical structure of the coronary artery, and hereby they achieved accurate segmentation of coronary arteries. Recently, the combination of traditional methods (such as level set and nearest neighbor search) and DL methods (such as fully convolutional network and CNN) were also devised for coronary artery segmentation^[17,18]. Moreover, Wolterink *et al*^[19] trained a 3D dilated CNN to iteratively track the centerline points in CTA images in which the coronary artery could be reconstructed based on the extracted centerline and the radius of each centerline point.

CORONARY PLAQUE DETECTION

Depending on the degree of calcification, coronary plaques can be divided into calcified plaques (full calcification), soft plaques (no calcification), and mixed plaques (partial calcification). Mittal *et al*^[20] used probability boosting trees and random forests to detect coronary calcified plaques with the designed rotation invariant features along the coronary centerline. Kurkure *et al*^[21] adopted an SVM-based method to detect the calcification positions in the aorta and coronary arteries, amongst which they selected coronary calcified plaques. Wei *et al*^[22] proposed a topological soft gradient pre-screening method to obtain candidate soft plaques and then detected soft plaques from the candidate set by a linear discriminant analysis. Jawaid *et al*^[23] divided the coronary cross-section into eight concentric circles. Then they constructed an SVM to identify abnormal coronary segments caused by soft plaques based on the difference in strength stability and localized and identified soft plaques. However, due to large morphological differences between different types of plaques, it is challenging to simultaneously detect multiple types of coronary plaques.

Thus, Tessmann *et al*^[24] performed feature extraction on a cylindrical coronary region of interest and introduced the AdaBoost algorithm to identify calcified plaques and soft plaques. Kelm *et al*^[25] regressed the vessel radius based on the pre-acquired centerline to evaluate stenosis and then constructed a classifier (similar to^[20]) to determine the type of coronary plaques that caused the stenosis, so as to realize the classification of multiple types of plaques. Zhao *et al*^[26] designed a random radial symmetric feature vector and augmented the training data by rotating the cross-section with random angles. Then they trained an SVM to detect and classify

multiclass coronary plaques. With the advantages in representing the complex texture of medical images, DL methods have been brought to the domain of plaque image analysis. Zreik *et al.*^[27] constructed a CNN model to extract the image features of coronary artery sections, and then used a recurrent neural network to fuse the features extracted by multiple CNNs. Finally, they realized the detection and classification of different coronary plaques. Huo *et al.*^[28] proposed a weak supervised attention recognition dual network to perform the detection of calcified plaques, which required only scan-level labels instead of pixel-level labels.

VULNERABLE PLAQUE IDENTIFICATION

CTA imaging can evaluate plaque components in coronary arteries with the diameter greater than 1.5 mm^[29]. Studies found that the plaque vulnerability in CTA images was closely related to low density plaque, positive remodeling, spotty calcification, and napkin ring sign (NRS)^[30,31]. If a coronary plaque contains two or more of the above four vulnerable features, the plaque is more likely to be a vulnerable plaque^[32]. Traditionally, visual inspection performed by radiologists is used to determine whether a coronary plaque contains the above vulnerable features. However, different patients have large individual differences in CTA imaging, resulting in the visual inspection relying heavily on experienced radiologists.

ML-based radiomics can extract a large number of quantitative features from the image to describe the complex texture and spatial structure of the lesion area, providing an automated solution for plaque vulnerability analysis. Kolossváry *et al.*^[33] applied radiomics to the identification of NRS in coronary CTA images, and the results showed that radiomic features were superior to traditional imaging parameters in distinguishing NRS and non-NRS plaques. Afterwards, they identified the low density plaque, NRS, and Na¹⁸F-positive vulnerable features in CTA images^[2]. The results demonstrated that noninvasive CTA diagnosis could accurately distinguish high risk plaques that were previously diagnosed by intravascular ultrasound, optical coherence tomography, and positron emission tomography. In addition, they also collaborated with researchers from the Massachusetts General Hospital to identify advanced coronary atherosclerotic lesions through an ML-based radiomics analysis of *ex vivo* coronary CTA imaging^[34]. The identification results on the cross-section were better than the visual inspection and histogram evaluation.

CORONARY STENOSIS ASSESSMENT

Various types of plaques are the main causes of coronary stenosis, *i.e.* narrowing of the coronary artery lumen, which will restrain blood flow to the myocardium and potentially lead to myocardial ischemia^[35]. Therefore, the assessment of coronary stenosis is also an important aspect in the diagnosis of CAD. Taking physiology into account, coronary stenotic lesions are generally categorized as anatomically significant stenosis and hemodynamically significant stenosis, both of which can be noninvasively assessed by CTA imaging. Anatomically significant stenosis refers to the narrowing of the coronary lumen of at least 50%, which acts as the early assessment for the severity of stenosis in CAD patients. Zuluaga *et al.*^[36] employed SVM to detect coronary stenosis and arterial bifurcation based on the features of concentric circles in two-dimensional cross-sectional images. Kang *et al.*^[37] developed a structured learning algorithm based on SVM and a formula-based analytical method to detect both obstructive (with over 50% stenosis) and non-obstructive (with stenosis between 25% and 50%) lesions. Furthermore, Zreik *et al.*^[27] applied a recurrent CNN on coronary artery multiplanar reconstruction images to detect different grades of anatomically significant stenosis, including no stenosis, nonsignificant stenosis (with less than 50% narrowing), and significant stenosis (with over 50% narrowing). However, the detected anatomically significant stenosis from CTA images has only moderate specificity for predicting hemodynamically significant stenosis (HSS) that causes myocardial ischemia^[38].

Currently, FFR is the standard examination for diagnosis of HSS, which invasively measures the ratio of distal blood flow to the proximal blood flow of the stenosis by inserting a special catheter. FFR estimation based on CTA images (FFT_{CT}) provides a noninvasive alternative for evaluating HSS based on computational fluid dynamics^[39,40], which is accurate but computationally demanding due to the complex iterative computation. To improve the computation efficiency, Itu *et al.*^[41] proposed an

artificial neural network to predict the FFR value of each coronary artery segment based on the geometry and global features extracted from the most severe stenosis. Wang *et al*^[42] developed a DL method (DEEPVESSEL-FFR) to calculate the FFR value from CTA images and predicted the ischemic risk of HSS. Both of the above ML-based FFR prediction methods only rely on the geometry of the coronary artery, leading to their susceptibility to the errors of coronary artery segmentation. Therefore, Dey *et al*^[43] performed the HSS identification with a boosted ensemble algorithm, which combined the geometric features of stenosis with the volumes of plaques, the contrast density difference, and the plaque length. Moreover, Kumamaru *et al*^[44] proposed a 3D DL model to identify patients with at least one HSS, where the model could automatically extract the representative features from the CTA dataset without segmentation or other data manipulation.

CHALLENGES AND PERSPECTIVES

ML algorithms have been widely used in the analysis of CTA images for CAD diagnosis, including the extraction of coronary arteries, diagnosis of plaques, and assessment of stenotic lesions. In particular, DL methods can directly extract task-specific features from input CTA images, which have partially replaced conventional ML methods that depend on the hand-crafted features (or engineered features). Nevertheless, there are some merits and challenges for both the conventional ML methods and DL-based methods. (1) Conventional ML methods are more often involved in plaque and stenosis diagnosis, where the used hand-crafted features were designed according to the visual and clinical experience of radiologists. For this reason, the diagnostic results of these ML methods are inherently explainable, which means they can explicitly show task-relevant quantitative features. Moreover, these ML models are relatively simple and easy to train with only a small number of CTA images. However, the quantitative features used in the ML methods heavily depend on the careful designing by computer vision experts. How to develop or select task-specific quantitative features requires extensive experience accumulation; and (2) DL-based methods are sometimes applied in both coronary artery extraction, and stenosis and plaque diagnosis. DL methods can integrate the whole ML-based analysis workflow including (hand-crafted) feature extraction, feature selection, and classifier training into only one DL model, whose performance would be continuously improved *via* end-to-end learning as long as enough training samples are provided^[45]. However, DL methods generally require a large number of training samples. As is known, manual labeling of coronary data is time-consuming and laborious, so the number of labeled samples is still very limited, even though there are large amounts of patient data in the clinics. Moreover, difficulty in interpretability may also prevent using the DL methods in clinical diagnosis of CAD.

Nevertheless, the DL method has become an important branch in the family of ML algorithms, especially for coronary artery segmentation and coronary stenosis assessment. It is foreseeable that most tasks in CAD diagnosis may start using DL methods or at least the combination of DL and conventional ML methods. For the latter, the DL method functions like a feature extractor, and the classifier from the conventional ML method carries out the subsequent classification. There are some solutions that may address the shortcomings of DL methods. For example, semi-supervised DL methods in natural image processing can potentially solve the classification with only small labeled data. It is reported the prediction error of semi-supervised methods using only 4000 labeled samples in the CIFAR-10 dataset was approximated to supervised learning with 50000 labeled samples^[46,47]. Moreover, some studies tried to explain the decision made by a DL model by double-checking the results with an expert^[48], generating a heat-map to highlight the input regions responsible for a specific task^[49], or projecting the high-dimensional feature space to a bi-dimensional plane^[50].

CONCLUSION

In conclusion, we have surveyed the ML-based CAD diagnostic methods in CTA images in recent years and highlighted the most typical application of both conventional ML and DL methods. We wish to give the readers a glimpse of the current status, challenges, and perspectives of these ML-based analysis methods for automatic CAD diagnosis.

REFERENCES

- 1 **Benjamin EJ**, Muntner P, Alonso A, Bittencourt MS, Callaway CW, Carson AP, Chamberlain AM, Chang AR, Cheng S, Das SR, Delling FN, Djousse L, Elkind MSV, Ferguson JF, Fornage M, Jordan LC, Khan SS, Kissela BM, Knutson KL, Kwan TW, Lackland DT, Lewis TT, Lichtman JH, Longenecker CT, Loop MS, Lutsey PL, Martin SS, Matsushita K, Moran AE, Mussolino ME, O'Flaherty M, Pandey A, Perak AM, Rosamond WD, Roth GA, Sampson UKA, Satou GM, Schroeder EB, Shah SH, Spartano NL, Stokes A, Tirschwell DL, Tsao CW, Turakhia MP, VanWagner LB, Wilkins JT, Wong SS, Virani SS; American Heart Association Council on Epidemiology and Prevention Statistics Committee and Stroke Statistics Subcommittee. Heart Disease and Stroke Statistics-2019 Update: A Report From the American Heart Association. *Circulation* 2019; **139**: e56-e528 [PMID: 30700139 DOI: 10.1161/CIR.0000000000000659]
- 2 **Kolossváry M**, Park J, Bang JI, Zhang J, Lee JM, Paeng JC, Merkely B, Narula J, Kubo T, Akasaka T, Koo BK, Maurovich-Horvat P. Identification of invasive and radionuclide imaging markers of coronary plaque vulnerability using radiomic analysis of coronary computed tomography angiography. *Eur Heart J Cardiovasc Imaging* 2019; **20**: 1250-1258 [PMID: 30838375 DOI: 10.1093/ehjci/jez033]
- 3 **Hampe N**, Wolterink JM, van Velzen SGM, Leiner T, Išgum I. Machine Learning for Assessment of Coronary Artery Disease in Cardiac CT: A Survey. *Front Cardiovasc Med* 2019; **6**: 172 [PMID: 32039237 DOI: 10.3389/fcvm.2019.00172]
- 4 **Litjens G**, Kooi T, Bejnordi BE, Setio AAA, Ciompi F, Ghafoorian M, van der Laak JAWM, van Ginneken B, Sánchez CI. A survey on deep learning in medical image analysis. *Med Image Anal* 2017; **42**: 60-88 [PMID: 28778026 DOI: 10.1016/j.media.2017.07.005]
- 5 **Lesage D**, Angelini ED, Bloch I, Funka-Lea G. A review of 3D vessel lumen segmentation techniques: models, features and extraction schemes. *Med Image Anal* 2009; **13**: 819-845 [PMID: 19818675 DOI: 10.1016/j.media.2009.07.011]
- 6 **Al'Aref SJ**, Anchouche K, Singh G, Slomka PJ, Kolli KK, Kumar A, Pandey M, Maliakal G, van Rosendaal AR, Beecy AN, Berman DS, Leipsic J, Nieman K, Andreini D, Pontone G, Schoepf UJ, Shaw LJ, Chang HJ, Narula J, Bax JJ, Guan Y, Min JK. Clinical applications of machine learning in cardiovascular disease and its relevance to cardiac imaging. *Eur Heart J* 2019; **40**: 1975-1986 [PMID: 30060039 DOI: 10.1093/eurheartj/ehy404]
- 7 **Cook CM**, Petraco R, Shun-Shin MJ, Ahmad Y, Nijjer S, Al-Lamee R, Kikuta Y, Shiono Y, Mayet J, Francis DP, Sen S, Davies JE. Diagnostic Accuracy of Computed Tomography-Derived Fractional Flow Reserve : A Systematic Review. *JAMA Cardiol* 2017; **2**: 803-810 [PMID: 28538960 DOI: 10.1001/jamacardio.2017.1314]
- 8 **Cademartiri F**, La Grutta L, Palumbo A, Malagutti P, Pugliese F, Meijboom WB, Baks T, Mollet NR, Bruining N, Hamers R, de Feyter PJ. Non-invasive visualization of coronary atherosclerosis: state-of-art. *J Cardiovasc Med (Hagerstown)* 2007; **8**: 129-137 [PMID: 17312429 DOI: 10.2459/01.JCM.0000260820.40145.a8]
- 9 **Sankaran S**, Schaap M, Hunley SC, Min JK, Taylor CA, Grady L. In: Ourselin S, Joskowicz L, Sabuncu M, Unal G, Wells W, editors. Medical Image Computing and Computer-Assisted Intervention - MICCAI 2016. MICCAI 2016. Lecture Notes in Computer Science, vol 9902. Cham: Springer 2016; 380-387 [DOI: 10.1007/978-3-319-46726-9_44]
- 10 **Zuluaga MA**, Hernandez Hoyos M, Orkisz M. Feature selection based on empirical-risk function to detect lesions in vascular computed tomography. *Irbm* 2014; **35**: 244-254 [DOI: 10.1016/j.irbm.2014.07.003]
- 11 **Kirbas C**, Quek F. A review of vessel extraction techniques and algorithms. *ACM Comput Surv* 2004; **36**: 81-121 [DOI: 10.1145/1031120.1031121]
- 12 **Zhao F**, Chen Y, Hou Y, He X. Segmentation of blood vessels using rule-based and machine-learning-based methods: a review. *Multimed Syst* 2019; **25**: 109-118 [DOI: 10.1007/s00530-017-0580-7]
- 13 **Tetteh G**, Efremov V, Forkert ND, Schneider M, Kirschke J, Weber B, Zimmer C, Piraud M, Menze BH. DeepVesselNet: Vessel Segmentation, Centerline Prediction, and Bifurcation Detection in 3-D Angiographic Volumes. 2018 Preprint. Available from: [arXiv:1803.09340](https://arxiv.org/abs/1803.09340)
- 14 **Schaap M**, van Walsum T, Neeffjes L, Metz C, Capuano E, de Bruijne M, Niessen W. Robust shape regression for supervised vessel segmentation and its application to coronary segmentation in CTA. *IEEE Trans Med Imaging* 2011; **30**: 1974-1986 [PMID: 21708497 DOI: 10.1109/TMI.2011.2160556]
- 15 **Huang W**, Huang L, Lin Z, Huang S, Chi Y, Zhou J, Zhang J, Tan RS, Zhong L. Coronary Artery Segmentation by Deep Learning Neural Networks on Computed Tomographic Coronary Angiographic Images. *Conf Proc IEEE Eng Med Biol Soc* 2018; **2018**: 608-611 [PMID: 30440470 DOI: 10.1109/EMBC.2018.8512328]
- 16 **Kong B**, Wang X, Bai J, Lu Y, Gao F, Cao K, Xia J, Song Q, Yin Y. Learning tree-structured representation for 3D coronary artery segmentation. *Comput Med Imaging Graph* 2020; **80**: 101688 [PMID: 31926366 DOI: 10.1016/j.compmedimag.2019.101688]
- 17 **Shen Y**, Fang Z, Gao Y, Xiong N, Zhong C, Tang X. Coronary Arteries Segmentation Based on 3D FCN With Attention Gate and Level Set Function. *IEEE Access* 2019; **7**: 42826-42835 [DOI: 10.1109/ACCESS.2019.2908039]
- 18 **Wu A**, Xu Z, Gao M, Buty M, Mollura DJ. Deep vessel tracking: A generalized probabilistic approach via deep learning. In: 2016 IEEE 13th International Symposium on Biomedical Imaging (ISBI). IEEE, 2016: 1363-1367 [DOI: 10.1109/ISBI.2016.7493520]
- 19 **Wolterink JM**, van Hamersvelt RW, Viergever MA, Leiner T, Išgum I. Coronary artery centerline extraction in cardiac CT angiography using a CNN-based orientation classifier. *Med Image Anal* 2019; **51**: 46-60 [PMID: 30388501 DOI: 10.1016/j.media.2018.10.005]
- 20 **Mittal S**, Zheng Y, Georgescu B, Vega-Higuera F, Zhou SK, Meer P, Comaniciu D. Fast Automatic Detection of Calcified Coronary Lesions in 3D Cardiac CT Images. In: Wang F, Yan P, Suzuki K, Shen D, editors. Machine Learning in Medical Imaging. MLMI 2010. Lecture Notes in Computer Science, vol 6357. Berlin, Heidelberg: Springer 2010; 1-9 [DOI: 10.1007/978-3-642-15948-0_1]
- 21 **Kurkure U**, Chittajallu DR, Brunner G, Le YH, Kakadiaris IA. A supervised classification-based method

- for coronary calcium detection in non-contrast CT. *Int J Cardiovasc Imaging* 2010; **26**: 817-828 [PMID: 20229312 DOI: 10.1007/s10554-010-9607-2]
- 22 **Wei J**, Zhou C, Chan HP, Chughtai A, Agarwal P, Kuriakose J, Hadjiiski L, Patel S, Kazerooni E. Computerized detection of noncalcified plaques in coronary CT angiography: evaluation of topological soft gradient prescreening method and luminal analysis. *Med Phys* 2014; **41**: 081901 [PMID: 25086532 DOI: 10.1118/1.4885958]
- 23 **Jawaid MM**, Riaz A, Rajani R, Reyes-Aldasoro CC, Slabaugh G. Framework for detection and localization of coronary non-calcified plaques in cardiac CTA using mean radial profiles. *Comput Biol Med* 2017; **89**: 84-95 [PMID: 28797740 DOI: 10.1016/j.compbiomed.2017.07.021]
- 24 **Tessmann M**, Vega-Higuera F, Fritz D, Scheuering M, Greiner G. Multi-scale feature extraction for learning-based classification of coronary artery stenosis. *SPIE* 2009; 726002
- 25 **Kelm BM**, Mittal S, Zheng Y, Tsybal A, Bernhardt D, Vega-Higuera F, Zhou SK, Meer P, Comaniciu D. Detection, grading and classification of coronary stenoses in computed tomography angiography. *Med Image Comput Comput Assist Interv* 2011; **14**: 25-32 [PMID: 22003680 DOI: 10.1007/978-3-642-23626-6_4]
- 26 **Zhao F**, Wu B, Chen F, Cao X, Yi H, Hou Y, He X, Liang J. An automatic multi-class coronary atherosclerosis plaque detection and classification framework. *Med Biol Eng Comput* 2019; **57**: 245-257 [PMID: 30088125 DOI: 10.1007/s11517-018-1880-6]
- 27 **Zreik M**, van Hamersvelt RW, Wolterink JM, Leiner T, Viergever MA, Isgum I. A Recurrent CNN for Automatic Detection and Classification of Coronary Artery Plaque and Stenosis in Coronary CT Angiography. *IEEE Trans Med Imaging* 2019; **38**: 1588-1598 [PMID: 30507498 DOI: 10.1109/TMI.2018.2883807]
- 28 **Huo Y**, Terry JG, Wang J, Nath V, Bermudez C, Bao S, Parvathaneni P, Carr JJ, Landman BA. Coronary Calcium Detection using 3D Attention Identical Dual Deep Network Based on Weakly Supervised Learning. *Proc SPIE Int Soc Opt Eng* 2019; **10949**: 1094917 [PMID: 31762534 DOI: 10.1117/12.2512541]
- 29 **Kolossváry M**, Szilveszter B, Merkely B, Maurovich-Horvat P. Plaque imaging with CT-a comprehensive review on coronary CT angiography based risk assessment. *Cardiovasc Diagn Ther* 2017; **7**: 489-506 [PMID: 29255692 DOI: 10.21037/cdt.2016.11.06]
- 30 **Rodriguez-Granillo GA**, Carrascosa P, Bruining N, Waksman R, Garcia-Garcia HM. Defining the non-vulnerable and vulnerable patients with computed tomography coronary angiography: evaluation of atherosclerotic plaque burden and composition. *Eur Heart J Cardiovasc Imaging* 2016; **17**: 481-491 [PMID: 26903599 DOI: 10.1093/ehjci/jew012]
- 31 **Motoyama S**, Sarai M, Narula J, Ozaki Y. Coronary CT angiography and high-risk plaque morphology. *Cardiovasc Interv Ther* 2013; **28**: 1-8 [PMID: 23108779 DOI: 10.1007/s12928-012-0140-1]
- 32 **Lee JM**, Bang JI, Koo BK, Hwang D, Park J, Zhang J, Yaliang T, Suh M, Paeng JC, Shiono Y, Kubo T, Akasaka T. Clinical Relevance of ¹⁸F-Sodium Fluoride Positron-Emission Tomography in Noninvasive Identification of High-Risk Plaque in Patients With Coronary Artery Disease. *Circ Cardiovasc Imaging* 2017; **10**: e006704 [PMID: 29133478 DOI: 10.1161/CIRCIMAGING.117.006704]
- 33 **Kolossváry M**, Karády J, Szilveszter B, Kitslaar P, Hoffmann U, Merkely B, Maurovich-Horvat P. Radiomic Features Are Superior to Conventional Quantitative Computed Tomographic Metrics to Identify Coronary Plaques With Napkin-Ring Sign. *Circ Cardiovasc Imaging* 2017; **10**: e006843 [PMID: 29233836 DOI: 10.1161/CIRCIMAGING.117.006843]
- 34 **Kolossváry M**, Karády J, Kikuchi Y, Ivanov A, Schlett CL, Lu MT, Foldyna B, Merkely B, Aerts HJ, Hoffmann U, Maurovich-Horvat P. Radiomics versus Visual and Histogram-based Assessment to Identify Atheromatous Lesions at Coronary CT Angiography: An ex Vivo Study. *Radiology* 2019; **293**: 89-96 [PMID: 31385755 DOI: 10.1148/radiol.2019190407]
- 35 **Fuchs TA**, Fiechter M, Gebhard C, Stehli J, Ghadri JR, Kazakauskaitė E, Herzog BA, Husmann L, Gaemperli O, Kaufmann PA. CT coronary angiography: impact of adapted statistical iterative reconstruction (ASIR) on coronary stenosis and plaque composition analysis. *Int J Cardiovasc Imaging* 2013; **29**: 719-724 [PMID: 23053859 DOI: 10.1007/s10554-012-0134-1]
- 36 **Zuluaga MA**, Magnin IE, Hernández Hoyos M, Delgado Leyton EJ, Lozano F, Orkisz M. Automatic detection of abnormal vascular cross-sections based on density level detection and support vector machines. *Int J Comput Assist Radiol Surg* 2011; **6**: 163-174 [PMID: 20549375 DOI: 10.1007/s11548-010-0494-8]
- 37 **Kang D**, Dey D, Slomka PJ, Arsanjani R, Nakazato R, Ko H, Berman DS, Li D, Kuo CC. Structured learning algorithm for detection of nonobstructive and obstructive coronary plaque lesions from computed tomography angiography. *J Med Imaging (Bellingham)* 2015; **2**: 014003 [PMID: 26158081 DOI: 10.1117/1.JMI.2.1.014003]
- 38 **Meijboom WB**, Van Mieghem CA, van Pelt N, Weustink A, Pugliese F, Mollet NR, Boersma E, Regar E, van Geuns RJ, de Jaegere PJ, Serruys PW, Krestin GP, de Feyter PJ. Comprehensive assessment of coronary artery stenoses: computed tomography coronary angiography versus conventional coronary angiography and correlation with fractional flow reserve in patients with stable angina. *J Am Coll Cardiol* 2008; **52**: 636-643 [PMID: 18702967 DOI: 10.1016/j.jacc.2008.05.024]
- 39 **Taylor CA**, Fonte TA, Min JK. Computational fluid dynamics applied to cardiac computed tomography for noninvasive quantification of fractional flow reserve: scientific basis. *J Am Coll Cardiol* 2013; **61**: 2233-2241 [PMID: 23562923 DOI: 10.1016/j.jacc.2012.11.083]
- 40 **Tesche C**, Vliegenthart R, Duguay TM, De Cecco CN, Albrecht MH, De Santis D, Langenbach MC, Varga-Szemes A, Jacobs BE, Jochheim D, Baquet M, Bayer RR Nd, Litwin SE, Hoffmann E, Steinberg DH, Schoepf UJ. Coronary Computed Tomographic Angiography-Derived Fractional Flow Reserve for Therapeutic Decision Making. *Am J Cardiol* 2017; **120**: 2121-2127 [PMID: 29102036 DOI: 10.1016/j.amjcard.2017.08.034]
- 41 **Itu L**, Rapaka S, Passerini T, Georgescu B, Schwemmer C, Schoebinger M, Flohr T, Sharma P, Comaniciu D. A machine-learning approach for computation of fractional flow reserve from coronary computed tomography. *J Appl Physiol (1985)* 2016; **121**: 42-52 [PMID: 27079692 DOI: 10.1152/japplphysiol.00752.2015]

- 42 **Wang ZQ**, Zhou YJ, Zhao YX, Shi DM, Liu YY, Liu W, Liu XL, Li YP. Diagnostic accuracy of a deep learning approach to calculate FFR from coronary CT angiography. *J Geriatr Cardiol* 2019; **16**: 42-48 [PMID: 30800150 DOI: 10.11909/j.issn.1671-5411.2019.01.010]
- 43 **Dey D**, Gaur S, Ovrehus KA, Slomka PJ, Betancur J, Goeller M, Hell MM, Gransar H, Berman DS, Achenbach S, Botker HE, Jensen JM, Lassen JF, Norgaard BL. Integrated prediction of lesion-specific ischaemia from quantitative coronary CT angiography using machine learning: a multicentre study. *Eur Radiol* 2018; **28**: 2655-2664 [PMID: 29352380 DOI: 10.1007/s00330-017-5223-z]
- 44 **Kumamaru KK**, Fujimoto S, Otsuka Y, Kawasaki T, Kawaguchi Y, Kato E, Takamura K, Aoshima C, Kamo Y, Kogure Y, Inage H, Daida H, Aoki S. Diagnostic accuracy of 3D deep-learning-based fully automated estimation of patient-level minimum fractional flow reserve from coronary computed tomography angiography. *Eur Heart J Cardiovasc Imaging* 2020; **21**: 437-445 [PMID: 31230076 DOI: 10.1093/ehjci/jez160]
- 45 **Afshar P**, Mohammadi A, Plataniotis KN, Oikonomou A, Benali H. From Handcrafted to Deep-Learning-Based Cancer Radiomics: Challenges and Opportunities. *IEEE Signal Process Mag* 2019; **36**: 132-160 [DOI: 10.1109/MSP.2019.2900993]
- 46 **Berthelot D**, Carlini N, Goodfellow I, Papernot N, Oliver A, Raffel C. MixMatch: a holistic approach to semi-supervised learning. 2019 Preprint. Available from: [arXiv:1905.02249](https://arxiv.org/abs/1905.02249)
- 47 **Qizhe X**, Dai Z, Hovy E, Luong MT, Le QV. Unsupervised Data Augmentation for Consistency Training. 2019 Preprint. Available from: [arXiv:1904.12848v1](https://arxiv.org/abs/1904.12848v1)
- 48 **Oakden-Rayner L**, Carneiro G, Bessen T, Nascimento JC, Bradley AP, Palmer LJ. Precision Radiology: Predicting longevity using feature engineering and deep learning methods in a radiomics framework. *Sci Rep* 2017; **7**: 1648 [PMID: 28490744 DOI: 10.1038/s41598-017-01931-w]
- 49 **Jamaludin A**, Kadir T, Zisserman A. SpineNet: Automated classification and evidence visualization in spinal MRIs. *Med Image Anal* 2017; **41**: 63-73 [PMID: 28756059 DOI: 10.1016/j.media.2017.07.002]
- 50 **Ciampi F**, Chung K, van Riel SJ, Setio AAA, Gerke PK, Jacobs C, Scholten ET, Schaefer-Prokop C, Wille MMW, Marchianò A, Pastorino U, Prokop M, van Ginneken B. Towards automatic pulmonary nodule management in lung cancer screening with deep learning. *Sci Rep* 2017; **7**: 46479 [PMID: 28422152 DOI: 10.1038/srep46479]



Acute pancreatitis: A pictorial review of early pancreatic fluid collections

Bo Xiao

ORCID number: Bo Xiao [0000-0001-5862-974X](https://orcid.org/0000-0001-5862-974X).

Author contributions: Xiao B wrote and revised this manuscript.

Conflict-of-interest statement: There is no conflict of interest.

Open-Access: This article is an open-access article that was selected by an in-house editor and fully peer-reviewed by external reviewers. It is distributed in accordance with the Creative Commons Attribution NonCommercial (CC BY-NC 4.0) license, which permits others to distribute, remix, adapt, build upon this work non-commercially, and license their derivative works on different terms, provided the original work is properly cited and the use is non-commercial. See: <http://creativecommons.org/licenses/by-nc/4.0/>

Manuscript source: Invited manuscript

Received: May 28, 2020

Peer-review started: May 28, 2020

First decision: June 5, 2020

Revised: June 8, 2020

Accepted: June 12, 2020

Article in press: June 12, 2020

Published online: June 28, 2020

P-Reviewer: Gokce E

Bo Xiao, Sichuan Key Laboratory of Medical Imaging, Department of Radiology, Affiliated Hospital of North Sichuan Medical College, Nanchong 637000, Sichuan Province, China

Bo Xiao, North Sichuan Medical College, Nanchong 637000, Sichuan Province, China

Corresponding author: Bo Xiao, MD, PhD, Associate Professor, Sichuan Key Laboratory of Medical Imaging, Department of Radiology, Affiliated Hospital of North Sichuan Medical College, No. 63, Wenhua Road, Nanchong 637000, Sichuan Province, China. xiaoboimaging@163.com

Abstract

Acute pancreatitis is a common acute inflammatory disease involving the pancreas and peripancreatic tissues or remote organs. The revised Atlanta classification 2012 of acute pancreatitis divides patients into mild, moderately severe and severe groups. Major changes of the classification include acute fluid collection terminology. However, some inappropriate terms of the radiological diagnosis reports in the daily clinical work or available literature may still be found. The aim of this review article is: to present an image-rich overview of different morphologic characteristics of the early-stage (within 4 wk after symptom onset) local complications associated with acute pancreatitis by computed tomography or magnetic resonance imaging; to clarify confusing imaging concepts for pancreatic fluid collections and underline standardised reporting nomenclature; to assist communication among treating physicians; and to facilitate the implications for clinical management decision-making.

Key words: Acute pancreatitis; Computed tomography; Magnetic resonance imaging; Acute peripancreatic fluid collection; Acute necrotic collection; Complication

©The Author(s) 2020. Published by Baishideng Publishing Group Inc. All rights reserved.

Core tip: To our best of knowledge, this is the first pictorial review that determines the spectrum of magnetic resonance imaging features in patients with acute pancreatitis of distinct early acute necrotic collection compared with acute peripancreatic fluid collection.

Citation: Xiao B. Acute pancreatitis: A pictorial review of early pancreatic fluid collections. *Artif Intell Med Imaging* 2020; 1(1): 40-49

S-Editor: Wang JL
L-Editor: Filipodia
E-Editor: Xing YX



URL: <https://www.wjgnet.com/2644-3260/full/v1/i1/40.htm>
DOI: <https://dx.doi.org/10.35711/aimi.v1.i1.40>

INTRODUCTION

Acute pancreatitis is a common digestive disease, which is related to an acute onset of epigastric pain with/without nausea and vomiting. Cholelithiasis, alcoholism and hyperlipidaemia are the most widely recognised etiological factors in acute pancreatitis patients^[1]. Clinically, physicians often make the accurate diagnosis based on clinical manifestations and biochemical parameters (sufficiently elevated serum lipase or amylase) for the majority of patients with acute pancreatitis^[1]. Indeed, the routine medical imaging for this disease is unwarranted. However, the natural history and consequences of critically ill patients (particularly moderately severe or severe acute pancreatitis) can result in a variety of local complications^[2]. These developments thus prompt imaging to detect clinical complications.

Imaging approaches, especially computed tomography (CT) and magnetic resonance imaging (MRI), are valuable in detecting local complications associated with acute pancreatitis in both the early-phase and the late-phase of disease. With the increasing application of the revised Atlanta classification criteria 2012^[2], radiologists play a crucial role in relevant imaging diagnosis, scientific research and multidisciplinary team communication. Although this classification updates the definitions of acute pancreatitis and many pancreatitis-associated complications, some inappropriate terms of the radiological diagnosis reports in the daily clinical work or available literature may still be found.

Therefore, the purpose of this pictorial article is: To serve as an image-rich overview of different morphologic characteristics of the early-stage (within 4 wk after symptom onset) local complications associated with acute pancreatitis by CT or MR; to clarify confusing imaging concepts and enable standardised reporting nomenclature; to assist communication among treating physicians; and to facilitate the implications for treatments.

DEFINITION AND DIAGNOSIS OF EARLY-STAGE COLLECTIONS ASSOCIATED WITH ACUTE PANCREATITIS

In general, acute pancreatitis is classically divided into two types: Interstitial oedematous pancreatitis and necrotising pancreatitis. Clinically, the majority of patients with acute pancreatitis are present as interstitial oedematous pancreatitis. They have diffuse or localised enlargement of the pancreas owing to inflammatory oedema. On the other hand, necrotising pancreatitis accounts for 20%-30% of acute pancreatitis patients^[3-5], and it is subdivided into three subtypes on the basis of contrast-enhanced CT according to the new Atlanta classification^[2]: (1) Combined pancreatic necrosis and peripancreatic necrosis (most common, approximately 75% of all necrotising pancreatitis); (2) Peripancreatic tissue necrosis alone (less common, with an incidence of approximately 20%)^[6]; and (3) Pancreatic parenchymal necrosis alone (rare, with an incidence of only 5%)^[7-9]. For radiologists, it is crucial to make a distinction between interstitial oedematous pancreatitis and necrotising pancreatitis in diagnosing acute pancreatitis. The correct diagnosis of imaging type can assist in the recognition of subsequent pancreatitis-related complications and application of the proper terminology.

Currently, there are two diagnostic terms for local complications in the early stage of acute pancreatitis: Acute peripancreatic fluid collections (APFCs) and acute necrotic collections (ANCs)^[2]. On the one hand, the characteristics of acute peripancreatic fluid collections include: (1) Arising from interstitial oedematous pancreatitis; (2) Nonencapsulated collections (lack of a well-defined capsule/definable wall); (3) Collection age within the initial 4 wk after symptom onset; (4) Peripancreatic location (surrounding or adjacent to pancreas); and (5) A homogeneous or simple fluid appearance (containing purely fluid) (Figure 1)^[7-9].

On the other hand, the characteristics of acute necrotic collections include: (1) Occurring only in the setting of necrotising pancreatitis; (2) Collections without an encapsulating capsule or over time with poorly organised wall, (3) Collection age within the first 4 wk of this disease; (4) Peripancreatic and pancreatic different

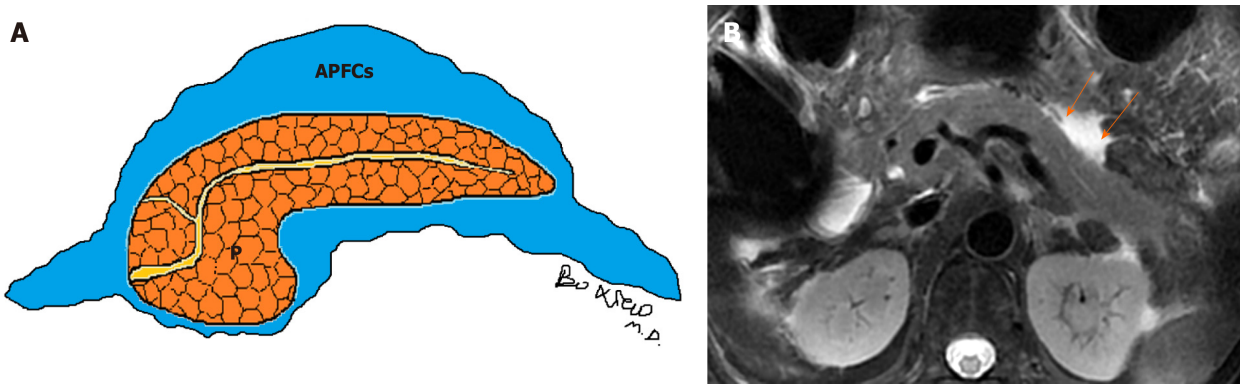


Figure 1 Schematic diagram of acute peripancreatic fluid collections and magnetic resonance imaging of a patient. A: Schematic diagram of acute peripancreatic fluid collections within 4 wk of onset of interstitial oedematous pancreatitis. The term “acute peripancreatic fluid collections” applies only to interstitial oedematous pancreatitis patients; B: A 66-year-old woman with interstitial oedematous pancreatitis. Magnetic resonance imaging axial T2WI image shows a homogeneous fluid finding (arrows) around the pancreas. APFCs: Acute peripancreatic fluid collections; P: Pancreas.

locations (surrounding the pancreas or intrapancreatic extension or both); and (5) A heterogeneous appearance due to containing variable amounts of inflammatory fluid and liquefied or nonliquefied necrotic debris (Figure 2)^[7-10].

LOCATION, SHAPE, SIZE OF APFCs/ANCs

On CT/MRI, acute peripancreatic fluid collections are predominantly localised in peripancreatic areas (e.g., the lesser sac) and the retroperitoneal spaces (e.g., left anterior pararenal space) or peripancreatic fascial planes. They exhibit variable shape and size but mostly present as a uniform linear or strip-shaped liquid appearance^[3-6]. In addition, the volume of APFCs is relatively smaller due to fluid generally confined by a simple retroperitoneum space and/or normal peripancreatic fascial planes (Figure 3).

On the other side, acute necrotic collections often break through the limitation of the interfascial planes and can affect multiple retroperitoneal spaces, interfascial planes, subperitoneal spaces and other abdominal spaces. In fact, they are most frequently situated in the lesser sac and the anterior pararenal spaces, followed by transverse mesocolon, mesenteric root, and thereafter, gastrohepatic, gastrosplenic and gastrocolic ligaments^[11]. Furthermore, these collections may additionally involve the remote regions, such as the pelvic sidewalls and mediastinum. Thus, acute necrotic collections are generally numerous (multiple), irregular and loculated, and the volume of effusion often appears larger than that of acute peripancreatic fluid collections (Figure 4)^[9-11].

DENSITY/SIGNAL INTENSITY, ENHANCEMENT CHARACTERISTICS OF APFCs/ANCs

Acute peripancreatic fluid collections have homogeneous fluid appearances. They are uniformly hypoattenuating on CT and T1 hypointense and T2 hyperintense on MRI. After intravenous contrast-material administration, acute peripancreatic fluid collections are not enhancing owing to the pure fluid nature^[8-10].

In contrast, acute necrotic collections are heterogeneous (Figure 5). There are relatively hyperdense materials (necrotic fragments of pancreas) and/or markedly hypodense fat globules (peripancreatic fat) among hypodense fluid on CT^[6-8]. Similarly, there are varying degrees of round, patchy, strip-shaped T2-hypointense components (adipose fragments or necrotic pancreatic tissue) among T2-hyperintense fluid on MR images^[3-6]. During contrast-enhanced CT/MRI, the internal necrotic debris or trapped fat within acute necrotic collections often does not show enhancement (Figure 5), while the immature, fibrous granulation tissue wall of these collections may be detectable as slight to confluent enhancement (Figure 6).

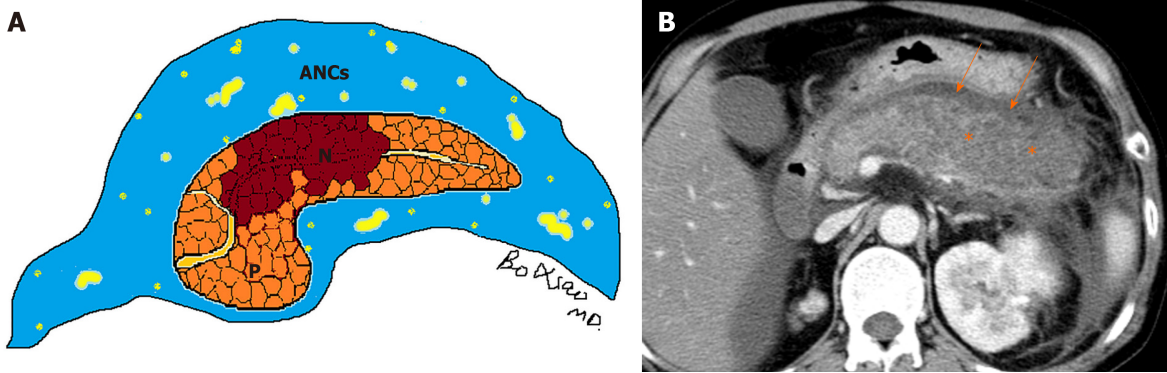


Figure 2 Schematic diagram of acute necrotic collections and computed tomography of a patient. A: Schematic diagram of acute necrotic collections within 4 wk of onset of necrotizing pancreatitis. The term “acute necrotic collections” is diagnosed only in necrotizing pancreatitis patients; B: A 56-year-old man with necrotizing pancreatitis. Axial contrast-enhanced computed tomography image in the venous phase shows a large area of necrosis (asterisks) in the pancreatic body and tail; therefore, a lesser omental sac collection (arrows) should be diagnosed as acute necrotic collections. ANCs: Acute necrotic collections; P: Pancreas; N: Necrosis.

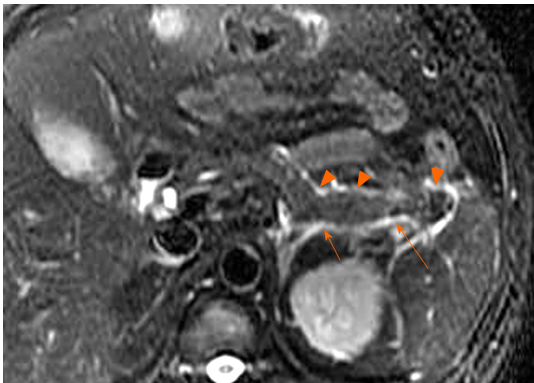


Figure 3 A 40-year-old woman with interstitial oedematous pancreatitis. Magnetic resonance imaging axial T2WI image shows uniform linear liquid hyperintense (acute peripancreatic fluid collections) in the left pararenal anterior spaces (arrowheads) and retromesenteric plane (arrows).

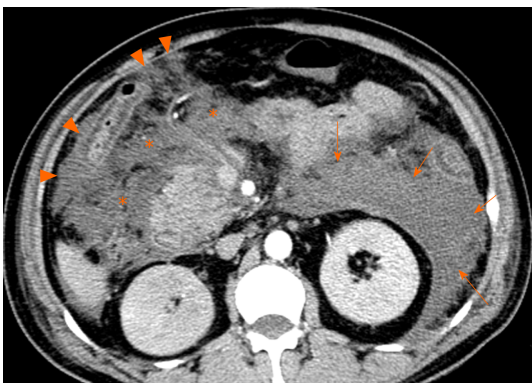


Figure 4 A 53-year-old man with necrotizing pancreatitis. Axial contrast-enhanced computed tomography image in the venous phase shows extensive heterogeneous collections (acute necrotic collections) in the left pararenal anterior spaces (arrows) and the subperitoneal spaces/transverse mesentery areas (asterisks) as well as greater omentum zones (arrowheads).

SECONDARY OR CONCOMITANT CT/MRI FINDINGS OF APFCs/ANCs

In general, (peri)pancreatic fluid collections may also be associated with a variety of complications, which can make the clinical condition more complex. After conservative treatments, acute peripancreatic fluid collections are often absorbed quickly with rare follow-up complications. Most of these patients are discharged within 1-2 wk after admission^[7-9].

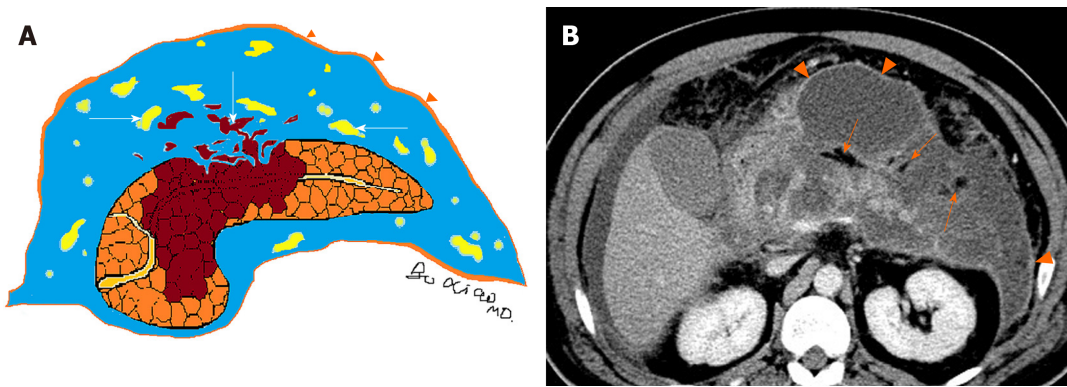


Figure 5 Schematic diagram of heterogeneous collections and computed tomography image of a patient. A: Schematic diagram of heterogeneous collections (acute necrotic collections) secondary to necrotizing pancreatitis. With the prolongation of the disease course, immature poorly organized walls (arrowheads) can gradually form. There are two components within necrotic collections: fat fragments and necrotic parenchymal fragments (arrows); B: A 60-year-old man with necrotizing pancreatitis. Axial contrast-enhanced computed tomography image in the venous phase shows markedly hypodense fat globules (arrows) within acute necrotic collections as well as slight enhancement of capsule (arrowheads) of collections. P: Pancreas; N: Necrosis.

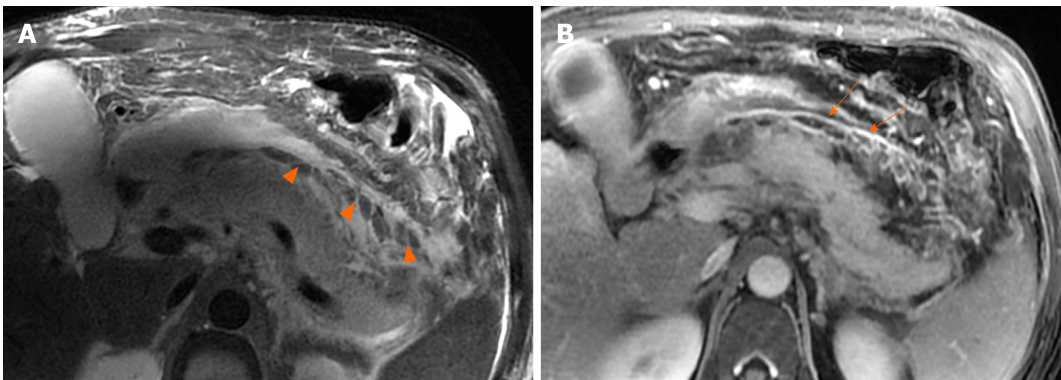


Figure 6 A 46-year-old man with necrotizing pancreatitis. A: Magnetic resonance imaging axial T2WI image shows a number of patchy, strip-shaped T2-hypointense components (necrotic adipose fragments) (arrowheads) among T2-hyperintense fluid; B: Axial contrast-enhanced magnetic resonance imaging shows viable capsule enhancement (arrows).

Clinically, necrotising pancreatitis with acute necrotic collection is mainly seen in patients with moderate severe acute pancreatitis and severe acute pancreatitis, with a longer disease course (lasting several weeks or months). Consequently, secondary infectious complications are more likely to occur in acute necrotic collections, compared with acute peripancreatic fluid collections^[9-11]. Infection should be suspected when there are secondary clinical signs of sepsis, such as a new occurrence of fever and leucocytosis^[8-10]. On CT images, the sign of multiple extraluminal gas or a gas-fluid level in the peripancreatic zones and retroperitoneal spaces is highly suggestive of acute necrotic collections complicated by infection (Figure 7). If clinical manifestations are concordant or needle-guided aspiration confirms the development of infection, then these collections should be classified as infected acute necrotic collections^[9-11]. In this setting, percutaneous aspiration or drain insertion can be performed for the treatment of an infected collection^[11-13].

Moreover, when necrotising pancreatitis affects a large area of intrapancreatic pancreas, it involves the main pancreatic duct (necrosis of the pancreatic duct). Over time, the pancreatic duct rupture or disrupted integrity of the pancreatic duct accompanied with the intrapancreatic acute necrotic collections (liquefied pancreatic tissue) can result in the formation of “disconnected duct syndrome” (Figure 8)^[11,14]. As for this condition, a collection communication with main pancreatic duct is usually evident on MRI and MR cholangiopancreatography (Figure 8). This syndrome may alter treatment but does not affect acute necrotic collection classification, and these patients often require surgical management for a complete recovery^[12-15].

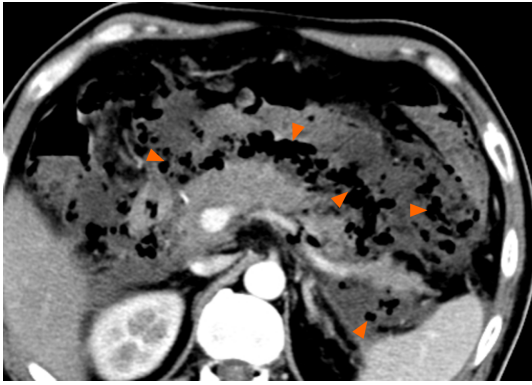


Figure 7 A 59-year-old man with necrotizing pancreatitis complicating infection. Axial contrast-enhanced computed tomography image in the venous phase shows multiple extraluminal gas bubbles (arrowheads) in the peripancreatic and the retroperitoneal spaces, consistent with a pathognomonic sign of the infected necrosis.

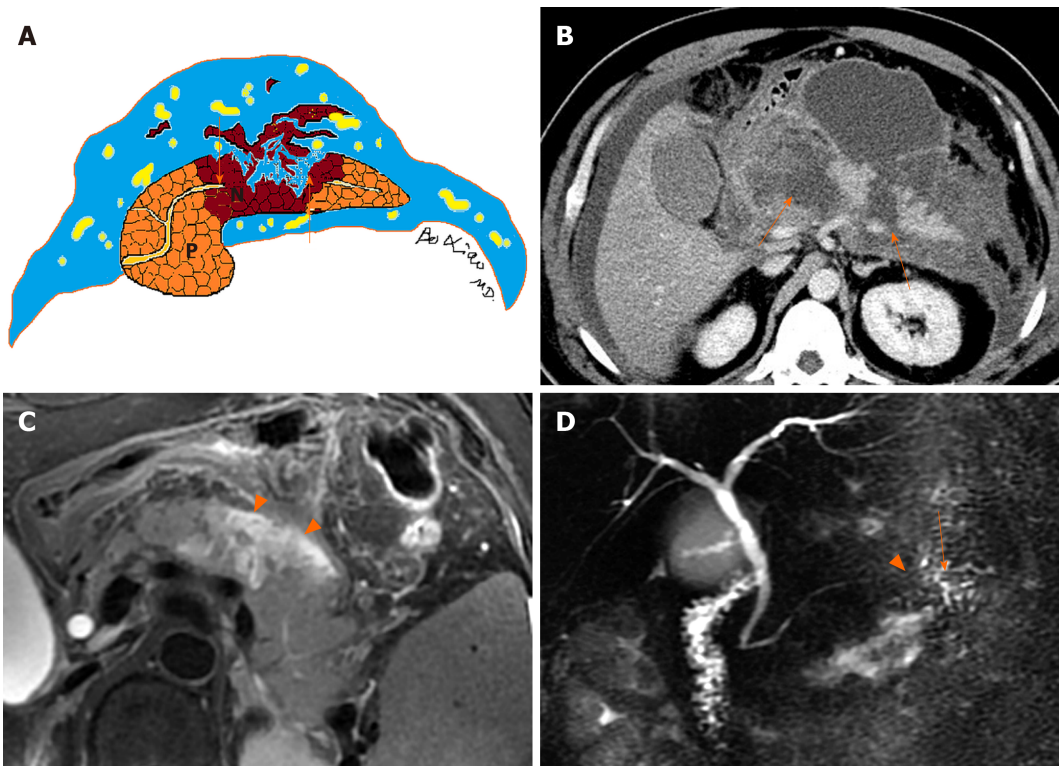


Figure 8 Schematic diagram of disconnected pancreatic duct syndrome and medical images of patients. A: Schematic diagram of disconnected pancreatic duct syndrome. The pancreatic duct rupture and interruption (arrows) resulting from a wide range of liquefied pancreatic body tissue is seen; B: A 60-year-old man with necrotizing pancreatitis. Axial contrast-enhanced computed tomography image in the venous phase shows extensive parenchymal transmural necrosis (arrows) in the region of neck and body of the pancreas. Disconnected main pancreatic duct was proved at surgery; C: A 57-year-old woman with necrotizing pancreatitis. Magnetic resonance imaging axial T2WI image shows a majority of liquefied necroses (arrowheads) in the pancreatic body; D: The main pancreatic duct (arrow) of the tail of pancreas is interrupted (arrowhead) by the mentioned-above lesion. P: Pancreas; N: Necrosis.

TERMINOLOGY MISUSE IN IMAGING REPORTS OF APFCs/ANCs

Depending on the revised Atlanta classification and our clinical practice, common terminology misuse conditions in the daily imaging reports are summarised as follows: (1) On CT/MRI, no necrosis finding was observed in the pancreatic parenchyma, which was assumed to be “interstitial oedematous pancreatitis.” Then the accumulation of fluid in the peripancreatic regions may be misinterpreted as “acute peripancreatic fluid collection.” However, a pitfall is probably present because we may ignore the presence of small “adipose tissue debris” in peripancreatic collections (Figure 9). At this point, it should be diagnosed as “necrotising pancreatitis (peripancreatic necrotic type),” due to necrotic adipose fragments around the pancreas. Therefore, the nomenclature of the collection is referred to as an “acute

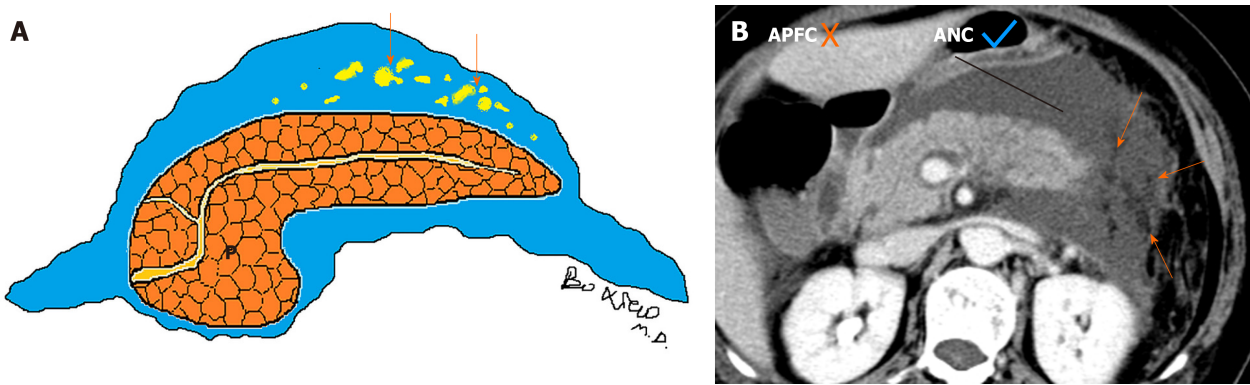


Figure 9 Schematic diagram of necrotizing pancreatitis and computed tomography image of a patient. A: Schematic diagram of necrotizing pancreatitis (peripancreatic necrotic type). Acute necrotic collection involving peripancreatic fat only (arrows) is seen; B: A 58-year-old woman with necrotizing pancreatitis (peripancreatic necrosis only). Axial contrast-enhanced computed tomography image in the venous phase shows normal pancreatic parenchymal enhancement without definite necrosis. A peripancreatic collection may be misdiagnosed as “acute peripancreatic fluid collection.” However, multiple heterogeneous, nonliquid adipose components (arrows) are revealed among the collection. For this reason, it should be considered as acute necrotic collection. P: Pancreas; APFC: Acute peripancreatic fluid collection; ANC: Acute necrotic collection.

necrotic collection” (Figure 9)^[8-11]; (2) On CT/MRI images, when a peripancreatic or retroperitoneal homogeneous collection with uniform fluid density or signal intensity was seen, it may be misinterpreted as an “acute peripancreatic fluid collection.” Instead, if a peripancreatic collection was secondary to known pancreatic parenchymal necrosis and/or haemorrhage, the correct diagnosis term for the collection should be “acute necrotic collection,” even if it is radiologically homogeneous and contains no nonliquefied component (Figure 10)^[4-8]; and (3) As aforementioned content, it may be easier to diagnose a peripancreatic homogeneous collection as “acute peripancreatic fluid collection.” However, if a collection is involving the pancreas parenchyma, a correct term for the surrounding fluid should be diagnosed as “acute necrotic collection” (Figure 11), regardless of the nature of fluid density or signal intensity. In another word, any collection involving the pancreas parenchyma should be determined as necrotising pancreatitis^[8-12].

EXISTING PROBLEMS AND PROSPECTS

Although there are many differences between acute peripancreatic fluid collections and acute necrotic collections, in the clinical practice it is sometimes difficult to accurately distinguish acute peripancreatic fluid collections from acute necrotic collections on CT at the early stage of acute pancreatitis (especially within 2 d of symptom onset). The reasons may be related to the following factors: (1) It may allow sufficient time for completed necrosis of the pancreas and/or peripancreatic fat (findings of solid necrotic materials to liquefy over several days). Thus, heterogeneous contents may not be found within the early-phase fluid. This also explains why an early contrast-enhanced CT may underestimate the eventual degree of (peri)pancreatic necrosis. In this setting, further CT studies after an interval of between 5 d and 7 d should be performed^[2-5]; and (2) Due to the low contrast resolution of CT, it is difficult to detect a small amount of heterogeneous contents. For this purpose, MRI may be required for this distinction because it is very sensitive to the detection of internal architecture of collections (even a small area of heterogeneous debris)^[6-9]. Moreover, MRI diffusion weighted imaging combined with ADC value measurement is helpful for the differential diagnosis of interstitial oedematous pancreatitis and necrotising pancreatitis^[4-6]. Whether diffusion weighted imaging is also valuable for the early differential diagnosis of acute peripancreatic fluid collection and acute necrotic collection may become a direction of future research.

CONCLUSION

To sum up, the natural history and consequences of different pancreatic and peripancreatic collections are now better described and understood. The differential

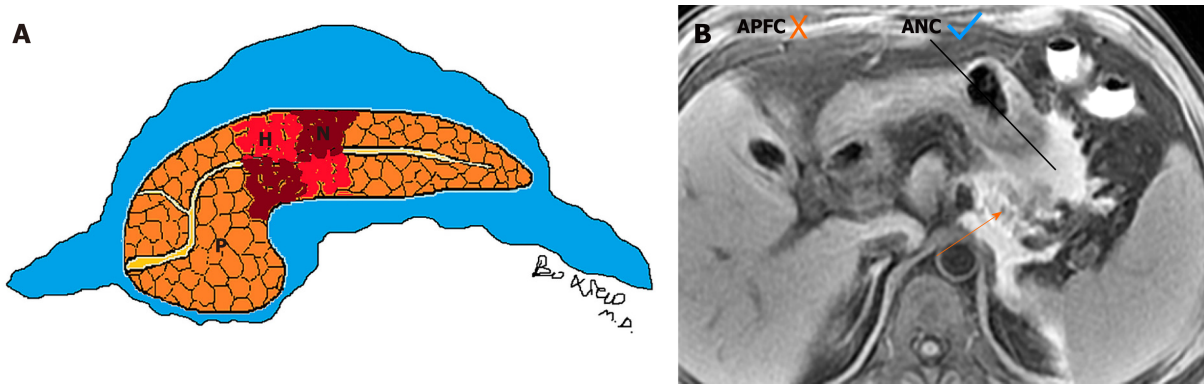


Figure 10 Schematic diagram of necrotizing pancreatitis and magnetic resonance imaging of a patient. A: Schematic diagram of necrotizing pancreatitis (pancreatic parenchymal necrosis alone). The peripancreatic collections are homogeneous; B: A 47-year-old man with necrotizing pancreatitis complicated with haemorrhage. Magnetic resonance imaging axial T1WI image shows peripancreatic homogeneous fluid with greater hyperintense signal. For this reason, it may be misdiagnosed as “acute peripancreatic fluid collection.” However, the necrosis and haemorrhage (arrow) of the body and tail of the pancreas can be indicated. Therefore, the collection should be diagnosed as acute necrotic collection. P: Pancreas, N: Necrosis, H: Haemorrhage; APFC: Acute peripancreatic fluid collection; ANC: Acute necrotic collection.

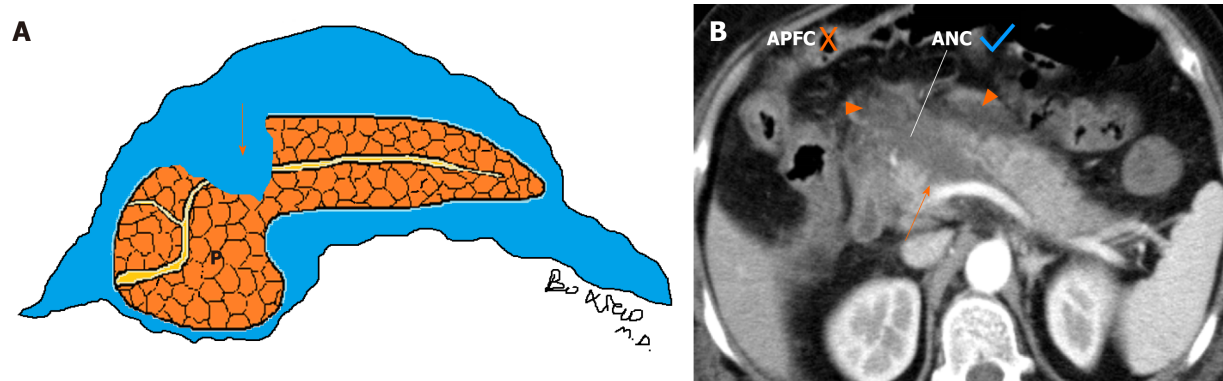


Figure 11 Schematic diagram of acute necrotizing pancreatitis, and extrapancreatic fluid and computed tomography of a patient. A: Schematic diagram of acute necrotizing pancreatitis and extrapancreatic fluid with extension within the pancreatic parenchyma (arrow); B: A 56-year-old woman with acute necrotizing pancreatitis. Axial contrast-enhanced computed tomography image in the late arterial phase shows a peripancreatic homogeneous collection (arrowheads). It may be misinterpreted as “acute peripancreatic fluid collection.” However, note the peripancreatic fluid extends into the parenchyma of the head and neck of the pancreas (arrow). Therefore, it should be diagnosed as an “acute necrotic collection.” P: Pancreas; APFC: Acute peripancreatic fluid collection; ANC: Acute necrotic collection.

diagnosis of these collections within 4 wk of symptom onset is succinctly summarised in [Table 1](#). The accurate description of pancreatitis-associated collections, including location (pancreatic, peripancreatic, others), the presence of contents (liquid, solid, gas), the thickness of collection wall (thin, thick) and the presence or absence of infectious findings will facilitate the radiologic reports in daily practice. Finally, radiologists should be fully aware of the standardised imaging nomenclature on the basis of associated morphologic descriptions. It is necessary for accurate documentation and reporting of academic research, and it is also important to direct implications of care plans for patients with acute pancreatitis.

Table 1 Key points of clinical and imaging differential diagnosis between acute peripancreatic fluid collection and acute necrotic collection

Key points	Acute peripancreatic fluid collection	Acute necrotic collection
Clinical severity	Mostly mild acute pancreatitis	Moderately severe acute pancreatitis or severe acute pancreatitis
Management algorithm	Conservative treatment (usually resolves spontaneously without intervention)	Likely increased morbidity and intervention rates (drainage or surgical treatment)
Course and prognosis	The hospital stay is usually about one week after onset; a good prognosis	Hospitalization often lasts from weeks to months; increased infection and mortality rates
CT/MRI imaging pattern	Occurs only in the setting of interstitial oedematous pancreatitis	Occurs in the setting of acute necrotising pancreatitis (including peripancreatic necrosis only)
Location and number of collections on CT/MRI	Mostly confined to simple retroperitoneal space or interfascial plane	Mostly in transabdominal-pelvic cavities and multiple spaces or interfascial planes
Shape, size, edge	Linear/strip-shaped, a small amount of collections, clear edge	Large patchy-shaped, a large amount of collections, unclear or irregular edge
Density/intense, enhancement characteristics	Homogeneous low density/hypointense T1 hyperintense T2 signal; no enhancement	Mixed features, mainly low density/hypointense T1 /hyperintense T2 signal, containing low density fat/fat signal intensity and low density or hypointense pancreas fragments; fragments are not enhancing
Secondary or concomitant signs	Rare	Frequent secondary infection with “bubble sign” (caused by infection itself or intestinal fistula with adjacent intestine); when a large area of intrapancreatic collections is present, “pancreatic duct disruption syndrome” may occur (further invasive operation is often required)

CT: Computed tomography; MRI: Magnetic resonance imaging.

REFERENCES

- 1 **Yadav D**, Lowenfels AB. The epidemiology of pancreatitis and pancreatic cancer. *Gastroenterology* 2013; **144**: 1252-1261 [PMID: 23622135 DOI: 10.1053/j.gastro.2013.01.068]
- 2 **Banks PA**, Bollen TL, Dervenis C, Gooszen HG, Johnson CD, Sarr MG, Tsiotos GG, Vege SS; Acute Pancreatitis Classification Working Group. Classification of acute pancreatitis--2012: revision of the Atlanta classification and definitions by international consensus. *Gut* 2013; **62**: 102-111 [PMID: 23100216 DOI: 10.1136/gutjnl-2012-302779]
- 3 **Thoeni RF**. The revised Atlanta classification of acute pancreatitis: its importance for the radiologist and its effect on treatment. *Radiology* 2012; **262**: 751-764 [PMID: 22357880 DOI: 10.1148/radiol.11110947]
- 4 **Xiao B**, Xu HB, Jiang ZQ, Zhang J, Zhang XM. Current concepts for the diagnosis of acute pancreatitis by multiparametric magnetic resonance imaging. *Quant Imaging Med Surg* 2019; **9**: 1973-1985 [PMID: 31929970 DOI: 10.21037/qims.2019.11.10]
- 5 **Sun H**, Zuo HD, Lin Q, Yang DD, Zhou T, Tang MY, Wang YXJ, Zhang XM. MR imaging for acute pancreatitis: the current status of clinical applications. *Ann Transl Med* 2019; **7**: 269 [PMID: 31355236 DOI: 10.21037/atm.2019.05.37]
- 6 **Meyrignac O**, Lagarde S, Bournet B, Mokrane FZ, Buscail L, Rousseau H, Otal P. Acute Pancreatitis: Extrapancreatic Necrosis Volume as Early Predictor of Severity. *Radiology* 2015; **276**: 119-128 [PMID: 25642743 DOI: 10.1148/radiol.15141494]
- 7 **Zhao K**, Adam SZ, Keswani RN, Horowitz JM, Miller FH. Acute Pancreatitis: Revised Atlanta Classification and the Role of Cross-Sectional Imaging. *AJR Am J Roentgenol* 2015; **205**: W32-W41 [PMID: 26102416 DOI: 10.2214/AJR.14.14056]
- 8 **Murphy KP**, O'Connor OJ, Maher MM. Updated imaging nomenclature for acute pancreatitis. *AJR Am J Roentgenol* 2014; **203**: W464-W469 [PMID: 25341160 DOI: 10.2214/AJR.13.12222]
- 9 **Türkvtan A**, Erden A, Türkoğlu MA, Seçil M, Yüce G. Imaging of acute pancreatitis and its complications. Part 2: complications of acute pancreatitis. *Diagn Interv Imaging* 2015; **96**: 161-169 [PMID: 24703377 DOI: 10.1016/j.diii.2013.12.018]
- 10 **Bollen TL**. Acute pancreatitis: international classification and nomenclature. *Clin Radiol* 2016; **71**: 121-133 [PMID: 26602933 DOI: 10.1016/j.crad.2015.09.013]
- 11 **Foster BR**, Jensen KK, Bakis G, Shaaban AM, Coakley FV. Revised Atlanta Classification for Acute Pancreatitis: A Pictorial Essay. *Radiographics* 2016; **36**: 675-687 [PMID: 27163588 DOI: 10.1148/rg.2016150097]
- 12 **Sarathi Patra P**, Das K, Bhattacharyya A, Ray S, Hembram J, Sanyal S, Dhali GK. Natural resolution or intervention for fluid collections in acute severe pancreatitis. *Br J Surg* 2014; **101**: 1721-1728 [PMID: 25329330 DOI: 10.1002/bjs.9666]
- 13 **Holleman RA**, Bakker OJ, Boermeester MA, Bollen TL, Bosscha K, Bruno MJ, Buskens E, Dejong CH, van Duijvendijk P, van Eijck CH, Fockens P, van Goor H, van Grevenstein WM, van der Harst E, Heisterkamp J, Hesselink EJ, Hofker S, Houdijk AP, Karsten T, Kruijff PM, van Laarhoven CJ, Laméris JS, van Leeuwen MS, Manusama ER, Molenaar IQ, Nieuwenhuijs VB, van Ramshorst B, Roos D, Rosman C,

- Schaapherder AF, van der Schelling GP, Timmer R, Verdonk RC, de Wit RJ, Gooszen HG, Besselink MG, van Santvoort HC; Dutch Pancreatitis Study Group. Superiority of Step-up Approach vs Open Necrosectomy in Long-term Follow-up of Patients With Necrotizing Pancreatitis. *Gastroenterology* 2019; **156**: 1016-1026 [PMID: 30391468 DOI: 10.1053/j.gastro.2018.10.045]
- 14 **Fischer TD**, Gutman DS, Hughes SJ, Trevino JG, Behrns KE. Disconnected pancreatic duct syndrome: disease classification and management strategies. *J Am Coll Surg* 2014; **219**: 704-712 [PMID: 25065360 DOI: 10.1016/j.jamcollsurg.2014.03.055]
- 15 **van Brunschot S**, van Grinsven J, van Santvoort HC, Bakker OJ, Besselink MG, Boermeester MA, Bollen TL, Bosscha K, Bouwense SA, Bruno MJ, Cappendijk VC, Consten EC, Dejong CH, van Eijck CH, Erkelens WG, van Goor H, van Grevenstein WMU, Haveman JW, Hofker SH, Jansen JM, Laméris JS, van Lienden KP, Meijssen MA, Mulder CJ, Nieuwenhuijs VB, Poley JW, Quispel R, de Ridder RJ, Römken TE, Scheepers JJ, Schepers NJ, Schwartz MP, Seerden T, Spanier BWM, Straathof JWA, Strijker M, Timmer R, Venneman NG, Vleggaar FP, Voermans RP, Witteman BJ, Gooszen HG, Dijkgraaf MG, Fockens P; Dutch Pancreatitis Study Group. Endoscopic or surgical step-up approach for infected necrotising pancreatitis: a multicentre randomised trial. *Lancet* 2018; **391**: 51-58 [PMID: 29108721 DOI: 10.1016/S0140-6736(17)32404-2]



Basic Study

Acoustic concept based on an autonomous capsule and a wideband concentric ring resonator for pathophysiological prevention

Amina Medjdoub, Fabrice Lefebvre, Nadine Saad, Saïd Soudani, Georges Nassar

ORCID number: Amina Medjdoub 0000-0002-7312-6478; Fabrice Lefebvre 0000-0001-8274-0464; Nadine Saad 0000-0001-9091-0793; Saïd Soudani 0000-0002-1934-3615; Georges Nassar 0000-0002-8413-3307

Author contributions: Nassar G was responsible for overall study concept; Medjdoub A and Lefebvre F were responsible for the quantification of the physical and electrical characteristics of sensors; Saad N and Soudani S were responsible of sensor/biological tissue interfaces behavior and signal processing analysis component; Nassar G, Medjdoub A and Lefebvre F were responsible for the experimental concept design and application; all authors reviewed, edited, and approved the final manuscript.

Institutional review board statement: No human and/or animal subjects are involved in this study.

Conflict-of-interest statement: Nothing to disclose.

Data sharing statement: No additional data are available.

Open-Access: This article is an open-access article that was selected by an in-house editor and

Amina Medjdoub, Fabrice Lefebvre, Georges Nassar, Institute of Electronic, Microelectronic and Nanotechnology, Department of Opto-Acousto-Electronic, Université Polytechnique Hauts-de-France, Villeneuve d'Ascq 59652, France

Nadine Saad, Department of Physics, Université Libanaise-Faculté des Sciences, Beyrouth 1000, Lebanon

Saïd Soudani, Signal Processing Department, Université des Sciences et de la Technologie d'Oran, Oran 31000, Algeria

Corresponding author: Georges Nassar, PhD, Professor, Institute of Electronic, Microelectronic and Nanotechnology, Department of Opto-Acousto-Electronic, Université Polytechnique Hauts-de-France, Avenue Henri Poincaré, Cité Scientifique CS 60069, Villeneuve d'Ascq 59652, France. gnassar@uphf.fr

Abstract

BACKGROUND

Research on the performance of elements constituting our modern environment is constantly evolving, both on a daily basis and on technological basis. But to date, the response of the system to the expectations of the population remains too modest.

AIM

To elaborate an ultrasonic technique to scan and evaluate *in-vivo* physiological properties by coupling sensors and multilayer biological tissues model.

METHODS

A low-frequency ultrasonic method (around a frequency of 32 KHz) based on the use of an innovative autonomous ultrasonic capsule as a miniaturized elementary spherical sensor (1 cm of diameter) and micro-rings resonators were examined.

RESULTS

Other their functions as passive listeners for the prevention and diagnosis in physiopathology of the respiratory and laryngeal apparatus, these micro-resonators coupled to the ultrasonic capsule through biological tissues (the body) are capable of evaluating the effects of aggression of the environment on human metabolism.

fully peer-reviewed by external reviewers. It is distributed in accordance with the Creative Commons Attribution NonCommercial (CC BY-NC 4.0) license, which permits others to distribute, remix, adapt, build upon this work non-commercially, and license their derivative works on different terms, provided the original work is properly cited and the use is non-commercial. See: <http://creativecommons.org/licenses/by-nc/4.0/>

Manuscript source: Invited manuscript

Received: May 28, 2020

Peer-review started: May 28, 2020

First decision: June 19, 2020

Revised: June 22, 2020

Accepted: June 25, 2020

Article in press: June 25, 2020

Published online: June 28, 2020

P-Reviewer: Mohammed RHA

S-Editor: Wang JL

L-Editor: A

E-Editor: Wang LL



CONCLUSION

This would allow consequently the detection of some potential diseases at an early stage, even in people who still represent no symptoms, which would permit an early treatment and a higher chance of cure.

Key words: Sensor; Capsule; Acoustics; Ring resonators; Biological tissues

©The Author(s) 2020. Published by Baishideng Publishing Group Inc. All rights reserved.

Core tip: Research on the performance of elements constituting our modern environment is constantly evolving, both on a daily basis and on technological basis. But to date, the response of the system to the expectations of the population remains too modest. The current trend lies in the very definition of performance, seen mainly from the point of view of optimizing the service provided to the users. Estimating it, is putting first the medico-technological coherence that will be measured by its capacity to respond to a certain number of needs of both care and comfort.

Citation: Medjdoub A, Lefebvre F, Saad N, Soudani S, Nassar G. Acoustic concept based on an autonomous capsule and a wideband concentric ring resonator for pathophysiological prevention. *Artif Intell Med Imaging* 2020; 1(1): 50-64

URL: <https://www.wjgnet.com/2644-3260/full/v1/i1/50.htm>

DOI: <https://dx.doi.org/10.35711/aimi.v1.i1.50>

INTRODUCTION

Studying interactions between acoustic and living fields goes far beyond biological and health impact studies. Within the context of the development or application of treatments, we intend to explore potential innovations motivated by the wide variety of medical challenges.

Obtaining continuous measurements is often more difficult and only a few constraining devices (rectal, esophageal probes, *etc.*) allow continuous monitoring of the physiological properties of an individual.

Many of the studies have addressed endoscopic ultrasound applications, the majority of which used wired systems. As an example, Lay *et al*^[1] developed a wired ultrasonic imaging capsule for gastrointestinal disorders combining the imaging capabilities of endoscopic ultrasound. The work of Peng *et al*^[2] focuses more on ultrasonic ablation of cancer cells and He *et al*^[3] combines' optoacoustic interference for these endoscopic characterizations. To this end, de Groen^[4] presents a panoramic view of endoscopic features and associated applications.

The evaluations of the quantities concerned are based on significant parameter uncertainty, which constitutes an undeniable field of application for statistical approaches. In this context and taking into account the limitations and the difficulty of some applications (morphology, age, *etc.*), our work focused on the development of an autonomous information system able to collect data on physiological variations or body composition using vibratory waves. This means of exploration combines endoscopy and ultrasound.

The layout of a sensor network embedded in the body is at the heart of concerns in terms of wave propagation, wave/tissue interactions, and biocompatibility of the radiating elements.

The objective of this work was partly to contribute to the development of innovative radiating structures close to the body (sensors radiating inside the body and through multilayer tissues). The development of a new autonomous ultrasound capsule-based scanning method associated with multilayer models represents a very important challenge given the difficulty of experimental implementation in the low frequency band. This work aimed to obtain conclusive results to assess exposure compared to the thresholds tolerated normatively and to propose an alternative method in order to set a better soft diagnosis to avoid in the limit of possible exposure regarding the harmful radiation [Magnetic resonance imaging (MRI), X-rays, *etc.*]. This device makes it possible to monitor continuously the physiological evolution (mechanical stress, *etc.*) and consequently reduce, by alert, the risks in situations considered as extreme.

To improve understanding and quantify the interaction process of evolving tissue characteristics in real conditions, a new low-frequency ultrasonic technique with a miniaturized elementary spherical sensor that behaves as a point source (capsule) was examined. This source was coupled through tissues to receivers spatially identified on the body and adapted, by their concentric ring shapes, to the central vibration frequency of the transmitter. The use of a dedicated algorithm allowed data logging and triggering of alerts if the threshold of a critical value was exceeded.

Using an embedded electrical control architecture, this “capsule” can simultaneously manage tasks such as acoustic transmission/reception, remote data storage and/or telecommunication, as well as provide extended autonomy, which is currently not available for discrete elements.

Given the technical characteristics of such resonators, the randomly distributed capsule network will be able to deliver useful information regarding the evolution of the mechanical state of a dynamic system. A threshold regarding the desired state set by the user must be included in the device in order to reach optimal decisions.

Figure 1 shows the global concept and the potential application in the biological domain. However, for legislative and regulatory reasons, the concept studied in this paper was validated using biological tissues of animal origin and agar as a coupling medium because its physical properties are close to those of human physiological fluid.

MATERIALS AND METHODS

Resonator devices

Integrated emitter capsule sensor: Contrary to most ultrasonic transmission techniques, our goal was to obtain a low-frequency acoustic point source to generate a spherical wave in the medium. To do this, we used a piezo element for which the frequency was optimized to bring the entire mechanical structure of a small sphere into resonance. The radius of the sphere is smaller than the acoustic wavelength generated in the medium so it can be considered as an acoustic point source.

The resonator is a closed spherical shell composed of two hemispheres made of a biocompatible material. Its inner radius is about 8 mm and it is about 2 mm thick^[5]. Resonance of the overall structure occurs as a result of the vibrations produced by a piezoelectric ring (0.5 mm thick) clamped between the two hemispheres (Figure 1A). This configuration offers a good compromise between a frequency of around 32 kHz suitable for the “ultrasonic” exploration of complex dispersive media and easy decoupling of the mechanical vibration frequency from the process (background noise) “until then considered as an undesirable parameter”.

Fundamental acoustic vibrational mode: Spherical motion

Relatively few studies have investigated miniaturized spherical resonators. The most recent studies concern an ultrasonic capsule device measuring 1 cm × 2.5 cm developed by Wang *et al*^[6] and Memon *et al*^[7] dedicated to scanning the gastrointestinal tract using ultrasound with an external emission provided by active elements positioned around the capsule. In the same context, Cox *et al*^[8] conducted studies regarding the feasibility of a wired ultrasound capsule endoscopy. Walker^[9] and Nasedkin *et al*^[10] developed a theoretical and finite element model of an ultrasonic transducer incorporating spherical resonators. However, a number have been developed over the past decades, especially for studying the properties of gasses and liquids. Mehl *et al*^[11] used a spherical resonator in a frequency range of 4 to 13 kHz to measure the velocity and attenuation of sound in C₂H₄ between 0 and 100 °C and 0.15 to 1.0 MPa. The resonator is made of two aluminum hemispheres with an inner diameter of 127 mm and a thickness of 12.1 mm. He *et al*^[12] developed another spherical resonator to measure sound velocity in the gas phase (argon). The resonator comprises two stainless steel (00Cr17Ni14Mo2 type) hemispheres with an inner radius of 61.77 mm and a working frequency between 1 and 15 kHz. The resonator was placed in a pressurized container that was immersed in a thermos-regulated bath.

Analytical approach

Many studies have been conducted in the field of mechanical vibration of spherical shells for axisymmetric modes. Baker^[13], Wilkinson^[14], Kalnins^[15] and Duffey *et al*^[16], for example, studied the vibration of a macro spherical shell under the effect of transverse shear and rotational inertia.

In what follows, to establish the equations of motion of a spherical shell we

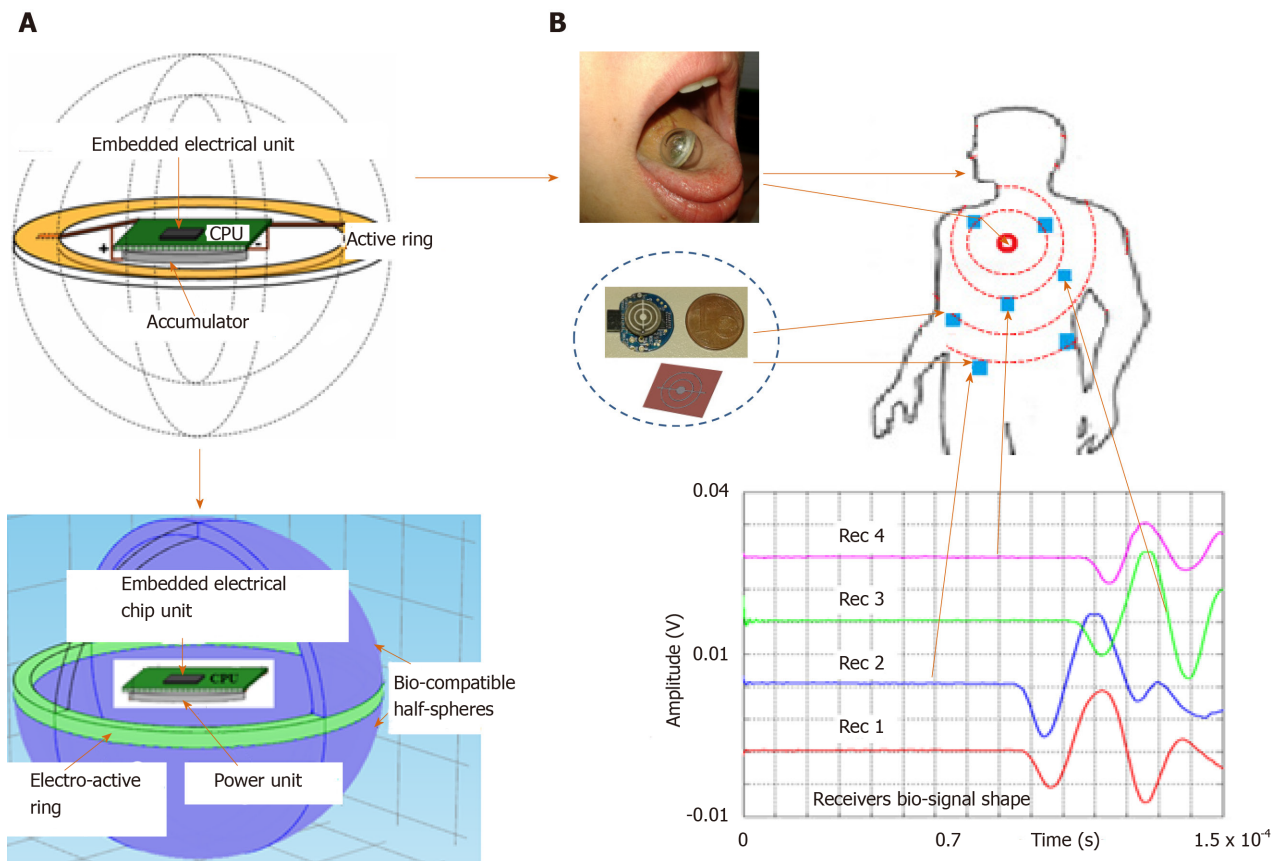


Figure 1 Illustration of the global concept based on a mobile ultrasonic capsule resonator as an emitter and a thin layer concentric rings resonators playing the role of receivers. A: The global concept based on a mobile ultrasonic capsule resonator; B: An emitter and a thin layer concentric rings resonators playing the role of receivers.

considered the fundamental theory of Love based on the Lagrangian formulation. In the case of an undamped system, the Lagrangian “L” is defined as the difference between kinetic “T” and potential “U” energy: $L = T - U$.

For a dynamic system undergoing a continuously free vibratory motion ($t_1 \leq t \leq t_2$), the equation of motion can be expressed using the Hamilton principle that satisfies the following condition (Formula 1).

For a spherical shape, the kinetic energy is given by Formula 2.

Where h is the thickness of the sphere, ρ is the material density, and (u, v, w) are the deformation of the sphere in spherical coordinates. Based on this model, Wilkinson^[14] established, for a thin spherical shell, a cubic polynomial in λ^2 (frequency parameter) whose solution expresses the vibration modes governing the spherical axisymmetric vibration (without torsion): $\alpha\lambda^6 - \beta\lambda^6 + \beta\lambda^6 - \lambda = 0$. Where α , β and δ are the dimensional characteristics of the sphere.

The solution of the polynomial of Eq. 4 governs the motion of the spherical structure and can be expressed analytically by the “axisymmetric fundamental resonance mode” which is given by Formula 3, and provides the natural radial frequencies of both the breathing and n th mode of closed spherical shells.

Where R is the radius of the mid-surface of the spherical shell, ρ is the density, E is Young’s modulus, ν is Poisson’s ratio, n is the mode number, and λ_n is a frequency parameter for the vibration mode n given by Formula 4.

Figure 2A shows the natural frequencies of the membrane modes with the following properties: Elastic modulus $E = 3300$ Mpa, mass density $\rho = 1190$ kg/m³, Poisson’s ratio $\nu = 0.39$, radius $R = 6.7$ mm, and thickness $h = 2.6$ mm.

For each value of $n \geq 1$, there are three distinct frequencies (three branches or three mode shapes), but only two branches are presented in this part of the study. These two lower and upper branches correspond to the membrane and bending modes, respectively. The mode associated with $n = 0$ on the membrane branch is called the “fundamental mode”, a pure breathing (elongation) mode of the spherical shell. The results are in good agreement with those of Soedel^[17] and Husson^[18] and those given by applying the modal analysis to determine the first resonance frequency of the sensor

$$\delta \int_{t_1}^{t_2} L dt = \delta \int_{t_1}^{t_2} (T - U) dt = 0$$

$$T = \frac{1}{2} \rho h \iint [u^2 + v^2 + w^2] R^2 \sin \varphi \, d\varphi d\theta$$

$$f_n = \frac{\lambda_n}{2\pi R} \left[\frac{E}{\rho(1 - \nu^2)} \right]^{1/2}$$

$$f_n = \frac{\lambda_n}{2\pi R} \left[\frac{E}{\rho(1 - \nu^2)} \right]^{1/2}$$

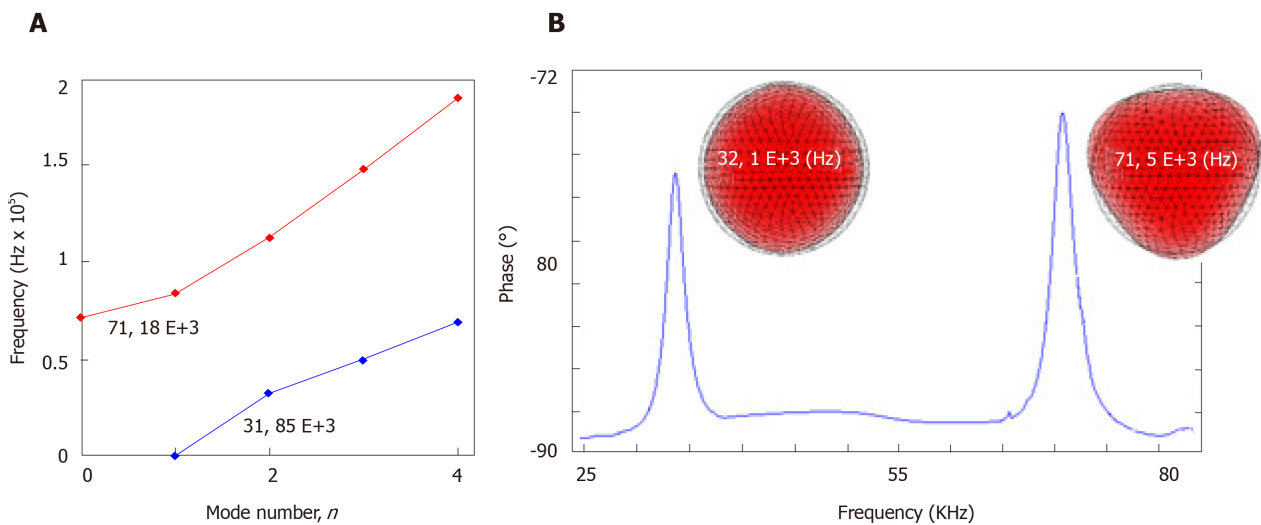


Figure 2 Natural frequencies of torsionless modes for the sensor and frequency response mode of impedance measurement and finite element analysis. A: Natural frequencies of torsionless modes; B: Frequency response mode of impedance measurement and finite element analysis.

considered (Figure 2B).

Physical concept

Embedded electrical scheduling unit: An electronic module is inserted into the hollow part of the sphere (Figure 3) to ensure the following tasks of the sensor simultaneously: (1) Structure resonance; (2) Emission-reception control; (3) Encoding algorithm; and (4) Signal processing and data storage.

The electronics are integrated into a chip system that includes a central processing unit (CPU), a digital oscillator (DCO), a task scheduler (IT), a coded ultrasonic generator (PWMG), a power management unit (PMU), an output amplifier (OB), and an accumulator (BAT).

The device was made from a SoC of the MSP430 family from “Texas Instruments”. The MSP430F2012 was chosen for its small size and minimal hardware resources.

The DCO produces three clock sources: A low-frequency clock (TB) set to 12 kHz to produce a stable time base for the task scheduler (IT), a high-frequency clock (MCLK) set to 16 MHz for timing the CPU, and an average frequency clock (USCLK) set to 32 kHz, which is the frequency of the vibrations emitted by the capsule.

At regular intervals (60 ms), the task scheduler (IT) sends an interrupted signal (INT) to the CPU that produces a sequence of width-modulated bit pulses (CP). This bit sequence is both the interrogation signal and the medium identifier of the device. This sequence is modulated by the all or nothing width modulation generator (PWMG) based on the carrier frequency (USCLK). These coded pulses are amplified by the output amplifier (OB) before being applied to the piezoelectric element. A 3V accumulator (BAT) powers the unit. A PMU provides an economical supply for the various elements of the chain to ensure minimum energy consumption and maximum autonomy of the device.

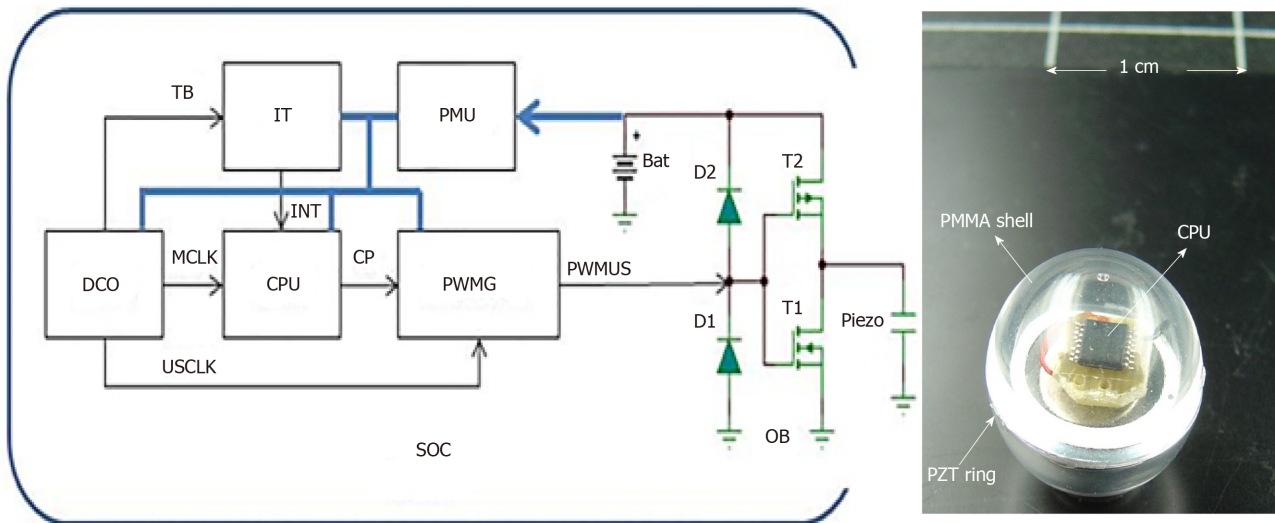


Figure 3 Architecture of the real-time electrical control system embedded in the physical concept (ultrasonic capsule). DCO: A digital oscillator; CPU: Central processing unit; PMU: Power management unit; PWMG: A coded ultrasonic generator; IT: A task scheduler; OB: An output amplifier.

Autonomies and energy balance: One of the goals was to design a sensor with a broad operating range that could be injected into a process (mixer, tank, *etc.*) for monitoring purposes, so we carried out measurements on power consumption during active sensor emissions. Electrical consumption was determined using a 10-Ohm shunt placed in series in the battery. The battery voltage and the voltage across the shunt were measured using differential isolation amplifiers. Both signals were recorded on a digital oscilloscope (Figure 4), which was also used to calculate the instantaneous power consumption of the device.

Outside the frame of bits, the consumption was insignificant except for the low-frequency clock (TB) and the task scheduler (IT). The CPU, PWMG generator, output amplifier, and other clocks were stopped.

For the transmission of the frame of bits, all the elements were “in operation” and the consumption was maximal. This consumption is due mainly to the central unit that works even during the spaces between bits as these spaces are managed by software. Minor overconsumption occurs when the PWMG generator is turned on transmitting a 0 or 1 level, but this consumption is marginal.

Based on different recordings, we can see that the average consumption of the system for a bit frame is relatively independent of the code transmitted: $I_{\text{frame}} \approx 4.5$ mA.

The average current consumed over a time frame $T_{\text{frame}} = 15$ ms repeated periodically every $T = 1.5$ s is then Formula 5.

Another possibility could be a more sophisticated IT task management scheduler that can turn the system unit “off” during these spaces. In this case, the emission of code 15 (1111 and maximum power requirement) would produce an average current drain between two frames (Formula 6).

Thin layer concentric ring receiver sensor

The usual ultrasonic concept is generally based on the use of a resonant piezoelectric transducer vibrating in thickness mode. As the resonant frequency of a transducer is inversely proportional to its size, it becomes greater and greater for low frequencies around 100 kHz.

Our aim was to obtain miniaturized low-frequency acoustic broadband receivers with a frequency component of the same order as the resonance frequency of the capsule. To do this, a different procedure from the classic sensor design was used. The new technique was based on the principle of setting in resonance small, thin concentric rings (Figure 5).

To validate the approach, the mechanical behavior (Figure 6) was assessed and the study was completed with a numerical step using the finite elements method to characterize the resonator vibration modes and visualize the corresponding distortions when the structure was excited. The concordance enabled the use of the experimental device to receive waves coupled with the body or tissues.

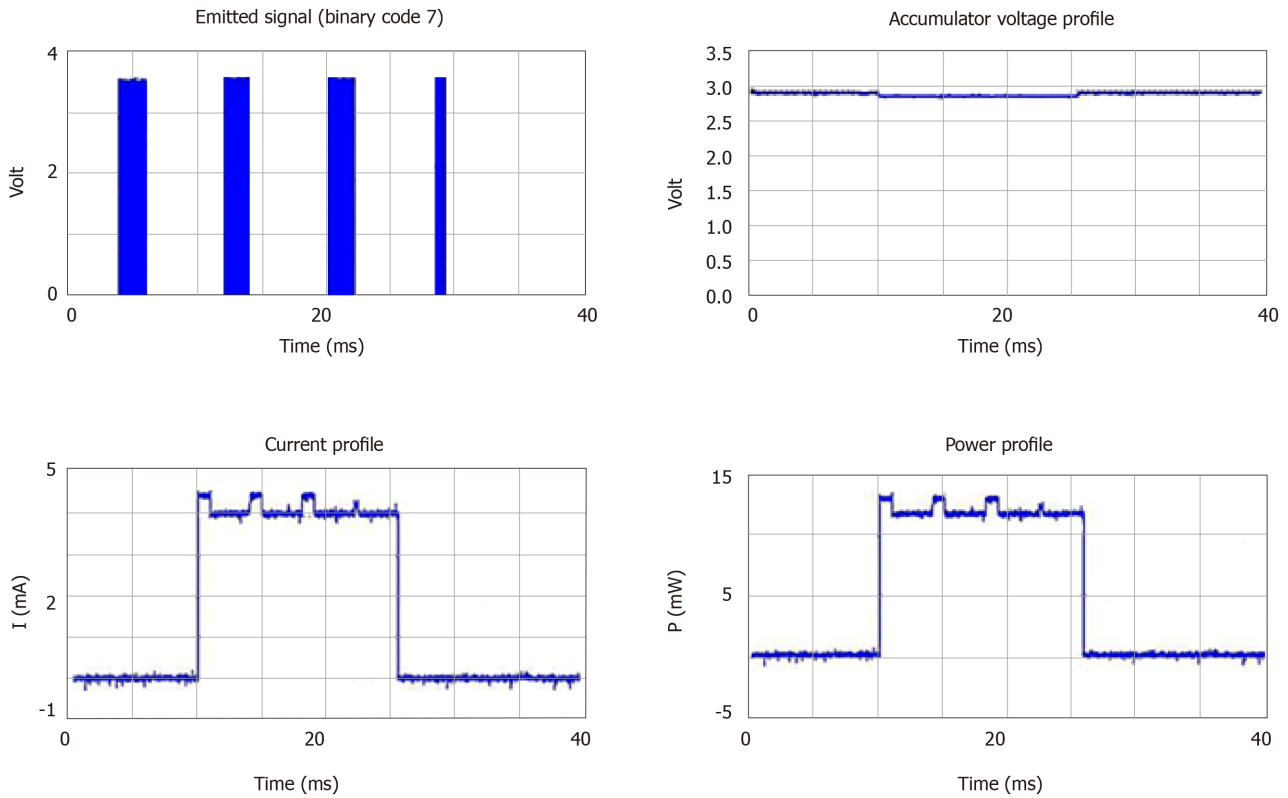


Figure 4 Power consumption during a 0111 frame emission (code 7).

$$I_{\text{average}} = \frac{I_{\text{frame}} \times T_{\text{frame}}}{T} \cong \frac{4.5 \text{ mA} \times 15 \times 10^{-2}}{1.5 \text{ s}} = 0.045 \text{ mA}$$

$$I_{\text{average}} = \frac{I_{\text{frame}} \times T_{\text{frame}}}{T} \cong \frac{4.8 \text{ mA} \times (4 \times 2 \text{ ms})}{1.5 \text{ s}} = 0.026 \text{ mA}$$

From a mechanical point of view, eigenvalues of following equation express the dynamics frequencies of the system: $-\omega^6 + 15.107j\omega^5 + 4.1015\omega^4 - 33.1020j\omega^3 + 1.1027\omega^2 + 2.1032j\omega + 25.1036 = 0$. So, $f_0 = 35 \text{ KHz}$, $f_1 = 56 \text{ KHz}$ and $f_2 = 5.25 \text{ MHz}$. Numerical values: $k = 18.104 \text{ N/m}$, $c = 0.5$, $m_1 = 4835.10^{-6} \text{ kg}$, $m_2 = 1088.10^{-8} \text{ kg}$, $m_3 = 1813.10^{-8} \text{ kg}$.

The physical concept of the micro-receiver is elaborated on the basis of a piezoelectric disk of diameter at the base 10 mm and thickness of 0.25 mm. The central concentric rings are made through an assisted laser engraving system. Other than the physical maintenance of the rings, the central rod allows both electrical polarization and electrical continuity with the central control unit (Figure 5).

RESULTS

Metrological approach

System stability: Before using the composite sensor to characterize a medium reflecting real biological tissues, its performance was validated in a medium with well-known, stable physical properties. For this purpose, we used water as a coupling medium.

At a frequency of 32 kHz, the first mode of vibration emitted by the spherical structure produced the echo diagram presented in Figure 7.

Based on the resonance frequency mode, the experiment was conducted in thermostated water ($25 \text{ }^\circ\text{C} \pm 0.3 \text{ }^\circ\text{C}$) in which a network of resonators (one transmitter and some receivers) was placed.

Knowing in-situ information about the state of *in-vivo* tissues requires the instantaneous position of the receivers to be known. The spatial identification of the

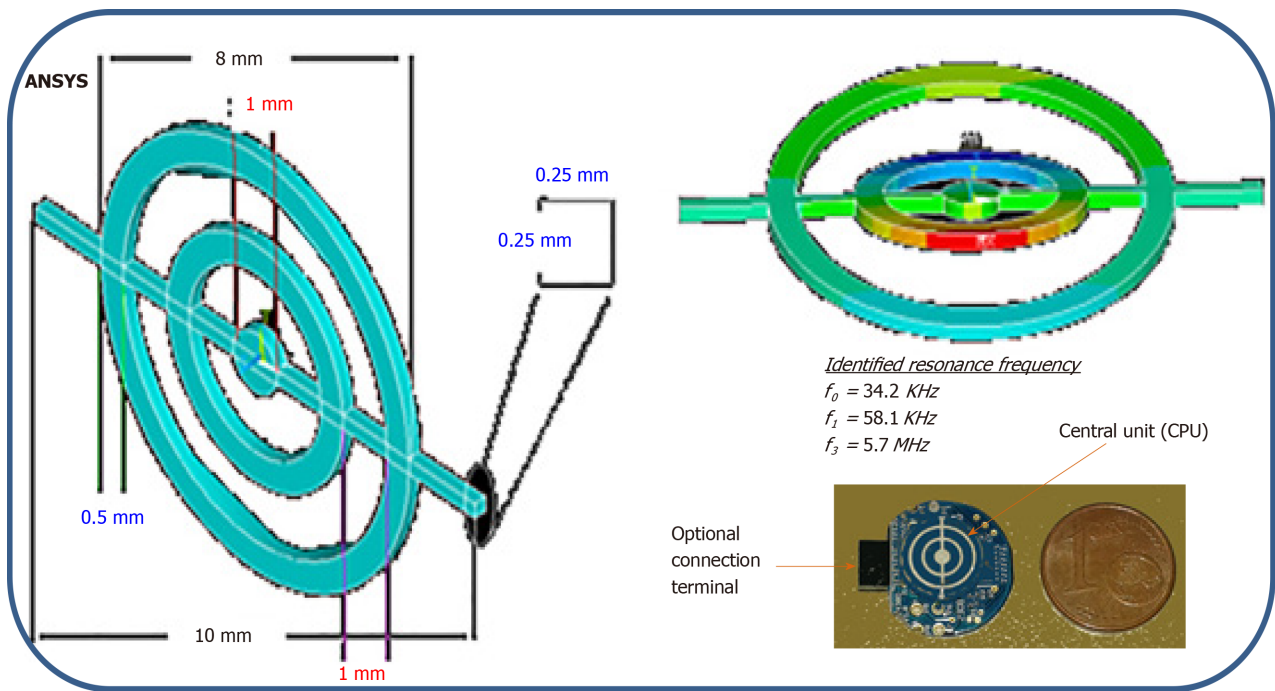


Figure 5 Numerical and physical concept of a micro acoustic sensor based on the use of the vibrational motion of a resonator comprised of concentric rings.

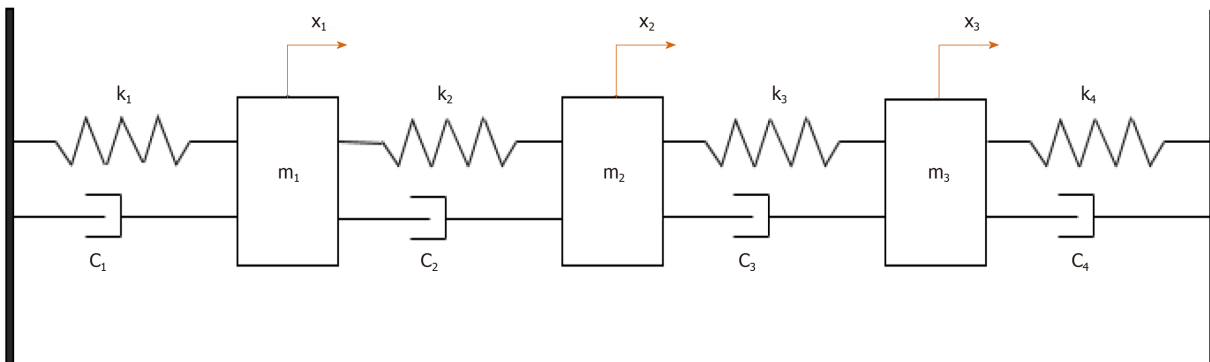


Figure 6 Mechanical equivalent of the micro acoustic sensor consisting of an assembly of masses (x_i) interposed between systems of springs (k_i) and dampers (C_i). k and c reflect the spring and dashpot characteristics.

transmitter at all times gives access to the history of the latter and consequently provides access to the desired physical state or properties of the environment.

The principle of trilateration makes it possible to know the distance between the transmitter and a given receiver by instantaneously locating the source in motion and consequently determining the relative position of the transmitter with respect to a reference point. Measurements are made by exploiting the relative time of flight of the wave (using zero-crossing protocol) between the mobile transmitter and each receiver in the space considered.

These transducers were coupled to the medium to be characterized and totally submerged. The emitter plays the role of a point source; this phenomenon generates a divergent ultrasonic wave, part of which was measured by receivers located at a regular distance from the transmitter. Figure 8 shows a schematic diagram of the measuring system and the stability plot of the variation in the compressional wave velocity measured at different reception points in the given space. A velocity of around 1545 ± 7 m/s in the Agar used as a coupling medium at 25°C is always linked to a longitudinal vibration mode.

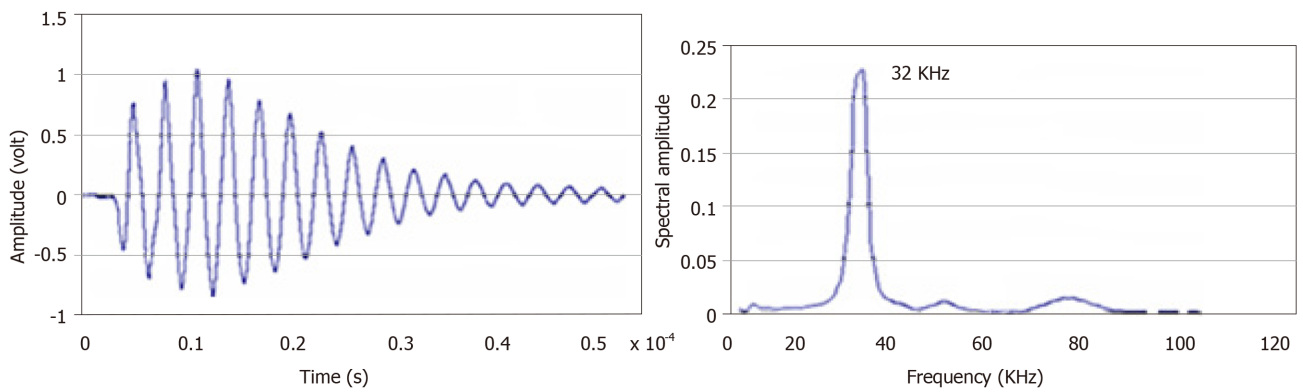


Figure 7 Time and frequency response of the sensor resulting from a short electrical pulse.

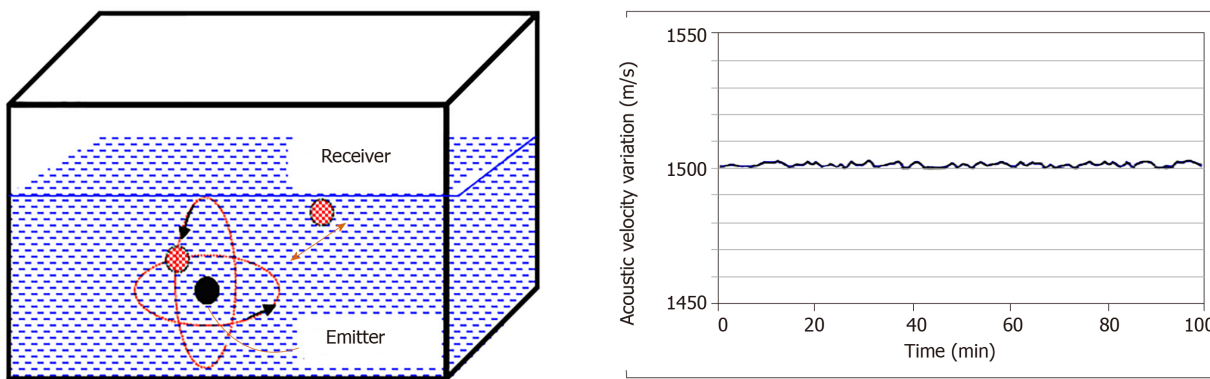


Figure 8 Schematic illustration of the metrological calibration of the capsule.

In-situ applications

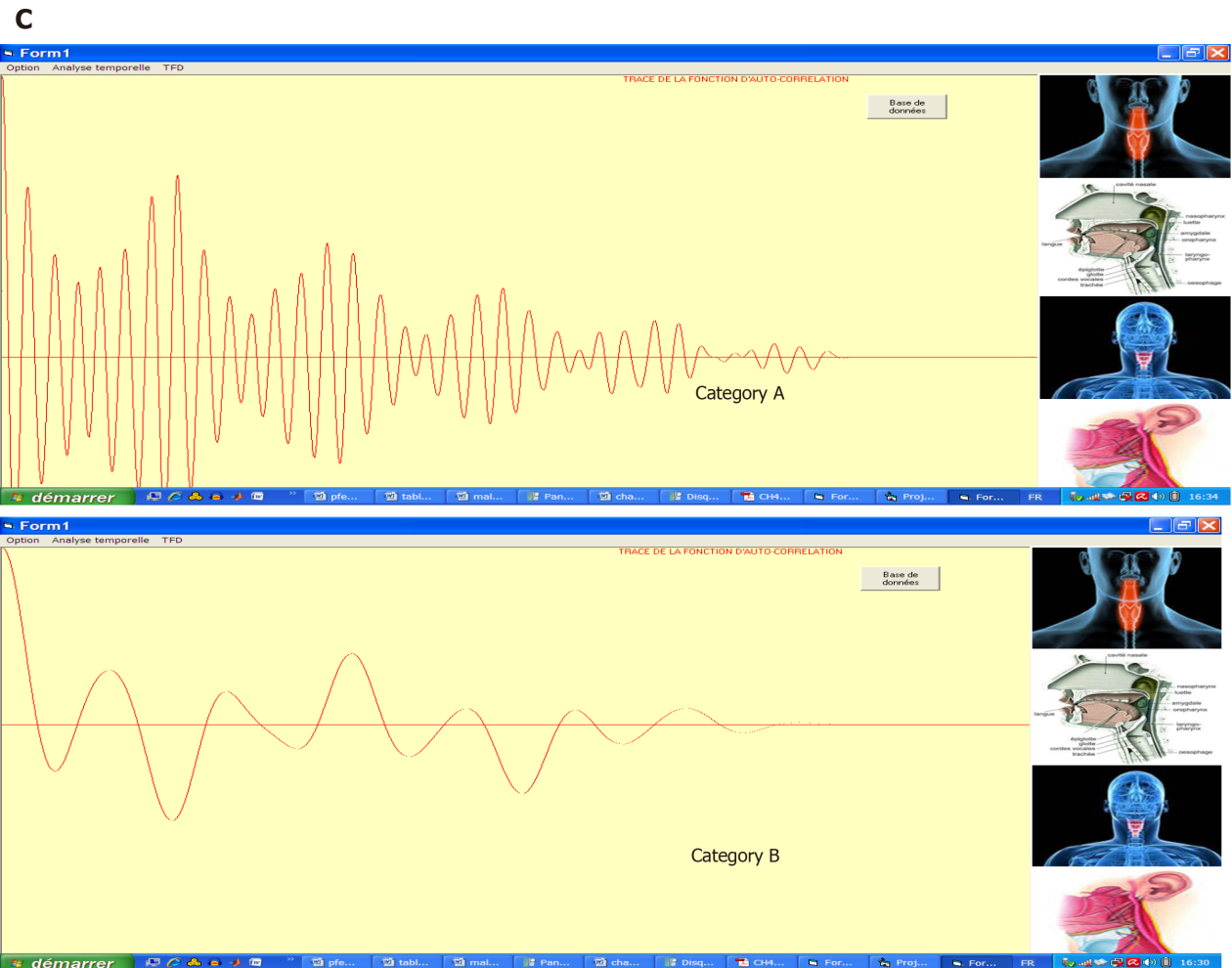
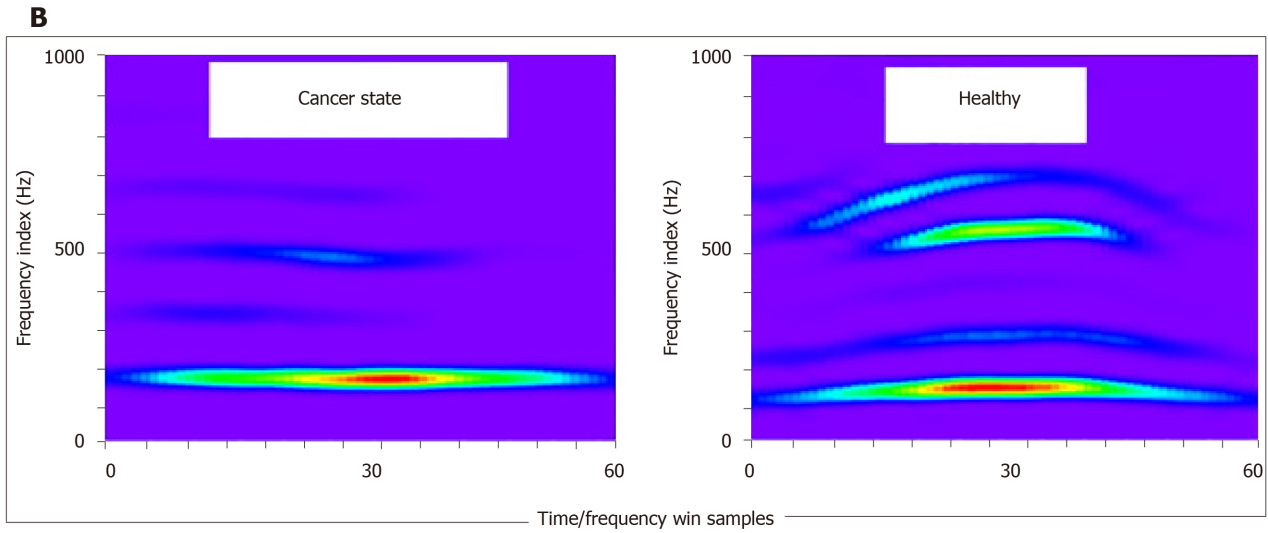
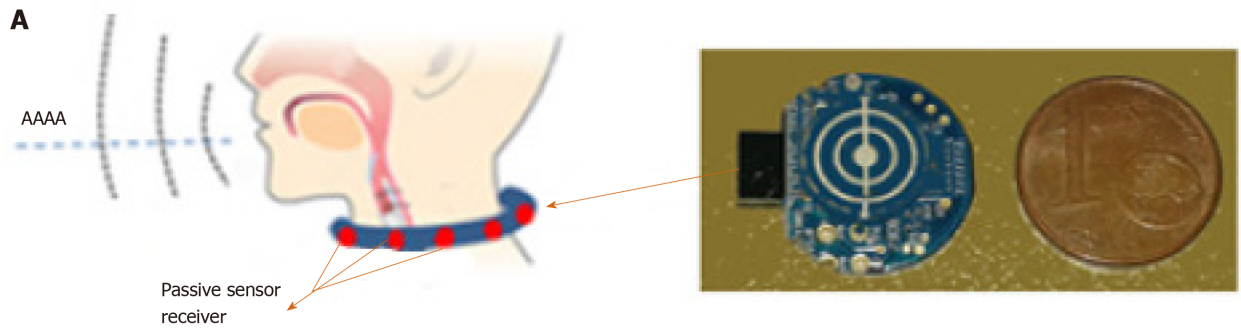
To validate this concept experimentally, we proceeded by two approaches in order to show the field of application and the potential of such system in medical domain. (1) Passive listening approach using concentric micro-sensors for the pathophysiological prevention of the respiratory and vocal apparatus; and (2) Coupling approach (by transmission mode) Capsule/ μ -Resonators to estimate the bio-physical evolution properties of multilayers biological tissues resulting from environmental aggression (electromagnetic waves radiation, stress, *etc.*).

Passive listening approach: This part of study aims to evaluate some larynx physical properties variation through a non-intrusive passive smart listening collar (Figure 9A). The vibratory signal was acquired after each person pronounced the vowel / a /, which reflects the greatest number of vocal cord vibrations modes^[19,20]. The latter can provide systematic and *in-vivo* screening for some laryngeal diseases, including laryngeal cancer, by spectro-temporal analysis of the voice signal resonance. This would allow consequently the detection of these diseases at an early stage, even in people who still represent no symptoms, which would permit an early treatment and a higher chance of cure.

For that, micro resonators collar is implemented and is used to carry a detailed examination on four different categories of people: Healthy cases, subjects with laryngeal cancer, those suffering from inflammatory polypus, and the ones having chronic laryngitis. Figure 9B shows the spectrograms of the two extreme physiological cases: A healthy state versus a cancerous one. In our application, one hundred patients with an average age of 53 years of whom 20% were women were diagnosed in the same context but separately.

Figure 9C gives an idea about the display of data and the classification of categories in a real environment. It shows an example of the graphical interface implemented providing the time signature of the signals for each of the above-mentioned patient categories:

The ENT examination shows that in a healthy subject the laryngeal pathway is normal with good mobility of the vocal cords (A). The autocorrelation function (of the



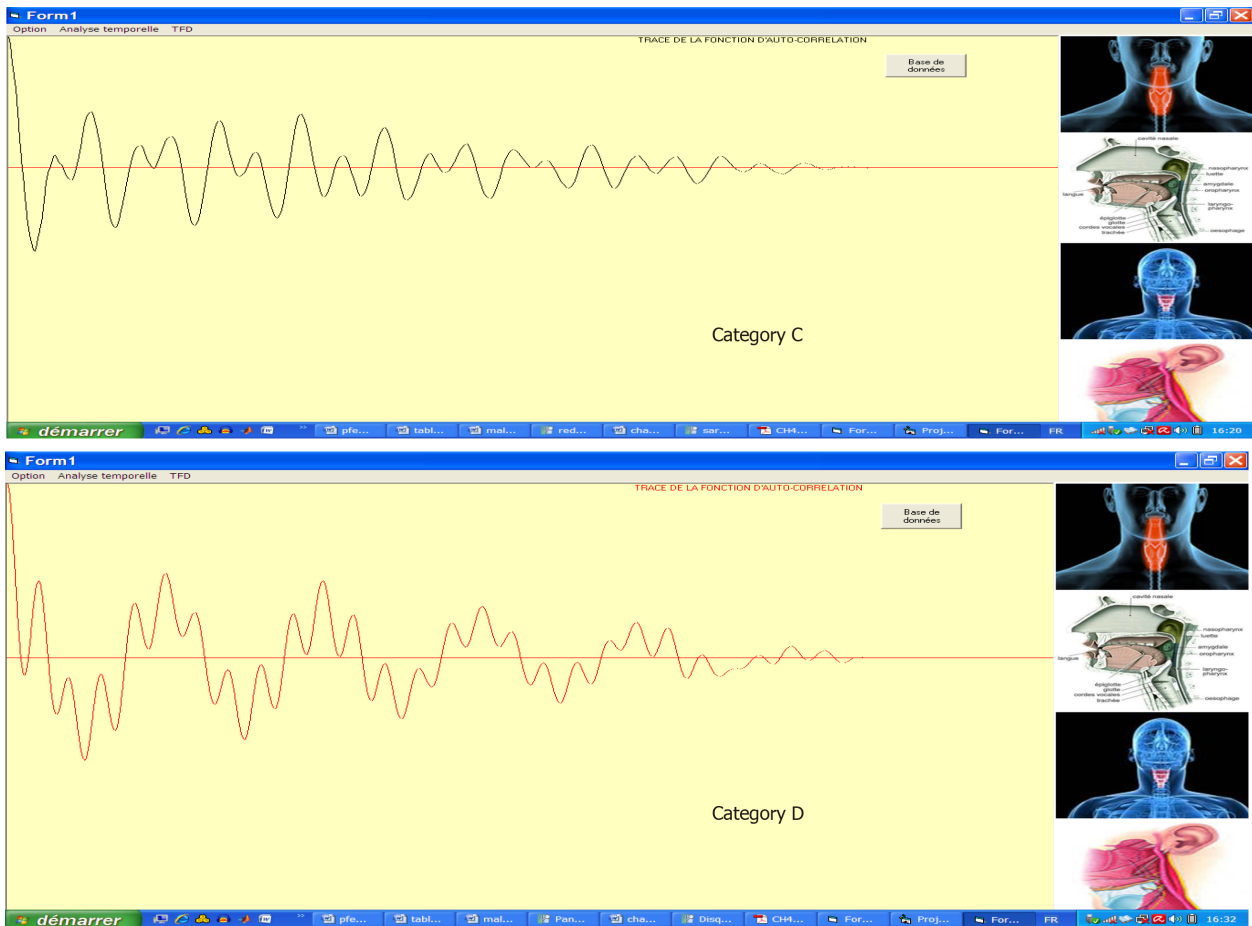


Figure 9 Passive listening approach. A: Physical concept of the micro-resonator acoustic prevention system; B: Spectrograms showing the different frequency components weights for two extreme physiological states: a healthy case and a cancerous state; C: Graphical interface of connected system showing the morphological diagram of signal issued from each category.

time signal) is a sin function; it is maximal at the intercept and contains several secondary periodic lobes resulting from the periodicity of the vibration of the vocal cords.

For a person with cancer (B), the temporal plot is irregular (random) and the spectrum is limited to low frequencies due to a significant decrease in and even total absence of vibration of the vocal cords.

As for subjects with inflammatory polyps or chronic laryngitis (C and D), the temporal plot contains some irregularities but also shows some similarities with the temporal plot of healthy patients. Additionally, the spectrum contains high frequencies but with lower values than healthy subjects.

Coupling capsule/ μ -resonators approach: This approach was carried out on the variation of the wave properties such as velocity and energy absorption of the acoustic wave at reception. Reason of ethical consideration, the parameters were measured through a composite medium made from biological tissues of animal origin embedded in a coupling medium, in this case, "Agar" (Figure 10).

To measure the evolution over time of the physical state of the biological tissues, we considered four samples of animal origin placed at equal distance (10 cm) from the diagonal crossing where the transmitter was located. The samples were embedded in the agar.

The receivers (R_i ; $i = 1, 2, 3, 4$) in the measurement space, close to the samples, were distributed as follows: R1 - Skin sample 3 mm thick; R2 - Composite sample; skin + muscle (3 mm + 7 mm); R3 - Muscle sample 10 mm thick; and R4 - Reference point (coupling without tissue).

Table 1 summarizes the averages of the physical properties of the different samples. These values were considered as starting values at time (t_0) in the measurement process based on the "LabView" acquisition system.

Given the dependence of the ultrasonic velocities on the physical properties of the samples (e.g., compression and shear modulus), the curves on Figure 11 shows the

Table 1 Averages of the physical properties of the different samples

	Agar (0.5%)	Skin	Muscle
E	25 kPa	30 MPa	480 MPa
G	148 kPa	0.58 MPa	0.14 MPa
kg/m ³	□ 1	1.3	1.57
	0.5	0.3	0.31



Figure 10 Illustration of the measurement cell showing the spatial distribution of the emitter capsule embedded in the volume of agar at controlled distance of the different bio-tissue samples equipped with micro-resonators receivers.

decrease in the compression elastic and shear modulus (E and G) of the samples over time under the effect of aging (applied as physical stress).

E and G were measured every two days over a period of 10 d (D) starting from the time of origin t_0 at 25°C.

As the agar is primarily a water incompressible fluid, its Poisson's ratio is near 0.50 and slight deviations do not significantly affect the results.

To consolidate this variation, the ultrasonic quantification based on matrix stiffness formalism^[21] was reported for each measurement showing the response of each layer and the multilayers taking into account the effects of the interfaces and boundary conditions between the layers (agar-muscle-epidermis). Indeed, the multi-layered structure being merged into a single layer, the reflection and transmission coefficients were calculated considering that the whole structure is bounded by fluids. Then, a back-recursive algorithm was applied to compute the displacement vectors amplitudes in each layer, which allows the calculation of acoustic field in every layer based on the angular spectrum approach.

DISCUSSION

The study and design of an autonomous embedded ultrasonic system able to meet a medical need was the main objective of this work. We have proposed a concept of measuring elements based on miniaturized spherical capsule sensors coupled with concentric ring receivers.

A detailed description of the proposed resonator and its vibratory mechanical behavior has been consolidated with a mechanical approach and a numerical approach using finite element analysis.

The physical implementation of the capsule led us to an autonomous vibratory element. The power analysis (impedance and phase) of the overall structure showed very good agreement between the numerical and analytical results.

However, the analysis of the effect of aging factors of tissues on the variation of the acoustic properties gave a coherent view of the mechanical behavior of both the

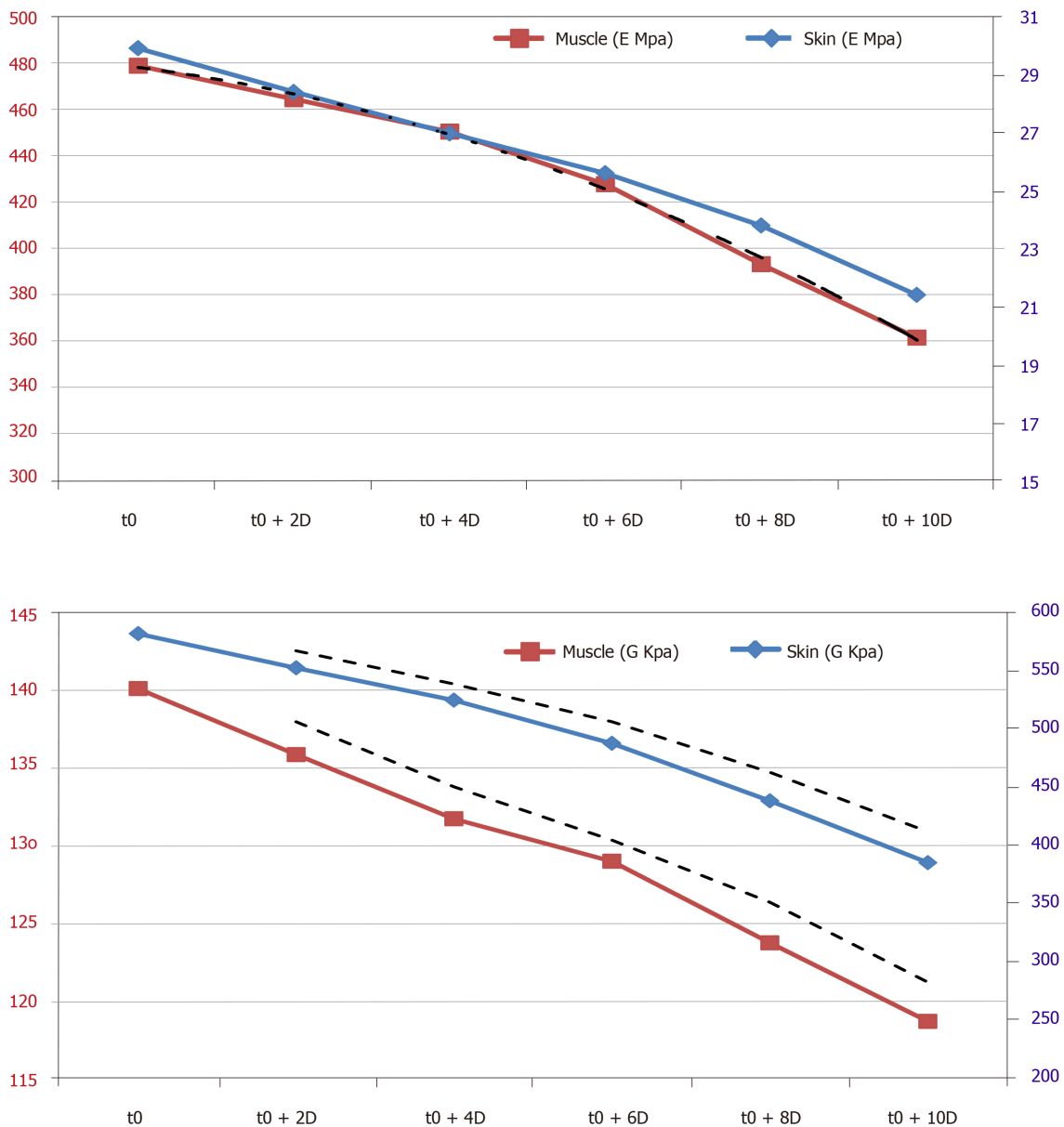


Figure 11 Curves showing the evolution of the stress and shear components measured by the experimental approach and compared to the calculated displacement-stress vector (dashed lines) for an incident plane wave in the three-layer medium (agar, skin and muscle).

measuring system and the dynamic medium considered. The curves show all the critical phases in a complex evolutionary environment, knowing that there are few techniques, which, under similar conditions, give access to the local physical properties sought.

As a result, this work presents a "soft" and reliable diagnostic system based on the vibratory mechanical behavior of the vocal apparatus. A double interest results in the prospects of such application.

Clinically, this system has been studied and designed to implement an alternative screening method for laryngeal pathologies to save patients from frequent exposure to harmful radiation as RX, MRI, *etc.*

In terms of prevention, the connected feature of this system offers a means of continuous information on the evolution of a state of health, continuously viewable by a "smart phone" interface, which could lead to a possible early detection of severe laryngeal diseases, especially cancer, giving the subject a higher chance of cure.

ARTICLE HIGHLIGHTS

Research background

Studying interactions between acoustic and living fields goes far beyond biological and health impact studies.

Research motivation

The present manuscript is one of the first reports on a potentially connected "real-time" diagnostic technique, optimizing interactions between acoustic and live fields, providing an autonomous information system capable of collecting data on physiological variations using a soft vibratory wave.

Research objectives

The objective of this work was partly to contribute to the development of innovative radiating structures close to the body (sensors radiating inside the body and through multilayer tissues).

Research methods

A low-frequency ultrasonic method based on the use of an innovative autonomous ultrasonic capsule as a miniaturized elementary spherical sensor and micro-rings resonators were examined.

Research results

Other their functions as passive listeners for the prevention and diagnosis in physiopathology of the respiratory and laryngeal apparatus, these micro-resonators coupled to the ultrasonic capsule through biological tissues are capable of evaluating the effects of aggression of the environment on human metabolism.

Research conclusions

This work presents a "soft" and reliable diagnostic system based on the vibratory mechanical behavior of the vocal apparatus. A double interest results in the prospects of such application.

REFERENCES

- 1 **Lay HS**, Cox BF, Seetohul V, Demore CEM, Cochran S. Design and Simulation of a Ring-Shaped Linear Array for Microultrasound Capsule Endoscopy. *IEEE Trans Ultrason Ferroelectr Freq Control* 2018; **65**: 589-599 [PMID: 29610089 DOI: 10.1109/TUFFC.2018.2794220]
- 2 **Peng C**, Sun T, Vykhodtseva N, Power C, Zhang Y, Medannold N, Porter T. Intracranial Non-thermal Ablation Mediated by Transcranial Focused Ultrasound and Phase-Shift Nanoemulsions. *Ultrasound Med Biol* 2019; **45**: 2104-2117 [PMID: 31101446 DOI: 10.1016/j.ultrasmedbio.2019.04.010]
- 3 **He H**, Stylogiannis A, Afshari P, Wiedemann T, Steiger K, Buehler A, Zakian C, Ntziachristos V. Capsule optoacoustic endoscopy for esophageal imaging. *J Biophotonics* 2019; **12**: e201800439 [PMID: 31034135 DOI: 10.1002/jbio.201800439]
- 4 **de Groen P**. From propofol to midazolam/fentanyl to nosedation during colonoscopy: can the propofol trend be reversed? *Gastrointest Endosc* 2018; **87**: AB149 [DOI: 10.1016/j.gie.2018.04.1378]
- 5 **Diab D**, Lefebvre F, Nassar G, Smagin N, Isber S, El Omar F, Naja A. An autonomous low-power management system for energy harvesting from a miniaturized spherical piezoelectric transducer. *Rev Sci Instrum* 2019; **90**: 075004 [PMID: 31370448 DOI: 10.1063/1.5084267]
- 6 **Wang J**, Memon F, Touma G, Baltsavias S, Jang JH, Chang C, Rasmussen MF, Olcott E, Jeffrey RB, Arbabian A, Khuri-Yakub BT. Capsule Ultrasound Device: Characterization and Testing Results. 2017 IEEE International Ultrasonics Symposium (IUS); 2017 Sep 6-9; Washington, USA. IEEE, 2017: 1-4 [DOI: 10.1109/ULTSYM.2017.8092071]
- 7 **Memon F**, Touma G, Wang J, Baltsavias S, Moini A, Chang C, Rasmussen MF, Nikoozadeh A, Choe JW, Olcott E, Jeffrey RB, Arbabian A, Khuri-Yakub BT. Capsule Ultrasound Device: Further Developments. 2016 IEEE International Ultrasonics Symposium (IUS); 2016 Sep 18-21; Tours, France. IEEE, 2016: 1-4 [DOI: 10.1109/ULTSYM.2016.7728851]
- 8 **Cox BF**, Stewart F, Lay H, Cummins G, Newton IP, Desmulliez MPY, Steele RJC, Nätke I, Cochran S. Ultrasound capsule endoscopy: sounding out the future. *Ann Transl Med* 2017; **5**: 201 [PMID: 28567381 DOI: 10.21037/atm.2017.04.21]
- 9 **Walker AJ**. A theoretical model of an ultrasonic transducer incorporating spherical resonators. *IMA J Appl Math* 2016; **81**: 1-25 [DOI: 10.1093/imamat/hxv023]
- 10 **Nasedkin K**, Rybyanets A. Finite element analysis of ultrasonic spherical piezoelectric phased array with split electrodes. 2016 Joint IEEE International Symposium on the Applications of Ferroelectrics, European Conference on Application of Polar Dielectrics, and Piezoelectric Force Microscopy Workshop (ISAF/ECAPD/PFM); 2016 Aug 21-25; Darmstadt, Germany. IEEE, 2016 [DOI: 10.1109/ISAF/ECAPD/PFM.2016.7728851]

- 10.1109/ISAF.2016.7578074]
- 11 **Mehl JB**, Moldover MR. Precision acoustic measurements with a spherical resonator: Ar and C2H4. *J Chem Phys* 1981; **74**: 4062-4077 [DOI: [10.1063/1.441587](https://doi.org/10.1063/1.441587)]
 - 12 **He MG**, Liu ZG, Yin JM. Measurement of speed of sound with a spherical resonator: HCFC-22, HFC-152a, HFC-143a, and Propane. *Int J Thermophys* 2002; **23**: 1599-1615 [DOI: [10.1023/A:1020742018220](https://doi.org/10.1023/A:1020742018220)]
 - 13 **Baker WE**. Axisymmetric Modes of Vibration of Thin Spherical Shell. *J Acoust Soc Am* 1961; **33**: 1749 [DOI: [10.1121/1.1908562](https://doi.org/10.1121/1.1908562)]
 - 14 **Wilkinson JP**. Natural Frequencies of Closed Spherical Shells. *J Acoust Soc Am* 1965; **38**: 367-368 [DOI: [10.1121/1.1909687](https://doi.org/10.1121/1.1909687)]
 - 15 **Kalnins A**. Effect of Bending on Vibrations of Spherical Shells. *J Acoust Soc Am* 1964; **36**: 74-81 [DOI: [10.1121/1.1918916](https://doi.org/10.1121/1.1918916)]
 - 16 **Duffey TA**, Romero C. Strain growth in spherical explosive chambers subjected to internal blast loading. *Int J Impact Eng* 2003; **28**: 967-983 [DOI: [10.1016/S0734-743X\(02\)00169-0](https://doi.org/10.1016/S0734-743X(02)00169-0)]
 - 17 **Soedel W**. Vibrations of Shells and Plates (Mechanical Engineering). 3rd Edition. Boca Raton: CRC Press, 2004 [DOI: [10.4324/9780203026304](https://doi.org/10.4324/9780203026304)]
 - 18 **Husson D**. A perturbation theory for the acoustoelastic effect of surface waves. *J Appl Phys* 1985; **57**: 1562 [DOI: [10.1063/1.334471](https://doi.org/10.1063/1.334471)]
 - 19 **Story H**. An overview of the physiology, physics and modeling of the sound source for vowels. *Acoust Sci Technol* 2002; **23**: 195 [DOI: [10.1250/ast.23.195](https://doi.org/10.1250/ast.23.195)]
 - 20 **Gramming P**. Vocal loudness and frequency capabilities of the voice. *J Voice* 1991; **5**: 144 [DOI: [10.1016/S0892-1997\(05\)80178-X](https://doi.org/10.1016/S0892-1997(05)80178-X)]
 - 21 **Matta S**. Acoustic wave propagation in a multilayer composed of fluid, solid, and porous viscoelastic layers. PhD Thesis, Université de Valenciennes et du Hainaut-Cambresis. 2018. Available from: <https://hal.inria.fr/tel-02398764/>



Cerebral amyloid angiopathy vs Alzheimer's dementia: Diagnostic conundrum

Jamie Arberry, Sarneet Singh, Ruth Akiyo Mizoguchi

ORCID number: Jamie Arberry 0000-0001-9485-5576; Sarneet Singh 0000-0003-1279-4760; Ruth Akiyo Mizoguchi 0000-0001-8938-5477.

Author contributions: Arberry J and Mizoguchi RA were the patient's physicians, Arberry J and Singh S reviewed the literature and drafted the manuscript; all authors were responsible for the revision of the manuscript and issued final approval for the version to be submitted.

Informed consent statement:

Informed written consent was obtained from the patient.

Conflict-of-interest statement: No conflict of interest.

CARE Checklist (2016) statement:

The authors have read the CARE Checklist (2016), and the manuscript was prepared and revised according to the CARE Checklist (2016).

Open-Access: This article is an open-access article that was selected by an in-house editor and fully peer-reviewed by external reviewers. It is distributed in accordance with the Creative Commons Attribution NonCommercial (CC BY-NC 4.0) license, which permits others to distribute, remix, adapt, build upon this work non-commercially,

Jamie Arberry, Sarneet Singh, Ruth Akiyo Mizoguchi, Chelsea and Westminster Hospital, London SW10 9NH, United Kingdom

Corresponding author: Jamie Arberry, BM BCh, Doctor, Chelsea and Westminster Hospital, 369 Fulham Palace Road, London SW10 9NH, United Kingdom. jamie.arberry@doctors.org.uk

Abstract

BACKGROUND

Diagnosis of a dementia subtype can be complex and often requires comprehensive cognitive assessment and dedicated neuroimaging. Clinicians are prone to cognitive biases when reviewing such images. We present a case of cognitive impairment and demonstrate that initial imaging may have resulted in misleading the diagnosis due to such cognitive biases.

CASE SUMMARY

A 76-year-old man with no cognitive impairment presented with acute onset word finding difficulty with unremarkable blood tests and neurological examination. Magnetic resonance imaging (MRI) demonstrated multiple foci of periventricular and subcortical microhaemorrhage, consistent with cerebral amyloid angiopathy (CAA). Cognitive assessment of this patient demonstrated marked impairment mainly in verbal fluency and memory. However, processing speed and executive function are most affected in CAA, whereas episodic memory is relatively preserved, unlike in other causes of cognitive impairment, such as Alzheimer's dementia (AD). This raised the question of an underlying diagnosis of dementia. Repeat MRI with dedicated coronal views demonstrated mesial temporal lobe atrophy which is consistent with AD.

CONCLUSION

MRI brain can occasionally result in diagnostic overshadowing, and the application of artificial intelligence to medical imaging may overcome such cognitive biases.

Key words: Alzheimer's dementia; Cerebral amyloid angiopathy; Cognitive impairment; Microhaemorrhages; Artificial intelligence; Case report

©The Author(s) 2020. Published by Baishideng Publishing Group Inc. All rights reserved.

and license their derivative works on different terms, provided the original work is properly cited and the use is non-commercial. See: <http://creativecommons.org/licenses/by-nc/4.0/>

Manuscript source: Invited manuscript

Received: March 17, 2020

Peer-review started: March 17, 2020

First decision: June 5, 2020

Revised: June 15, 2020

Accepted: June 18, 2020

Article in press: June 18, 2020

Published online: June 28, 2020

P-Reviewer: Chen TL, Nassar G

S-Editor: Wang JL

L-Editor: A

E-Editor: Ma YJ



Core tip: This case represents the complexities of diagnosing dementia subtypes with an unusual presentation for what is likely Alzheimer's dementia, rather than cerebral amyloid angiopathy as per initial magnetic resonance imaging brain. In such cases, imaging can potentially influence the diagnostic accuracy, which might ultimately result in misdiagnosis and hence alter the management plan. We argue that artificial intelligence and image automation could avoid such diagnostic oversights.

Citation: Arberry J, Singh S, Mizoguchi RA. Cerebral amyloid angiopathy vs Alzheimer's dementia: Diagnostic conundrum. *Artif Intell Med Imaging* 2020; 1(1): 65-69

URL: <https://www.wjgnet.com/2644-3260/full/v1/i1/65.htm>

DOI: <https://dx.doi.org/10.35711/aimi.v1.i1.65>

INTRODUCTION

Cerebral β -amyloid angiopathy (CAA) occurs when β -amyloid is deposited in the vascular media and adventitia. It is a common pathology in the brains of older individuals and is known to co-exist with other causes of cognitive decline. CAA has been shown to contribute to changes in early Alzheimer's dementia (AD) pathogenesis^[1,2]; CAA is present in 2%-3% of the AD brains of which half of them have a severe form. Therefore, it is possible that vascular change and neuritic plaque deposition are not just parallel processes but reflect additive pathological cascades.

CAA also predisposes one to cerebral infarction and cerebral haemorrhage, though the clinical effects of CAA in AD are mostly silent, or at least are "masked" by the greater degree of neuronal dysfunction induced by senile plaque formation and neurofibrillary degeneration. However major haemorrhagic episodes can still occur in patients with AD and CAA appears to be the underlying cause of these.

There can be diagnostic uncertainties in patients with CAA and underlying dementia. In this case report, we discuss an unusual presentation of AD. Through this we aim to emphasise the importance of robust cognitive assessment and dedicated neuroimaging in patients presenting with cognitive impairment, to investigate and consider all causes of dementia, and in order to ensure an accurate diagnosis in such patients.

CASE PRESENTATION

Chief complaints

A 76-year-old man presented to our hospital with acute onset word finding difficulty and "confused" speech.

History of presenting illness

He had returned from work and could not remember the events that followed. A collateral history from his wife reveals that on his return to the house, he was delirious and had difficulty word finding. There was no obvious history of trauma reported.

In the years leading up to this episode, he had small problems remembering complex instructions and would be a little more repetitive.

History of past illness

He had a background of hypertension, hypercholesterolaemia, gout and alcohol excess, with no known cognitive impairment. He had recently had a mesenteric aneurysm repaired. He was a non-smoker.

Social and family history

There was no family history of note. He worked as an advisor on multiple boards and lived with his wife, both fully independent.

Physical examination upon admission

On general examination, there was no evidence of alcohol intoxication or alcohol withdrawal. A Glasgow Coma Scale score, which is used to review levels of consciousness, was 13 (15 is the highest score and the patient scored 2 points less due

to his “confused” speech). An Abbreviated Mental Test Score (AMTS) used to assess cognition at the bedside was low at 2/10 (a score of less than 7 would prompt more sensitive cognitive testing). His neurological examination was intact aside from his speech disturbance: There was evidence of an expressive dysphasia, perseveration and confabulation. As prompted by the low AMTS, further detailed cognitive tests were carried out: (1) Montreal Cognitive Assessment, he scored 10/30 (a score of 26 or over is normal); and (2) Addenbrookes Cognitive Examination 3 (ACE3), he scored 62/100, affecting mainly memory and fluency domains (a score of 88 and above is normal; below 83 is abnormal; and between 83 and 87 is inconclusive).

Laboratory examinations

All initial blood tests including full blood count, renal profile, liver function tests, ammonia, clotting screen, inflammatory markers were normal. Chest X-ray and urinalysis were normal. Electrocardiogram revealed normal sinus rhythm.

Imaging examinations

Both computed tomography (CT) brain and CT angiogram revealed bilateral hygromas without mass effect, but no other abnormality. Diffusion-weighted magnetic resonance imaging (MRI) demonstrated bilateral infarcts, with haemorrhagic transformation. Susceptibility weighted MRI (SWI) demonstrated multiple foci of periventricular and subcortical microhaemorrhages, consistent with CAA.

FINAL DIAGNOSIS

On this presentation, the patient was treated as having CAA due to the MRI changes. Further diagnostic evaluation (see below), later questioned this diagnosis and raised the possibility of AD.

TREATMENT

Given the presence of the haemorrhages on initial imaging, this patient did not receive antiplatelet or anticoagulant therapy. His vascular risk factors were optimised by commencing atorvastatin and amlodipine. He was also commenced on vitamin B and thiamine tablets with his previous medications (lansoprazole, allopurinol, ferrous fumarate). He was discharged with memory clinic follow-up.

OUTCOME AND FOLLOW-UP

Prior to his attendance at the memory clinic, his condition was complicated by another episode of delirium and dysphasia – CT brain on this occasion demonstrated bilateral subdural haematomas, which were operated on the following day.

At the memory clinic, his repeat ACE3 reflected some degree of improvement from 62/100 to 73/100. Despite fluent speech and extensive description of historic events, the main deficits were seen again in the domains of working memory and semantic language function; he only scored 10/26 on memory domain and 5/14 on verbal fluency. This pattern of cognitive decline is consistent with AD, which is contrary to the initial diagnosis of CAA.

DISCUSSION

In this case, we are faced with multiple potential causes of cognitive decline, including AD, CAA^[5,4] and intracerebral haemorrhage^[4]. Gold standard diagnostic testing for AD is still post-mortem assessment of brain tissue, therefore dementia diagnosis is made based upon a combination of history, cognitive assessment and neuroimaging to provide a probable diagnosis.

Our patient demonstrated significant decline in episodic memory and verbal fluency, as per the ACE3. In recent studies^[5,6], CAA has been shown to be associated with deficits in executive function and processing speed, while working memory is usually relatively preserved. Patients with AD demonstrate deficits in all domains,

especially working memory. This suggests that the cognitive impairment here could represent an underlying diagnosis of AD.

Despite this, the initial MRI brain focused significantly on features of CAA rather than mesial temporal lobe (MTL) atrophy, the latter of which correlates more with the findings on cognitive assessment. These features of CAA (microhaemorrhages) are shown more clearly on the SWI (Figure 1A), which is more sensitive at detecting CAA compared with conventional gradient-echo imaging.

Given the diagnostic overshadowing from the CAA, we proceeded to dedicated T1 coronal views of his hippocampi (Figure 1B), which demonstrated MTL atrophy. In this case, the initial MRI may have masked the potential for an alternative diagnosis of the much more likely AD. The next step would be amyloid PET scanning to add more evidence to our final diagnosis of AD.

This case highlights the perils of diagnostic oversight while reviewing imaging, resulting in the potential for misdiagnosis. It is known that the workload of radiologists has massively increased over the past decade^[7], meaning they have less time to review each image. When uncertainty arises, as it did in our case, radiologists are under temporal pressure to commit to a diagnosis using their visual perception. Artificial intelligence (AI) in imaging not only removes this time pressure, but also allows image automation to remove cognitive biases that clinicians might face when reviewing imaging. Deep learning algorithms in AI allow for machines to learn how to review imaging data without the need for pre-defined human input. This increases accuracy and efficiency of image acquisition, providing objective assessment of disease and removing radiologist subjectivity. Such an approach would have assisted in the case here, and indeed would assist in all cases of cognitive impairment, by comparing imaging to a database of other age and sex matched images. Data has already demonstrated the increased sensitivity and specificity of AI techniques in diagnosis of AD with MRI^[8].

CONCLUSION

There are clear diagnostic uncertainties in patients presenting with evidence of cognitive impairment and CAA. CAA has been shown to contribute to changes in early AD pathogenesis, therefore, in order to correctly diagnose the dementia subtype, robust cognitive assessment and dedicated neuroimaging is required to actively search for other causes of cognitive impairment. AI in imaging may offer a step towards accurate diagnosis in such cases using deep learning methods to provide accurate and early diagnosis of dementia subtypes.

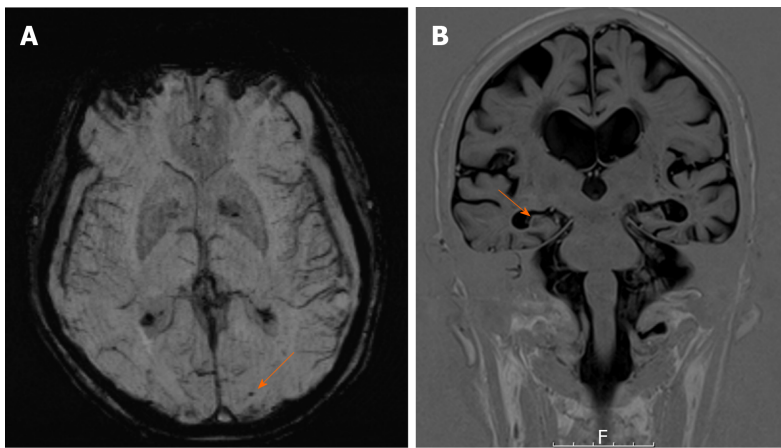


Figure 1 Magnetic resonance imaging of the patient. A: Susceptibility weighted magnetic resonance imaging (MRI) showing left occipital microhaemorrhage (arrow), suggestive of cerebral amyloid angiopathy; B: Coronal view T1-weighted MRI showing bilateral mesial temporal atrophy (arrow).

REFERENCES

- 1 **Vidoni ED**, Yeh HW, Morris JK, Newell KL, Alqahtani A, Burns NC, Burns JM, Billinger SA. Cerebral β -Amyloid Angiopathy Is Associated with Earlier Dementia Onset in Alzheimer's Disease. *Neurodegener Dis* 2016; **16**: 218-224 [PMID: 26756746 DOI: 10.1159/000441919]
- 2 **De Reuck J**. The Impact of Cerebral Amyloid Angiopathy in Various Neurodegenerative Dementia Syndromes: A Neuropathological Study. *Neurol Res Int* 2019; **2019**: 7247325 [PMID: 30792924 DOI: 10.1155/2019/7247325]
- 3 **Boyle PA**, Yu L, Nag S, Leurgans S, Wilson RS, Bennett DA, Schneider JA. Cerebral amyloid angiopathy and cognitive outcomes in community-based older persons. *Neurology* 2015; **85**: 1930-1936 [PMID: 26537052 DOI: 10.1212/WNL.0000000000002175]
- 4 **Banerjee G**, Wilson D, Ambler G, Osei-Bonsu Appiah K, Shakeshaft C, Lunawat S, Cohen H, Yousry T Dr, Lip GYH, Muir KW, Brown MM, Al-Shahi Salman R, Jäger HR, Werring DJ; CROMIS-2 Collaborators. Cognitive Impairment Before Intracerebral Hemorrhage Is Associated With Cerebral Amyloid Angiopathy. *Stroke* 2018; **49**: 40-45 [PMID: 29247143 DOI: 10.1161/STROKEAHA.117.019409]
- 5 **Case NF**, Charlton A, Zwiers A, Batool S, McCreary CR, Hogan DB, Ismail Z, Zerna C, Coutts SB, Frayne R, Goodyear B, Haffenden A, Smith EE. Cerebral Amyloid Angiopathy Is Associated With Executive Dysfunction and Mild Cognitive Impairment. *Stroke* 2016; **47**: 2010-2016 [PMID: 27338926 DOI: 10.1161/STROKEAHA.116.012999]
- 6 **Xiong L**, Davidsdottir S, Reijmer YD, Shoamanesh A, Roongpiboonsopit D, Thanprasertsuk S, Martinez-Ramirez S, Charidimou A, Ayres AM, Fotiadis P, Gurol E, Blacker DL, Greenberg SM, Viswanathan A. Cognitive Profile and its Association with Neuroimaging Markers of Non-Demented Cerebral Amyloid Angiopathy Patients in a Stroke Unit. *J Alzheimers Dis* 2016; **52**: 171-178 [PMID: 27060947 DOI: 10.3233/JAD-150890]
- 7 **McDonald RJ**, Schwartz KM, Eckel LJ, Diehn FE, Hunt CH, Bartholmai BJ, Erickson BJ, Kallmes DF. The effects of changes in utilization and technological advancements of cross-sectional imaging on radiologist workload. *Acad Radiol* 2015; **22**: 1191-1198 [PMID: 26210525 DOI: 10.1016/j.acra.2015.05.007]
- 8 **Salvatore C**, Cerasa A, Castiglioni I. MRI Characterizes the Progressive Course of AD and Predicts Conversion to Alzheimer's Dementia 24 Months Before Probable Diagnosis. *Front Aging Neurosci* 2018; **10**: 135 [PMID: 29881340 DOI: 10.3389/fnagi.2018.00135]



Published by **Baishideng Publishing Group Inc**
7041 Koll Center Parkway, Suite 160, Pleasanton, CA 94566, USA

Telephone: +1-925-3991568

E-mail: bpgoffice@wjgnet.com

Help Desk: <https://www.f6publishing.com/helpdesk>

<https://www.wjgnet.com>

